Fall 2012

# Applications of mesoporous silica and zeolites for drug delivery

Ashish Datt
*University of Iowa*

# APPLICATIONS OF MESOPOROUS SILICA AND ZEOLITES FOR DRUG DELIVERY

by

Ashish Datt

An Abstract

Of a thesis submitted in partial fulfillment
of the requirements for the Doctor of
Philosophy degree in Chemistry
in the Graduate College of
The University of Iowa

December 2012

Thesis Supervisor: Professor Sarah C. Larsen

ABSTRACT

Zeolites and mesoporous silica were used as drug delivery systems for the loading and release of small drug molecules, aspirin and 5-fluorouracil. Different parameters were varied such as aluminum content in the zeolite, effect of distribution of functional groups and the method of surface modification in the case of mesoporous silica. The effect of the aforementioned variables was studied on drug loading and release from these microporous and mesoporous systems. The drug loaded materials were extensively characterized using various physicochemical techniques such as powder X-ray diffraction, nitrogen adsorption isotherms, infrared spectroscopy, solid state NMR and thermogravimetric analysis. Quantum calculations and molecular dynamics simulations were performed in order to validate the experimental data and also to obtain a molecular level insight of the drugs inside the pores of the host materials. Drug templated synthesis of mesoporous silica was also carried out in the presence of aspirin as the template. The aspirin templated material was characterized by aforementioned techniques and showed a sustained drug release profile.


Abstract Approved: _____
Thesis Supervisor

_____
Title and Department

_____
Date

# APPLICATIONS OF MESOPOROUS SILICA AND ZEOLITES FOR DRUG DELIVERY

by

Ashish Datt

A thesis submitted in partial fulfillment
of the requirements for the Doctor of
Philosophy degree in Chemistry
in the Graduate College of
The University of Iowa

December 2012

Thesis Supervisor: Professor Sarah C. Larsen

Graduate College
The University of Iowa
Iowa City, Iowa

CERTIFICATE OF APPROVAL

_____

PH.D. THESIS

_____

This is to certify that the Ph.D. thesis of

Ashish Datt

has been approved by the Examining Committee
for the thesis requirement for the Doctor of Philosophy
degree in Chemistry at the December 2012 graduation.

Thesis Committee: _____
Sarah C. Larsen, Thesis Supervisor

_____
Claudio J. Margulis

_____
Vicki H. Grassian

_____
Amanda J. Haes

_____
Lee E. Kirsch

To (MY FAMILY)

Life Lived for others is the Life Lived FOREVER

Ashish Datt

# ACKNOWLEDGMENTS

There are moments in life which can never be expressed in words, in writings, and not even in any form of expressions. I got this opportunity to live it large just because of my family, specially my brother. These are those people in front of whom you will always fall short to thank them on what they have done for you and contributed. I found another person of such respect and it was none other than Dr. Sarah C. Larsen. The definition of BOSS was redefined by Dr. Larsen to be the nicest, sweetest and most caring person one can ever find in life. She was my home away from home, always felt comfortable when she was around. So I take this opportunity to let you know how blessed I am, that I got a chance to get trained under your supervision. I would like to take this opportunity to express my deepest gratitude for being there for me during all of my good and bad times during my doctoral work.

I would like to thank Divya for being there through the good and bad times with me. This journey wouldn't have been smooth without her. In addition, I was fortunate enough to have a friend like Lokesh who guided me consistently both in research and in my personal life. I would like to thank his whole family for their support I would also like to thank Sai and his wife Spandana for everything they did for me. I would like to thank Sampada for hanging in there with me even though I was one hard mate in terms of my temper to stay with. Especially, the formatting of this thesis wouldn't have been so easy if you weren't there.

My stay in Iowa became so memorable because of friends like Adil, Harsha, Amninder, Sharavathi who always made sure things were going fine for me.

I had a chance to work with some very talented people in the lab and would like to thank all my present and past labmates Ram, Anton, Will, Karna, Melissa, Yulia, Paul, and Shani. And there was my mini research group, the pool of most smart undergraduates and high school students that I worked with. It was pleasure working and learning many things from them. I would also like to thank members of this chemistry department whom I interacted and shared the experiences. There are many many friends who have made my stay in Iowa very enjoyable and full of happiness. I don't know if this acknowledgement is any justice to their efforts on making me a better individual.

Finally, I would like to express my sincere gratitude to all members of my thesis committee. I would also like to thank all the faculty members and members of this chemistry department with whom I learnt/taught and shared experiences throughout this graduate program .

This will remain my most satisfying journey forever.

.

## ABSTRACT

Zeolites and mesoporous silica were used as drug delivery systems for the loading and release of small drug molecules, aspirin and 5-fluorouracil. Different parameters were varied such as aluminum content in the zeolite, effect of distribution of functional groups and the method of surface modification in case of mesoporous silica. The effect of the aforementioned variables was studied on drug loading and release from these microporous and mesoporous systems. The drug loaded materials were extensively characterized using various physical techniques such as powder X-ray diffraction, nitrogen isotherms, infrared spectroscopy, solid state NMR and thermogravimetric analysis. Quantum calculations and molecular dynamics simulations were performed in order to validate the experimental data and also to obtain a molecular level insight of the drugs inside the pores of the host materials. Drug templated synthesis of mesoporous silica was also carried out in the presence of aspirin as the template. The aspirin templated material was characterized by aforementioned techniques and showed a sustained drug release profile.

TABLE OF CONTENTS

LIST OF TABLES ..... iv

LIST OF FIGURES ..... v

CHAPTER 1 INTRODUCTION ..... 1

1.1 Zeolites – Properties and Applications ..... 1
1.2 Mesoporous Silica – Synthesis and Modifications ..... 4
1.3 Drug Delivery – Tuning the Loading and Release Properties ..... 9
1.4 Thesis overview ..... 10

CHAPTER 2 PHYSICOCHEMICAL CHARACTERIZATION ..... 14

2.1 Powder X-ray Diffraction ..... 14
2.2 Nitrogen adsorption isotherms ..... 17
2.3 Thermogravimetric Analysis ..... 22
2.4 Fourier Transform Infra-red Spectroscopy ..... 23
2.5 Solid State NMR ..... 24
2.6 UV-Vis Spectroscopy ..... 31
2.7 Electron Microscopy ..... 33

CHAPTER 3 THEORETICAL METHODS ..... 38

3.1 Geometry Optimization ..... 38
3.2 Hartree-Fock Method ..... 38
3.3 Density Functional Theory ..... 41
3.4 Molecular Dynamics Simulations ..... 43

CHAPTER 4 AN EXPERIMENTAL AND COMPUTATIONAL STUDY OF THE LOADING AND RELEASE OF ASPIRIN FROM ZEOLITE HY ..... 47

4.1 Abstract ..... 47
4.2 Introduction ..... 47
4.3 Experimental Section ..... 51
4.3.1 Sample Preparation ..... 51
4.3.2 Aspirin Loading and Release ..... 51
4.3.3 Theoretical Methods ..... 52
4.4 Characterization ..... 53
4.4 Results and Discussion ..... 54
4.4.1 Physicochemical Characterization of Parent and Aspirin-loaded Zeolite Y ..... 54

CHAPTER 5 ASPIRIN LOADING AND RELEASE FROM MCM-41 FUNCTIONALIZED WITH AMINOPROPYL GROUPS VIA CO-CONDENSATION OR POSTSYNTHESIS MODIFICATION METHODS ..... 77

5.1Abstract ..... 77

5.2 Introduction....78
5.3 Experimental Procedures....82
5.3.1 Materials....82
5.3.2 Synthesis of MCM-41....83
5.3.3 Co-condensation of APTES with MCM-41....83
5.3.4 Post-synthesis grafting of the APTES on MCM-41....83
5.3.5 Aspirin Loading and Release....84
5.4 Characterization....84
5.5 Theoretical Procedure....86
5.6 Results....88
5.6.1 Synthesis and Characterization of MCM-41 Functionalized with APTES by Co-Condensation and Post-Synthesis Grafting....88
5.6.2 NMR and FTIR Characterization of the MCM-41 and Aspirin Loaded MCM-41 Samples....93
5.6.3 Molecular Dynamics Simulation of Aspirin in MCM 41....97
5.6.4 Aspirin Release from MCM-41....100
5.7 Discussion....103
5.8 Conclusions....108

CHAPTER 6 LOADING AND RELEASE OF 5-FLUOROURACIL FROM HY ZEOLITES WITH VARYING $SIO_2/AL_2O_3$ RATIOS....109

6.1 Abstract....109
6.2 Introduction....109
6.3 Experimental Section....112
6.3.1 Sample Preparation....112
6.3.2 5-Fluorouracil Loading and Release....113
6.4 Characterization....114
6.5 Results and Discussion....115
6.5.1 Physicochemical Characterization of Zeolite HY Before and After 5-FU Loading....115
6.5.2 FTIR and NMR Results....120
6.5.3 5-Fluorouracil Release from HY Zeolites....124
6.5.4 Discussion....128
6.6 Conclusions....130

CHAPTER 7 LOADING AND RELEASE OF SMALL DRUG MOLECULES USING AMINE FUNCTIONALIZED MESOPOROUS SILICA SBA-15....131

7.1 Abstract....131
7.2 Introduction....131
7.3 Experimental Procedures....133
7.3.1 Materials Required and Synthesis....133
7.3.2 Drug Loading and Release....134
7.3.3 Characterization....135
7.4 Results and Discussion....136
7.4.1 Physiochemical Properties....136
7.4.2 Aspirin Loaded SBA-15....136
7.5 Conclusions....148

CHAPTER 8 ASPIRIN TEMPLATED MESOPOROUS SILICA SYNTHESIS....150

8.1 Abstract....150

8.2 Introduction.....150
8.3. Experimental Details .....152
8.3.1. Materials Required & Synthetic Procedure .....152
8.3.2. Characterization.....154
8.4 Results and Discussion .....155
8.5 Conclusions.....163

CHAPTER 9 CONCLUSIONS AND FUTURE WORK.....166

9.1 Conclusions.....166
9.2 Future Work.....169

REFERENCES .....171

LIST OF TABLES

Table

1. Physicochemical properties of the zeolites before and after aspirin loading.....59
2. Relative integrated intensities and linewidths (Hz) from the $^{27}$Al MAS NMR spectra.....67
3. Fitted kinetic release parameters for aspirin release from HY .....70
4. Calculated (HF) and experimental vibrational frequencies (FTIR) for aspirin and aspirin/zeolite Y .....74
5. Physicochemical properties of the MCM-41 before and after aspirin loading.....92
6. Fitted kinetic parameters for the release of aspirin from MCM-41 samples .....105
7. Physicochemical properties of parent and drug loaded zeolites .....119
8. Experimental FTIR frequencies for selected vibrational bands of 5-FU and zeolite HY/5-FU.....122
9. Fitted Kinetic Release Parameters for 5-fluorouracil Release from HY .....127
10. Physicochemical properties of SBA-15 materials before and after drug loading.....137
11. Kinetic parameters for the aspirin release from the parent and functionalized SBA-15 samples.....144

LIST OF FIGURES

Figure


1. FAU Framework type showing the (top) pore surface in yellow and (bottom) pore diameter in zeolite Y.....3
2. Different types of surface silanol groups in mesoporous silica. .....6
3. Schematic representation of the glancing angle and the path length difference. .....15
4. Powder X-ray diffraction pattern for zeolite HY. .....19
5. Typical nitrogen adsorption-desorption isotherm profiles for porous and non porous materials. .....20
6. BET Plot for zeolite HY. .....21
7. Representative thermograms for the pure aspirin (inset) and aspirin loaded zeolite HY. .....25
8. Potential energy changes when a spring is relaxed or compressed. .....26
9. Representative FTIR spectrum of fluorouracil loaded in zeolite HY. .....27
10. Energy level splitting diagram for a nucleus with I = 1/2.....30
11. Representative $^{27}Al$ MAS NMR spectrum of zeolite HY with $SiO_2/Al_2O_3$ = 30.....32
12. Possible electronic transitions in a hypothetical energy diagram .....34
13. Representative UV-Vis spectrum for 5-FU in phosphate buffer. .....36
14. SEM image (top) for SBA-15 and TEM image (bottom) of MCM-41 mesoporous silica. .....37
15. Characteristic potential energy surface showing the progress of the reaction.....39
16. T12 Cluster model used for the quantum calculations of zeolites. .....42
17. Snapshot of the orientation of aspirin inside the pores of mesoporous silica during a MD simulation. .....45
18. Zeolite Y (top) and aspirin (bottom) structures .....49
19. Powder X-ray diffraction patterns of a) parent zeolite Y (HY-5) and b) zeolite Y (HY-5) with aspirin .....56
20. Thermogravimetric Analysis of aspirin loaded zeolite (HY-5); the inset shows the thermogram of the pure aspirin. .....57

21. Nitrogen adsorption-desorption isotherm measurements for a) zeolite Y (HY-5) and b) aspirin loaded zeolite HY-5. (representative adsorption isotherms shown in green and black and representative desorption isotherms shown in blue and red). .....58

22. (left figure) FTIR spectra of a) aspirin, b) HY-5 with aspirin, c) HY-30 with aspirin and d) HY-60 with aspirin. The spectra in b-d are the difference spectra of the zeolite with aspirin with the spectrum of the zeolite alone substracted, (right figure) Difference FT-IR spectra of the hydroxyl group region for a) HY-5 with aspirin, c) HY-30 with aspirin and d) HY-60 with aspirin. The spectra in a-c are difference spectra of the zeolite with aspirin with the spectrum of the parent zeolite subtracted.....64

23. $^{27}$Al MAS NMR spectra for HY-5, HY-30, HY-60 before (a, c, e) and after loading with aspirin (b, d, f), respectively. .....65

24. Representative $^{13}$C CP-MAS NMR spectrum of (a) physical mixture of zeolite Y (HY-5) with aspirin, (b) drug loaded zeolite Y (HY-5) with aspirin.....66

25. Aspirin release kinetics from a) HY-5, b) HY-30 and c) HY-60. The least squares fits to the function Q=Qmax[1-exp(-k1*t)] are shown by the solid lines. The release was measured at in phosphate buffer solution at pH=7.4. .....69

26. T12 cluster of zeolite Y geometry optimized a) without and b-c) with an aspirin molecule and d) with an aspirin anion. Two different views of the same cluster with aspirin are provided in b) and c). .....73

27. Schematic representations for mesoporous silica (left) and aspirin (right) .....79

28. Different methods of functionalization (A) Co-condensation method, and (B) Postsynthesis grafting method.....81

29. Powder X-ray diffraction patterns of both parent and functionalized mesoporous silica MCM-41 samples before and after drug loading. .....90

30. Nitrogen adsorption-desorption isotherms for (a) parent MCM-41 material and (b) MCM-41 with aspirin. .....91

31. TGA plots of MCM-PS-1 loaded with aspirin and pure aspirin as an inset. .....94

32. Solid State $^{13}$C NMR of (a) physical mixture of mesoporous silica and aspirin (CP-MAS), (b) MCM-41 with aspirin (CP-MAS), (c) MCM-41 with aspirin (SP with decoupling), (d) MCM-CC-1 with aspirin (CP-MAS), and (e) MCM-PS-1 with aspirin (CP-MAS).....96

33. FTIR spectra of (a) MCM-41 and (b) MCM-PS-1 with (red) and without (black) aspirin loaded. The FTIR spectra before and after loading have been scaled to the strong framework Si−O vibration from ∼1000−1200 cm−1 for display purposes.....98

34. Results of the molecular dynamics simulation showing (a) the starting configuration with aspirin in the center of the 3 nm mesopore and (b) after 400 ps with the phenyl ring of aspirin orientated parallel to the pore wall. .....99

35. Aspirin release kinetics from MCM-CC-1 (filled square), MCM-CC-2 (open square), MCM-PS-1 (open circle), MCM-PS-2 (filled circle),and MCM-41 (filled triangle) are shown. ....101

36. Summary of drug release ....106

37. 5-FU ....111

38. Powder X-ray diffraction patterns of a) parent zeolite Y (HY-30) and b) zeolite Y (HY-30) with 5-fluorouracil. ....116

39. TGA of pure 5-fluorouracil (left) and zeolite HY-30 with 5-fluorouracil (right). ....117

40. Nitrogen adsorption-desorption isotherms for (a) HY-30 and (b) HY-30 with 5-FU. ● represents the desorption branch and ■ represents the adsorption branch of the nitrogen isotherms. ....118

41. FTIR spectra of a) 5-FU, b) HY-5/5-FU, c) HY-30/5-FU and d) HY60/5-FU. ....121

42. $^{27}$Al MAS spectra of parent and 5-FU loaded HY zeolites ....125

43. 5-FU release kinetics from HY-5, HY-30 and HY-60. The least squares fits to the function Q=Qmax[1-exp(-k1*t)] are shown by the solid lines for HY-30 and HY-60. The release was measured in phosphate buffer solution at pH=7.4. ....126

44. The loading and release of 5-FU from HY as a function of silica to alumina ratio. ....129

45. Nitrogen isotherm plots for (a) parent SBA-15, and (b) SBA-15 with aspirin ....138

46. Thermograms of (inset) pure aspirin and SBA-15-PS1 with aspirin ....140

47. $^{13}$C CP-MAS Solid State NMR spectra for (a) physical mixture of SBA-15 and aspirin, (b) SBA-15 with aspirin, and (c) SBA-15-PS2 with aspirin ....141

48. FT-IR spectra showing the vibrations from SBA-15 materials with aspirin ....143

49. Drug release profiles for different SBA-15 type materials (a) SBA-15 with aspirin, (b) SBA-15-PS1 with aspirin, and (c) SBA-15-PS2 with aspirin ....146

50. Higuchi model fit for the drug release profiles from SBA-15 mesoporous silica ....147

51. Schematic Representation of Aspirin templated amorphous silica ....153

52. Powder X-ray diffraction pattern of aspirin templated silica material ....156

53. Nitrogen Adsorption-Desorption Isotherm for the aspirin template silica particles. ....158

54. Thermogram of aspirin template silica particles showing the characteristic weight changes due to the aspirin molecule. .....159

55. $^{13}C$ CP-MAS Solid State NMR for (a) aspirin (b) aspirin template mesoporous silica.....161

56. FT-IR spectra of the parent aspirin (bottom) and the aspirin templated silica material (top).....162

57. Drug Release profile from the aspirin template system.....164

58. Comparison of loading of different drug molecules in the host zeolite HY .....167

# CHAPTER 1

# INTRODUCTION

## 1.1 Zeolites – Properties and Applications

Boiling stones, also known as zeolites, derived from the Greek words ‘zeo’ (boil) and ‘lithos’ (stone) were first discovered by a Swedish mineralogist A.F. Cronstedt in 1756. Since then, about 50 natural and more than 200 synthetic zeolites have been identified as a separate group of minerals. Natural zeolites cannot meet the huge demands in industry particularly in catalysis; therefore synthetic zeolites are produced in large quantities.[1]

Zeolites are microporous inorganic crystalline materials containing Si, Al and O atoms in their framework.[2] Their general formula can be represented as:

$$M_{x/n}[(AlO_2)_x(SiO_2)_y]\bullet wH_2O$$

where n is the valence of the cation M, w is the number of water molecules per unit cell, x and y are the total number of tetrahedral atoms per unit cell. The y/x ratio (Si/Al ratio) usually ranges from 1 to 5 or 10 to 100 for high silica zeolites. The cations are mobile and ordinarily undergo ion exchange. The water may be removed reversibly, generally by application of heat. Zeolites with low Si/Al ratios are widely used in adsorption and separation purposes. Such zeolites are nearly "saturated" in aluminium in the framework composition with a molar ratio of Si/Al ≈ 1, which is considered as the highest aluminum content possible in tetrahedral alumosilicate frameworks. As a consequence, they contain the maximum number of cation exchange sites balancing the framework aluminum, and thus the highest cation contents and exchange capacities. Zeolites having Si/Al ratios

from 10 to 100 or higher, possess a surface which is more homogeneous with an organophilic-hydrophobic selectivity.[3] These zeolites adsorb the less polar organic molecules more strongly and only weakly interact with water and other polar molecules. In addition to this novel surface selectivity, the high silica zeolite compositions still contain a small concentration of aluminum in the framework and the accompanying stoichiometric cation exchange sites. Thus, their cation exchange properties allow the introduction of acidic groups via the well-known zeolite ion exchange reactions, essential to the development of acid hydrocarbon catalysis properties.

Zeolite Y has an Faujasite (FAU)-type structure as shown in Figure 1. The basic structural units for zeolite Y are the sodalite cages, which are arranged in a three dimensional network which in turn form supercages. Supercages are 12 membered rings which are formed by the connection of sodalite cages in the framework. The diameter of the supercages and the size of the 12-ring opening of Y zeolites are ~12 Å and ~7.4 Å, respectively.[4-6]

Zeolites have well defined pore structures and topologies, having a large surface area with tunable surface properties. Owing to these properties, they are widely used in the separation of small molecules from large molecules. This makes the phenomenon of shape selectivity possible in catalytic reactions. The presence of aluminum in the zeolite framework gives a net negative charge to the system and thus creates the existence of charge compensating counter ions. Such counter-ions provide the zeolite with a very unique property of ion-exchange. The ion-exchange properties of the zeolites are widely used in transition metal catalysis as well as in water softening techniques. Zeolites also

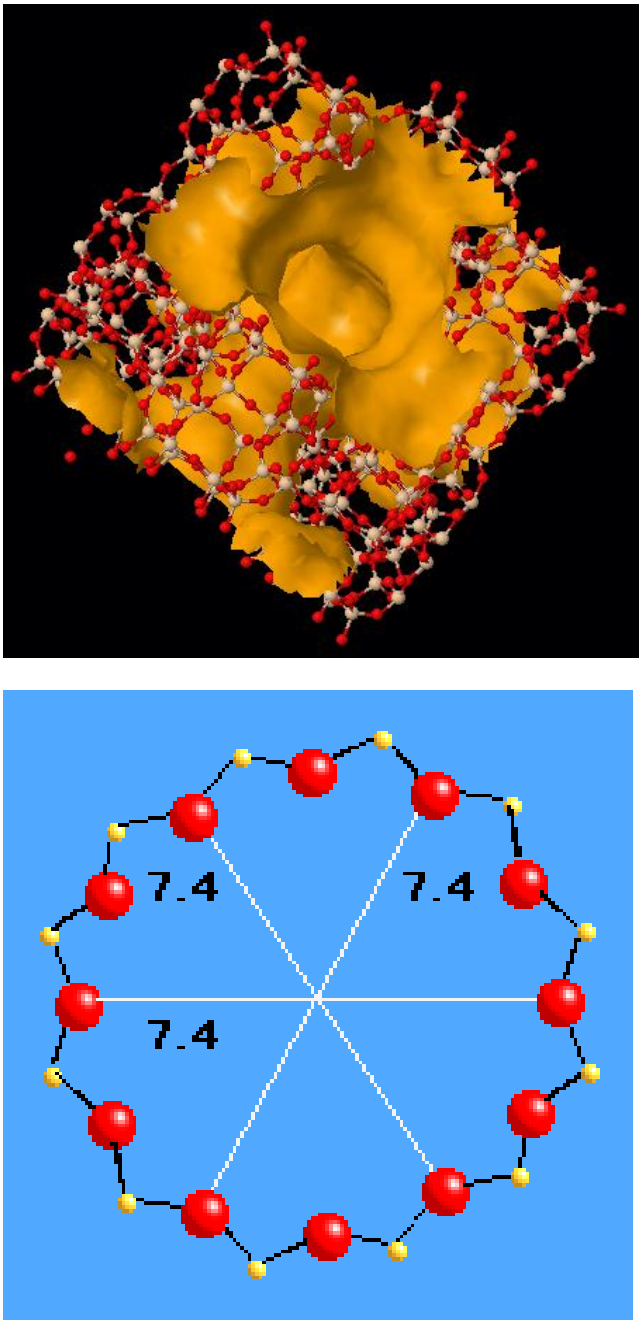


Figure 1. FAU Framework type showing the (top) pore surface in yellow and (bottom) pore diameter in zeolite Y

---

Source: http://www.iza-structure.org.

possess high surface area and high thermal stability which makes them potential candidates for a wide range of applications such as adsorbents, detergents and catalysts.[7-9]

There are several examples of biomedical applications of zeolites reported in the literature including imaging,[10-13] wound treatment, and drug delivery.[14-17] These examples demonstrate that different zeolites can be exchanged with cations, functionalized or loaded with drug molecules for specific biomedical applications. In examples of drug-loading, zeolite Y/magnetite nanocomposites have been loaded with doxorubicin molecules and paraquat molecules have been loaded into trimethylsilyl functionalized zeolite Y. Recently, the adsorption of sulfonamide antibiotics on zeolite Y has been investigated.[14,15] Controlled release in zeolites has been achieved through modifying the external surface of the zeolites with functional groups. The release is controlled by a number of factors such as the pore size, the nature of the grafted functional groups, and the nature of intermolecular interactions. The loading and release of anthelminthics and other drugs from zeolites have produced a controlled release of these molecules. For example, dealuminated zeolite Y has been successfully used in the controlled delivery of ibuprofen.[18] Additional research is needed to understand fundamental zeolite and drug molecule interactions so that the loading and release of the drug molecules can be better controlled.[14-17]

## 1.2 Mesoporous Silica – Synthesis and Modifications

Mesoporous silicas are amorphous inorganic materials which have silicon and oxygen atoms in their framework. ‘Meso’porous indicates that the pore sizes in such materials range from 2-50 nm in dimension. Mesoporous silica materials can be synthesized in the presence of surfactants, which act as templates for the

polycondensation of the silicon source (sodium silicate, tetraethyl orthosilicate).[19,20] Since 1992, when Mobil Corporation synthesized the MCM-41 material, there have been various types of mesoporous silica in the literature which have been investigated for diverse applications. The basic difference between different mesoporous silica originates from the nature of the synthesis conditions in which they are synthesized.[21,22] The factors which determine the physiochemical parameters of mesoporous silica (type of mesostructure, pore diameter, pore volume, wall thickness) are dependent on the synthesis conditions such as pH of the medium, type of the silicon source, templating agent and its concentration.[23-25]

The nature of synthesis conditions will vary the surface characteristics of the mesoporous silica (silica-surfactant interactions). The nature of the surface terminated silanol groups will vary accordingly in different mesoporous silica. The different types of silanol groups (shown in Figure 2) which are present on the surface of mesoporous silica are: (a) single, (b) hydrogen bonded, and (c) geminal silanol groups.[26] The content of the silanol groups depends on how the silica-surfactant interactions are broken or on how surfactants are removed, once silica formation is complete. Due to the presence of these silanol groups at the surface of mesoporous silica, these materials are of particular interest because of tailorable surface modifications.[27,28]

The literature precedent shows that there are a number of ways in which one can tune the surface according to the applications required. There are three major ways in which we can modify the surface of mesoporous silica: (a) post synthesis grafting, (b) co-condensation, and (c) the generation of periodic mesoporous silica.[29] In post synthesis grafting, the functionalization/modification of the surface takes place after the synthesis

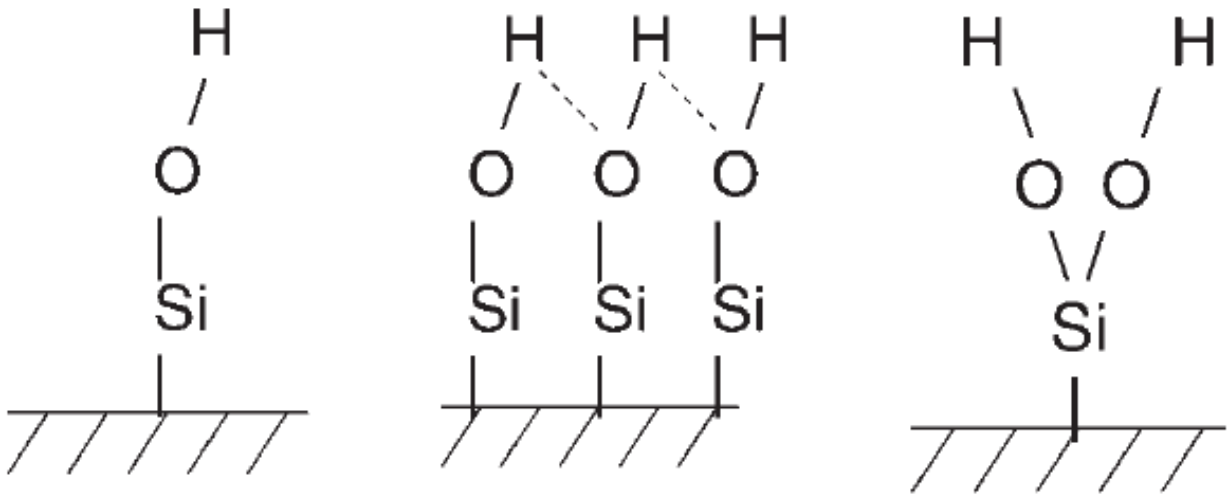


Figure 2. Different types of surface silanol groups in mesoporous silica.

---

Source: Reference 26

reaction. The only disadvantage of this method is that if the functional group reacts preferentially at the pore openings then the diffusion of the functionalization agent for further functionalization is blocked, thus leads to an inhomogeneous distribution of the functional groups. Co-condensation method involves the addition of the functionalization agent during the synthesis of the mesoporous silica framework. The problem of pore blocking is not observed in this type of functionalization as the functional group is being incorporated while the framework is being formed. As a result of which, a more homogeneous distribution of functional groups is obtained. Co-condensation method of surface modification has some disadvantages too including: (a) loss of the mesostructure with the incorporation of organic groups, and (b) homocondensation of the organosilane species makes the point of homogeneous distribution less predictive. Periodic mesoporous silica can be synthesized by the hydrolysis and condensation of the bridged organosilane precursors of the type $(R`O)_3Si\text{-}R\text{-}Si(OR`)_3$. The organic precursors are incorporated in the three dimensional network of the mesoporous silica as opposed to the aforementioned surface functionalization methods. The disadvantage associated with such systems is that they have disordered pore structures with very large pore diameters.[30-32]

Mesoporous silica materials possess high surface areas, tunable pore diameters, high pore volumes and well organized porosity which make them potential candidates for many applications. The chemical nature and the ability to tailor the surface for chemical modification as discussed above makes them ideal for applications such as adsorption, catalysis, separation, sensors and drug delivery systems.[33-37] Mesoporous silica have been used extensively in chromatographic columns for the separation of molecules and the,

immobilization of biomolecules such as enzymes.[38,39] Incorporation of aluminum species in mesoporous silica gives them an interesting character to catalyze reactions. The catalytic properties arise from the formation of Brönsted and Lewis acid sites by the incorporation of aluminum in the framework.[40-47] Recently, mesoporous silica has also been used as hard templates in the fabrication of mesocellular foams. Mesoporous silica has also found their way in environmental and biomedical applications.[48-53] Core-shell nanocomposites of magnetite-mesoporous silica are extensively used in environmental applications for the adsorption of toxic ions.[54,55] Due to their high surface areas and pore volumes, mesoporous silicas have attracted great attention in the biomedical applications. They have been extensively researched as promising drug delivery systems. The literature precedent shows many examples of drug molecules loaded onto mesoporous silica materials. Ibuprofen has been extensively studied as a model drug adsorbed on the mesoporous silica materials, MCM-41, SBA-15 and hexagonal mesoporous silica (HMS) materials.[18,56-58] In addition, many anti-cancer drugs, such as doxorubicin and camptothecin, have also been studied for controlled release using mesoporous silica materials. Lin and co-workers studied the release of a drug cargo using capped mesoporous silica materials. Recently, rattle type mesoporous silica $Fe_3O_4$@$SiO_2$ have also attracted a great deal of attention for drug delivery.[59,60] Drug delivery using mesoporous silica materials largely depends on the textural properties of these materials, such as pore diameters, pore volumes, particle morphology and surface modifications.

## 1.3 Drug Delivery – Tuning the Loading and Release Properties

The transport of drug molecules to the target organ without the loss of its pharmaceutical and therapeutic activity is the basic principle which exists as the basis for most drug delivery systems. Previous studies have shown the efficacy of polymer systems in delivering the drugs in a controlled release manner. Polymeric systems are proven to be beneficial in terms of improving the efficiency of drug transport and also reducing the toxic side effects of the drug. Drug delivery systems are basically classified based on their release mechanism and the method of their preparation. The different types of drug delivery systems include; (a) physical systems such as porous monoliths and biodegradable systems, (b) chemical systems which involve the immobilization of the drug molecules, and (c) biological systems which include gene therapy.[61-64]

The nature of the release of the drug process will depend on the type of the system used for the controlled release process. However, there are some primary ways by which the drug cargo can be released in the system: diffusion, degradation and swelling followed by diffusion. Drug delivery systems can also be tuned according to the nature of the drug under consideration such as slow release of water soluble drug or fast release of water insoluble drug. The ideal drug delivery system should be biodegradable, biocompatible, mechanically strong and capable of achieving high drug dosage form.

There are several mathematical and mechanistic models available in the literature to describe the drug release profile.[56] The nature of the release profile will depend on the type of the system. For our studies, diffusion controlled mechanisms are of particular interest. The solubility of the drug and its dissolution in the solvent media both influence

the drug release kinetics. The diffusion process in the case of porous systems can be best described by Fickian diffusion models. The extent of release from a porous matrix can be described by Fick's second law of diffusion which relates the change of concentration with time. Furthermore, in a one dimensional system the drug release process is directly proportional to the square root of the time. A first order release kinetics is generally obtained from a porous matrix.[65-67]

Mesoporous silica and zeolites are both the potential candidates for controlled drug delivery systems. The loading of the drug in these systems can be maximized by understanding the nature of host-guest chemistry. Several important factors such as polarity, nature of surface functional groups, surface area and pore diameter influence the loading of drug molecules in these porous systems. The literature precedent shows the controlled release of drug molecules such as doxorubicin, camptothecin, aspirin and, ibuprofen from these systems was achieved either by surface modification or by changing the polarity of the system. By changing the physicochemical properties of the host materials we can change the nature of interactions of the guest (drug) molecules and as a result of which we have better control over the loading and release properties of drug molecules in these materials.[68-71]

## 1.4 Thesis overview

The research work described in this thesis investigates the interaction between the small drug molecules and the zeolites and mesoporous silica materials. Chapter 1 deals with the basic introduction of these materials and, the basic properties of zeolites which make them attractive candidates for this research. The chapter also discusses the properties of mesoporous silica and their modification procedures which can be

performed in order to tune their properties for drug delivery applications. Finally, concepts of drug delivery and how these materials can be used as drug delivery systems are discussed. Chapter 2 focuses on the various physicochemical techniques that were used to characterize the host and host-guest materials along with a brief background on various techniques. Chapter 3 centers on the computational methods that were used to complement the experimental observations, with some background on the theory involved in those methods.

The interaction between the aspirin molecule with zeolite HY framework is investigated in chapter 4. The goal of this research was to load and release aspirin drug from the zeolite HY and to understand the nature of interactions of the drug molecule in the zeolitic framework. The molecular level understanding came from the application of various spectroscopic techniques, such as FTIR and solid state NMR. Nitrogen adsorption isotherms were conducted in order to determine the surface area and pore volume of the materials before and after the drug loading. The aspirin loaded materials were released in the phosphate buffer maintained at pH 7.4. The study revealed that the aluminum content in the zeolite is a critical factor for the release of aspirin molecules from the zeolites with varying $SiO_2/Al_2O_3$ ratios.

Loading and release of aspirin molecules from functionalized mesoporous silica is discussed in Chapter 5. Mesoporous silica, MCM-41, was synthesized and functionalized with amine groups by two different methods including post synthesis grafting and co-condensation methods. Both parent and functionalized materials were loaded with aspirin molecules and their release at physiological pH was studied. The mesoporous materials were characterized for the amine content and the aspirin loading using thermogravimetric

analysis. The molecular level understanding of the aspirin molecule in the pores of mesoporous silica came using spectroscopic methods such as $^{13}C$ solid state NMR. The missing carbonyl peak in case of parent MCM-41 with aspirin molecule was investigated using single pulse NMR experiments. The extent of release of the aspirin molecules from the parent and functionalized systems were studied and the effect of the distribution of the amine groups towards drug loading and release was investigated.

Chapter 6 deals with the interaction of an anti-cancer drug (5-fluorouracil) with zeolite HY with varying $SiO_2/Al_2O_3$ ratios. The effect of aluminum content on the loading and release of the drug was studied. $^{27}Al$ solid state NMR studies showed that aluminum is playing an important role in the loading of the drug in the zeolitic systems. The decrease in the tetrahedral aluminum peak intensity after drug loading makes it conclusive towards the effect of aluminum in drug loading and drug release.

Loading and release of small drug molecules using amine functionalized mesoporous silica SBA-15 is discussed in chapter 7. Both parent and amine functionalized mesoporous materials were studied for the loading and release of small drug molecules such as aspirin and 5-fluorouracil. Nitrogen isotherms and thermogravimetric analysis were used to study the loading of the drugs in the mesoporous host systems. The interaction between the phenyl group of aspirin with the mesoporous pore wall has been hypothesized based on the shifts in the phenyl group resonances in the $^{13}C$ CP-MAS NMR. It was observed that with an increase in the amine loading, the release of aspirin is decreased.

Chapter 8 focuses on the synthesis of drug loaded mesoporous silica without the use of templates. The encapsulation of aspirin molecules in a one-step co-condensation

procedure for the synthesis of mesoporous silica has been proposed. The formation of the silica framework has been characterized using a wide variety of physicochemical techniques such as thermogravimetric analysis, solid state NMR, and nitrogen isotherms. The drug release studies were also performed and a sustained release of the drug from the drug templated system was obtained.

Chapter 9 summarizes the research work described in this thesis and makes some proposals for the future work on novel strategies for using zeolites and mesoporous silica for biomedical applications.

# CHAPTER 2

# PHYSICOCHEMICAL CHARACTERIZATION

## 2.1 Powder X-ray Diffraction

With the discovery of X-rays in 1895 by William Rontgen, it was soon confirmed that they can be diffracted if passed through a crystal. X-rays are very high energy electromagnetic radiations having wavelengths of the order of $10^{-10}$ m. X-rays are generated by bombarding a metal with high energy electrons, as a result, the electrons decelerate and generate a continuous range of wavelengths, known as Bremsstrahlung radiations. With a cascade of collisions, each collision expels an electron from an inner shell and an electron of higher energy drops into the vacancy, thus emitting the excess energy as the X-ray photon.

In order to understand the theory behind the X-ray diffraction experiment, let's assume that the lattice planes in a crystal are a mirror. Consider the reflection of two parallel rays of the same wavelength by two adjacent planes of the crystal lattice. The reflected rays from the crystal lattice planes will differ in the path length by a distance. The angle which the incident beam makes with the crystal lattice plane, away from the normal is known as the glancing angle. In order to observe a constructive interference, the path length difference should be an integer of the wavelengths. Thus, a reflection would be observed if the glancing angle satisfies the Bragg's law:

$$n\lambda = 2dsin\theta \qquad (1)$$

where n is the order of reflection and θ is the glancing angle. Figure 3 shows the schematic representation of the glancing angle and then path length difference.[72,73]

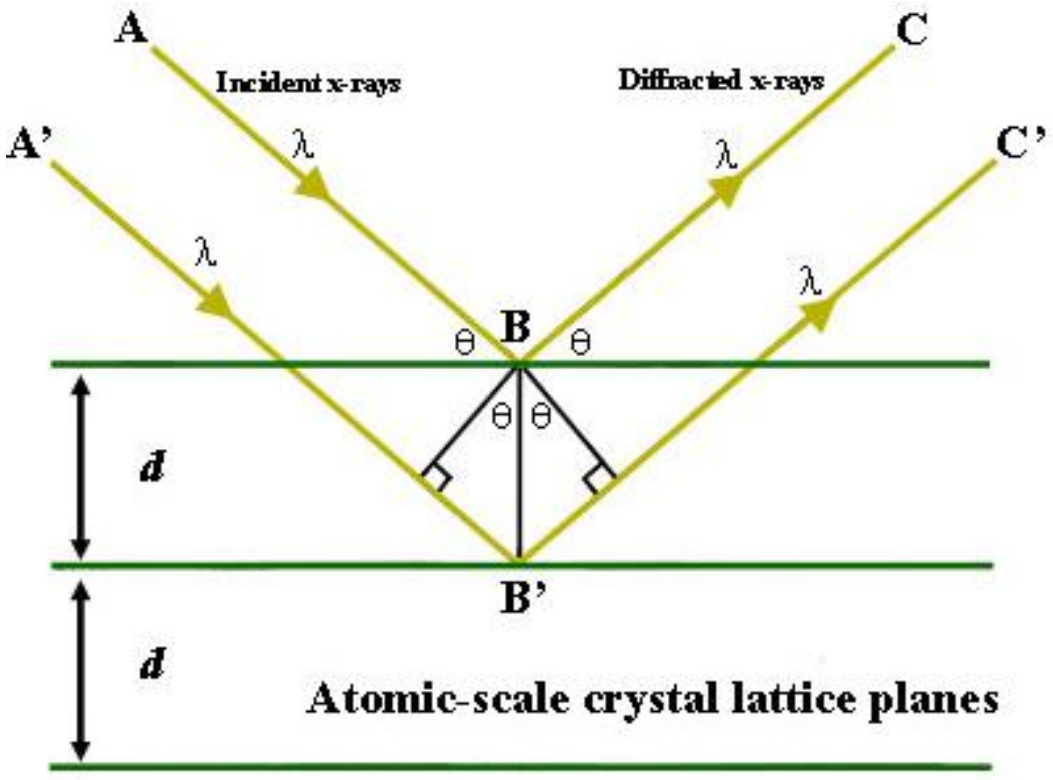


Figure 3. Schematic representation of the glancing angle and the path length difference.

---

Source: http://serc.carleton.edu/research_education/geochemsheets/BraggsLaw.html

X-ray diffraction is a widely used technique in research, for analyzing single crystals as well as powder crystallites. The technique to analyze the powder pattern is commonly known as powder X-ray diffraction. Powder X-ray diffraction can be used to determine the crystallinity as well as the ordering between the planes for amorphous substances. In the case of mesoporous silica, which is amorphous in nature, powder patterns can show the ordering of the mesopores in the framework. Other important information which can be deduced from the powder patterns in case of mesoporous silica is obtained by comparing the intensity of the most intense peak between the parent and the organically functionalized mesoporous silica. Generally, a decrease in the diffraction intensity occurs when organic functionalization takes place inside the mesopores. Additional useful information, which can be obtained from the powder diffraction patterns of mesoporous silica is the pore diameter. There is an empirical relation which relates the interplanar spacing to the pore width of mesoporous silica. The relation is given as:

$$W_d = cd\left(\frac{\rho V_p}{1+\rho V_p}\right)^{1/2} \qquad (2)$$

where, $W_d$ is the pore diameter of the mesoporous silica, c is the constant which depends on the pore geometry and is usually equal to 1.155 for hexagonally ordered pores, $V_p$ is the pore volume and ρ is the pore wall density (2.2 g $cm^{-3}$ for siliceous materials).

In case of zeolites, powder diffraction patterns can reveal information regarding the crystallinity of the sample. The position and the relative intensities of the powder pattern acts as a fingerprint for a particular type of the zeolite. Each zeolite has a characteristic powder diffraction pattern. Figure 4 shows the typical powder diffraction pattern for zeolite HY.

## 2.2 Nitrogen adsorption isotherms

The term adsorption was first introduced by Kayser in 1881 to denote the condensation of gases on free surfaces. In other words, physical adsorption is the enrichment (adsorption) or depletion (desorption) of the interfacial layer. The substance on which the gas molecules are adsorbed is known as adsorbent and the substance which gets adsorbed is known as adsorbate. There are two major ways in which adsorption can take place; physical and chemical.

In the literature, there are many models which describe the adsorption phenomenon using mathematical relationships. The most widely used adsorption model is the one given by the Brunauer-Emmett-Teller (BET) method for the determination of the surface area of porous solids. The BET equation used can be given as:

$$\frac{1}{W\left(\left(\frac{P_0}{P}\right)-1\right)} = \frac{1}{W_m C} + \frac{C-1}{W_m C}\left(\frac{P}{P_0}\right) \qquad (3)$$

where, W is the weight of the gas adsorbed at a relative pressure $P/P_0$ and $W_m$ is the weight of the adsorbate required for the monolayer surface coverage. C is the BET constant and is related to the energy of adsorption in the first adsorbed layer and it indicates the magnitude of the adsorbent/adsorbate interactions. Surface area measurements are usually done using inert adsorbates such as $N_2$, or Ar. Based on the amount of the adsorbate required to form a monolayer surface coverage, one can calculate the total surface area of the material. The cross sectional area ($A_{cs}$) value for the hexagonal close-packed nitrogen monolayer at 77 K is 16.2 $Å^2$. Thus, the total surface area of the sample can be expressed as:

$$S_t = \frac{W_m N A_{cs}}{M} \qquad (4)$$

where, N is the Avogadro's number (6.022 X $10^{23}$ molecules $mol^{-1}$) and M is the molecular weight of the adsorbate.

In addition to the surface area measurements, there are other models in the literature which can be used to calculate the pore volume and pore size distributions. For pore volume measurements, the total pore volume can be calculated from the amount of vapor which is adsorbed at relative pressure close to unity (with an assumption that all the pores are filled by the adsorbate). The volume of nitrogen adsorbed ($V_{ads}$) can be converted to the volume of liquid nitrogen ($V_{liq}$) contained in the pores using the following equation:

$$V_{liq} = \frac{P_a V_{ads} V_m}{RT} \qquad (5)$$

where $P_a$ and T are ambient pressure and temperature respectively and $V_m$ is the molar volume of the liquid adsorbate (34.7 $cm^3$ $mol^{-1}$ for nitrogen). Figure 5 shows the Type I isotherm which is typical of microporous solids and chemisorption isotherms. Type II is shown by finely divided non-porous solids. Type III and V are typical of vapor adsorption (i.e. water vapor on hydrophobic materials). Type IV and V feature a hysteresis loop generated by the capillary condensation of the adsorbate in the mesopores of the solid. Finally, the rare type VI step-like isotherm is shown by nitrogen adsorbed on carbon.

The distribution of pore volumes with respect to the pore size is known as pore size distribution. The most common method for obtaining the pore size distribution is the Barrett-Joyner-Halenda (BJH) method. The basic assumptions which the BJH takes into consideration are; (a) cylindrical pore shape, (b) condensation take place at lower pressure in smaller pores and larger pores are filled as the relative pressure increases.

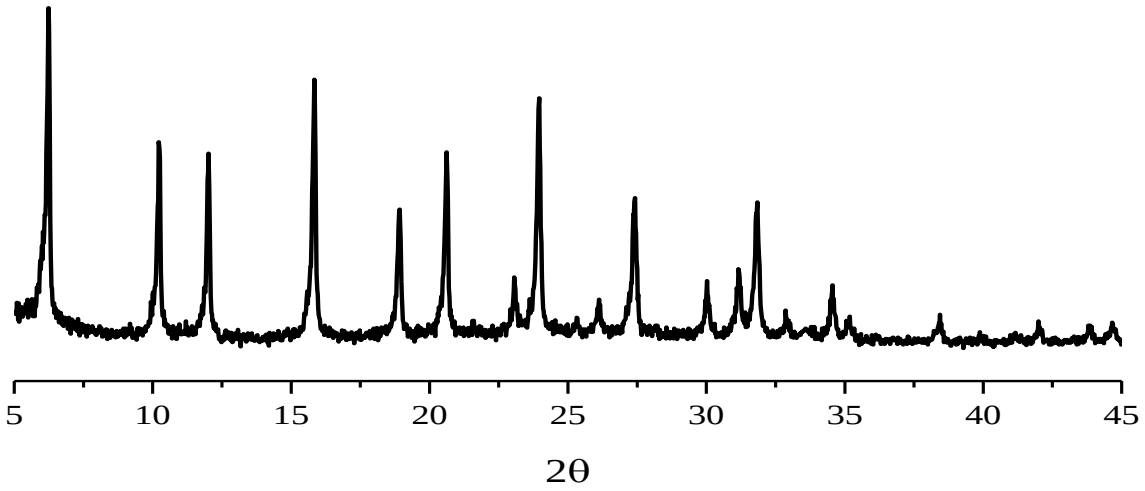


Figure 4. Powder X-ray diffraction pattern for zeolite HY.

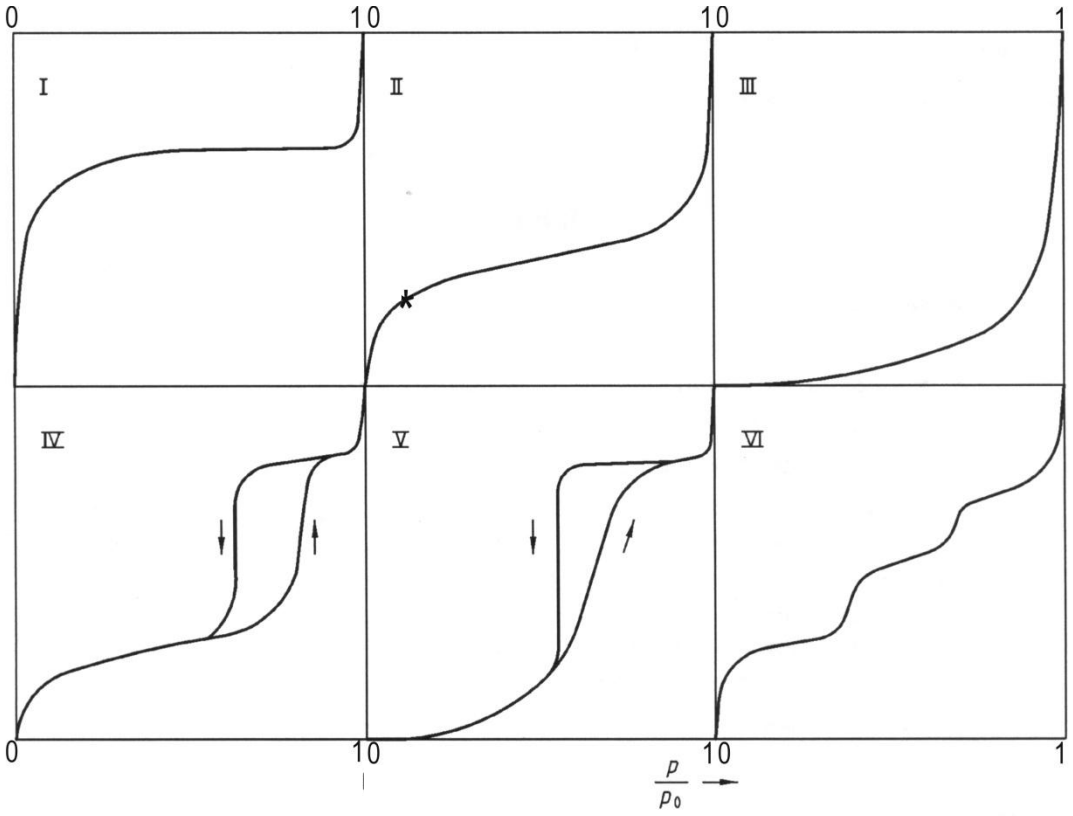


Figure 5. Typical nitrogen adsorption-desorption isotherm profiles for porous and non porous materials.

---

Source: https://www.helmholtz-berlin.de/forschung/enma/solare-brennstoffe/analytische-methoden/gassorptionsmessungen_en.html

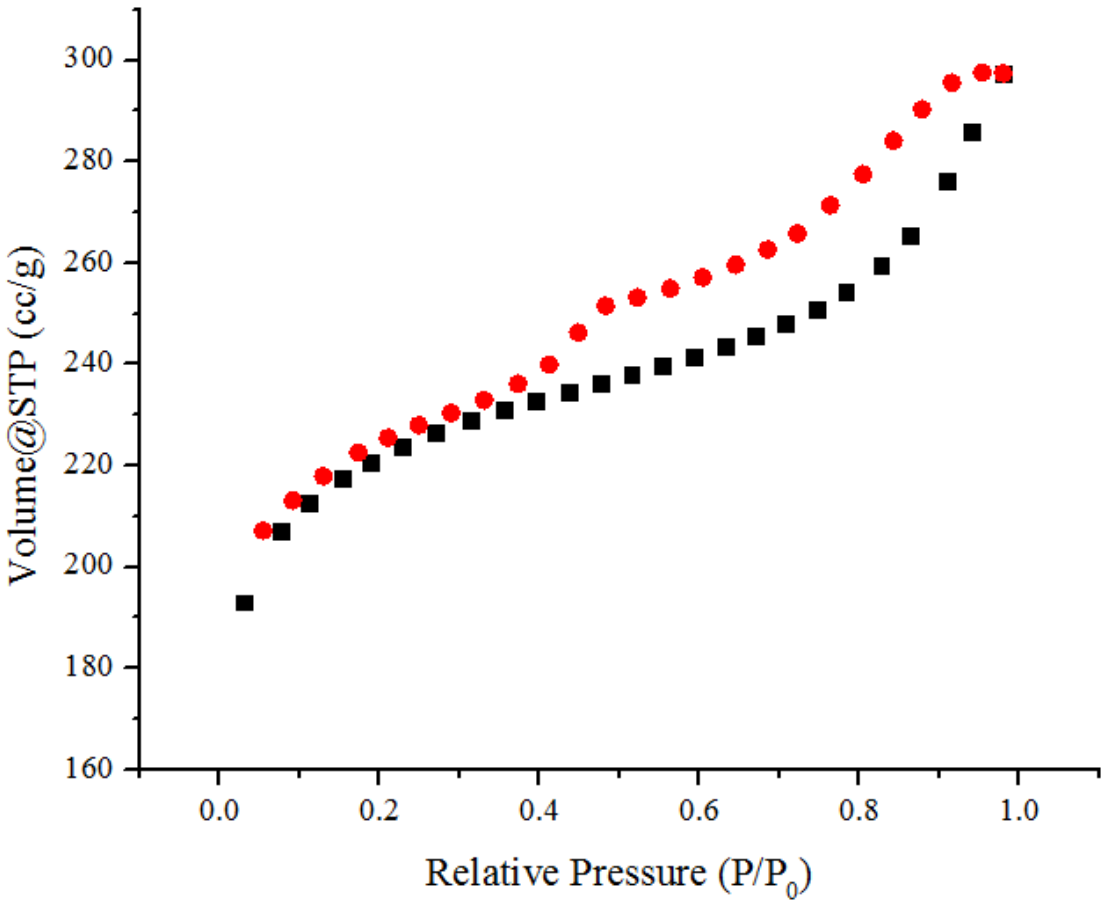


Figure 6. BET Plot for zeolite HY.

Mesoporous size calculations assuming the cylindrical geometry can be obtained by using the Kelvin equation:

$$r_k = \frac{-2\gamma V_m}{RTln\frac{P}{P_0}} \quad (6)$$

where, $\gamma$ is the surface tension of nitrogen at its boiling point (8.85 ergs $cm^{-2}$ at 77 K), $V_m$ is the molar volume of nitrogen, $r_k$ is the kelvin radius of the pore.[74,75]

Figure 6 shows a characteristic BET adsorption-desorption plot for HY zeolite. For zeolites, the hysteresis curve exhibits the typical Type I isotherm whereas for mesoporous silica it exhibits the Type IV isotherm.

## 2.3 Thermogravimetric Analysis

The method in which the effect of heat on the mass of a sample with time is studied to obtain quantitative information is known as the thermogravimetric method of analysis (TGA). There are various parameters which can be obtained from a particular thermal method of analysis namely mass, enthalpy, magnetic properties, and electrical properties. Thermal events are usually recorded by observing the change in the thermal property as the temperature is varied to give a thermal analysis curve or a thermogram. The thermal events which can lead to some important quantitative information can be melting, phase transition, decomposition, and glass transition.

Thermogravimetry, in particular, is the study of the change in mass of the sample as the temperature is varied. When the sample is heated from ambient to 1000 °C, under an atmosphere of $O_2$ or $N_2$, characteristic weight losses can be obtained which may yield important information regarding the physical processes occurring in the sample. The magnitude of the weight change can be used to provide the weight change due to that

particular transition. When there are more than one process taking place, the thermograms appear to be quite complex, and thus derivative thermograms provide a visual insight to the characteristic weight changes in the sample.[76,77]

Figure 7 shows the representative thermograms for the pure aspirin and aspirin loaded zeolite HY. The shape of thermogram of aspirin is clearly different when loaded onto zeolite HY, which shows the presence of aspirin in confined environments versus the free aspirin. The characteristic weight changes occurring due to the aspirin in its free state, are being observed at higher temperatures when confined in the micropores of zeolites.

## 2.4 Fourier Transform Infra-red Spectroscopy

This spectroscopic technique deals with the absorption of electromagnetic radiation in the infra-red region of the electromagnetic spectrum, which probes the changes in the vibrational energy levels of the molecule. This method is widely used in the identification and structural analysis of the organic compounds. The basic concepts behind this spectroscopic method can be easily understood by taking the analogy of the chemical bond to a spring or a harmonic oscillator. Figure 8 shows the changes in the potential energy when the spring is compressed and relaxed. The only difference between the chemical bond and the spring is that, in case of chemical bonds, the bond between the atoms eventually breaks if they are stretched too much. The resulting vibrational motion is called an anharmonic oscillation. The potential energy of the system can be expressed in terms of vibrational quantum number as:

$$E = \left(V + \frac{1}{2}\right)\nu \qquad (7)$$

where V is the vibrational quantum number and ν is the oscillating frequency. For polyatomic molecules, the complexity of the spectrum increases rapidly with increasing the number of atoms N in the molecule. With two major factors in effect, mass effect and the force constant effect, determine the position of vibrational stretching frequencies for particular functional groups. Other factors which influence the position of the vibrational stretching frequencies are hydrogen bonding, the neighboring functional groups and coupled vibrations.[78]

Figure 9 shows the infra-red spectrum of fluorouracil loaded in zeolite HY. For pure fluorouracil the peak at 1660 $cm^{-1}$ corresponds to the C=C stretching vibrations and those vibrations and blue shifted to 1685 $cm^{-1}$ in the drug loaded spectrum. This shows the effect of hydrogen bonding and neighboring group effects affecting the position of vibrational bands in the spectra, helping us understand the molecular level information from the samples.

## 2.5 Solid State NMR

Nuclear magnetic resonance (NMR) spectroscopy deals with the absorption of electromagnetic radiation in the radio frequency region, which results in changes in the orientation of the spinning nuclei in a magnetic field. This technique helps in the structural identification of the organic compounds. In order to understand the theory behind NMR, consider a nucleus spinning about its own axis carrying a charge will result in a magnetic field. In addition to this, the nucleus also possess an inherent property known as angular momentum. The angular momentum of spinning nuclei can be given as:

$$\boldsymbol{I}_Z = [I(I+1)]^{1/2}\frac{h}{2\pi} \qquad (8)$$

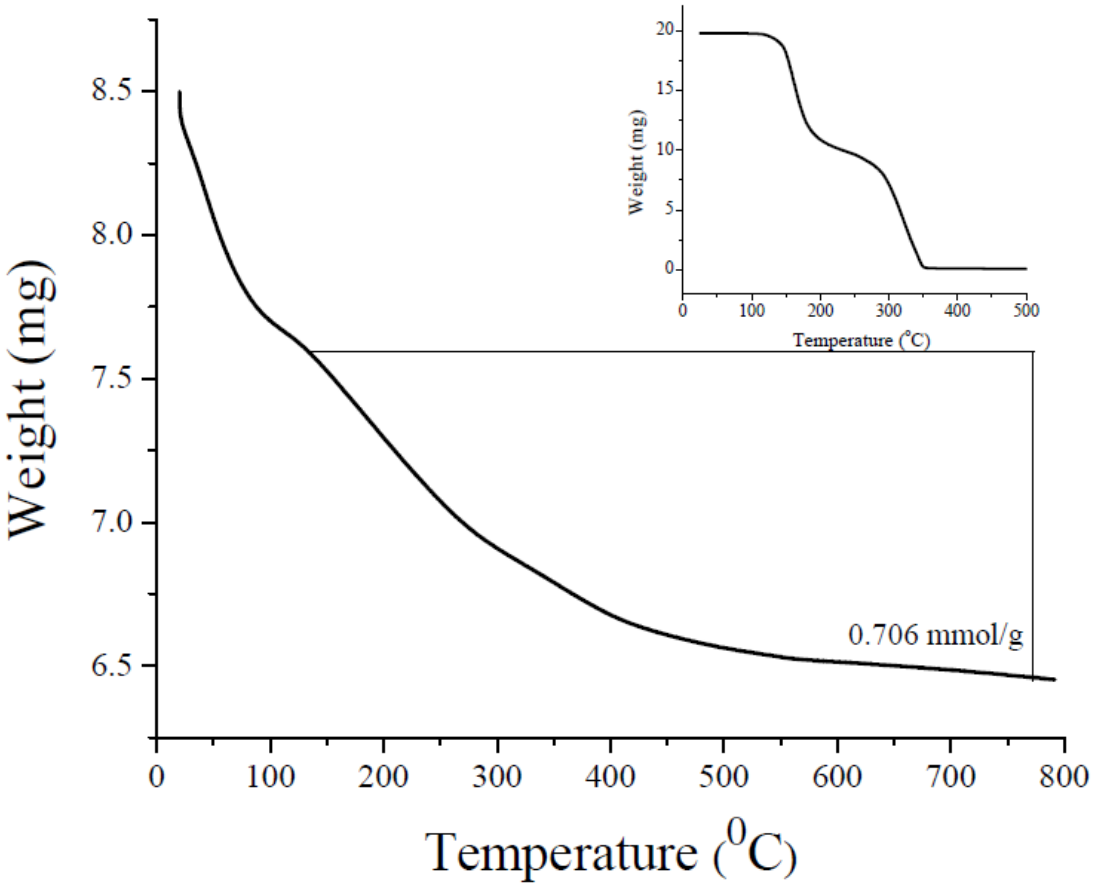


Figure 7. Representative thermograms for the pure aspirin (inset) and aspirin loaded zeolite HY.

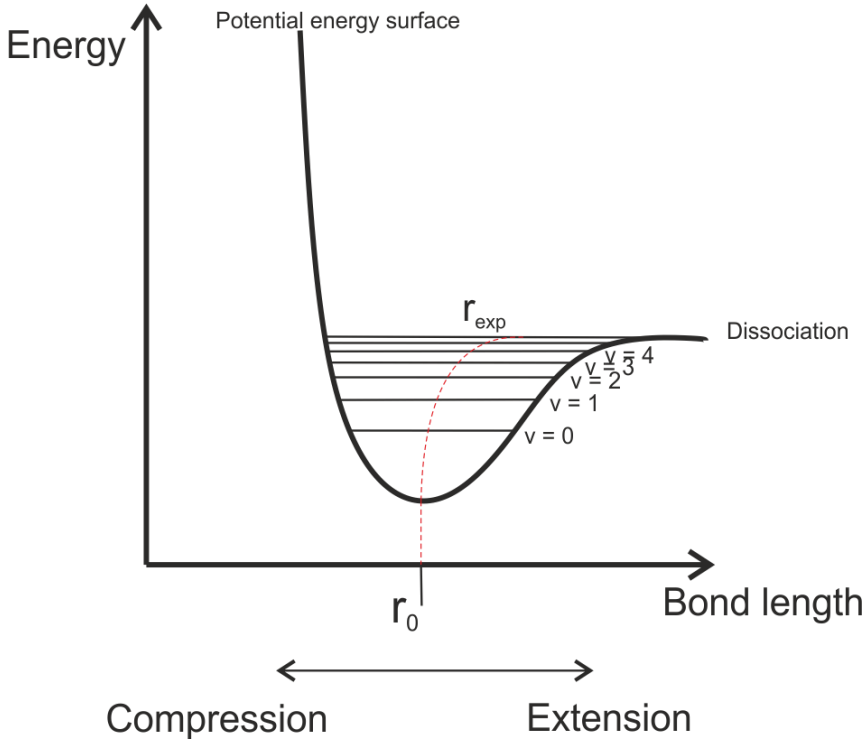


Figure 8. Potential energy changes when a spring is relaxed or compressed.

---

Source: http://www.chemtube3d.com/spectrovibcd1-ce-final.html

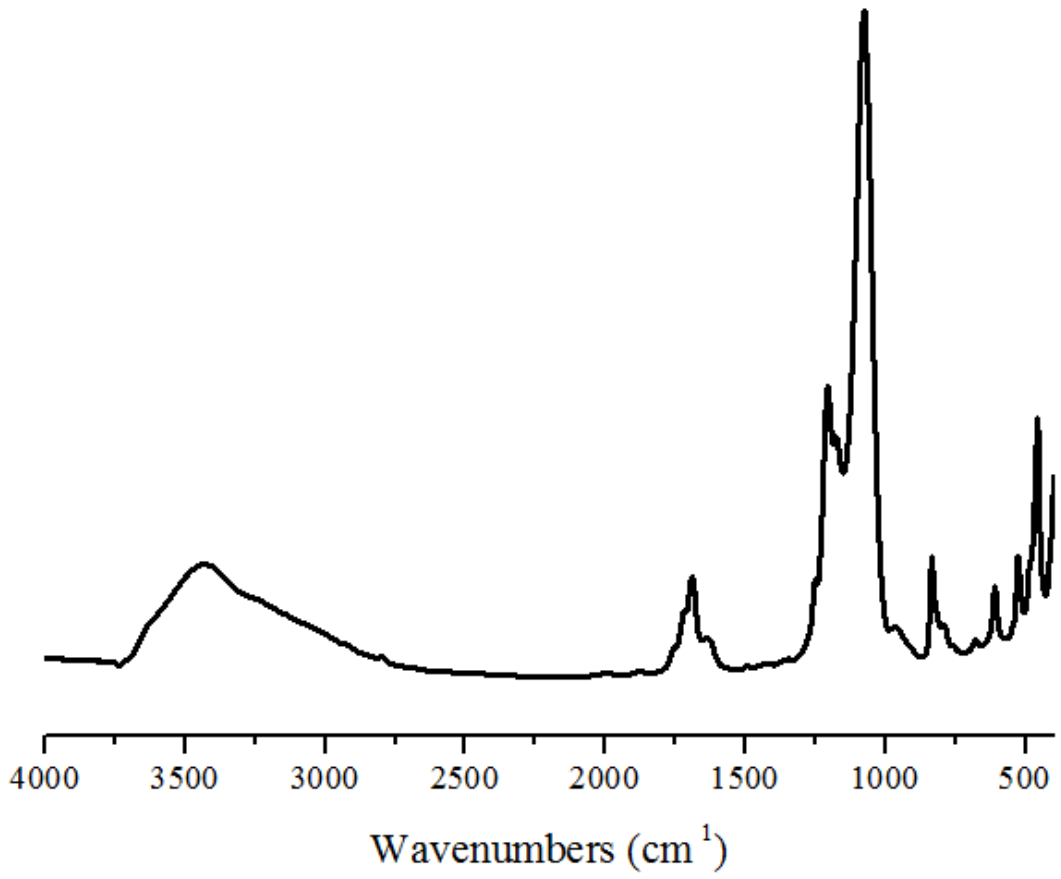


Figure 9. Representative FTIR spectrum of  fluorouracil loaded in zeolite HY.

where, h is the Planck's constant and h/2π is defined as the angular momentum unit. When magnetic field is applied, the angular momentum vector can only assume those orientations which are half integral or integral number of angular momentum units, such as:

$$\boldsymbol{I_z} = m_I \frac{h}{2\pi} \quad (9)$$

where, $\mathbf{I}_z$ represents the magnitude of the angular momentum in the direction of the field or the z-axis and $m_I$ is the magnetic quantum number. For a given nucleus, the ratio of the magnetic moment to the angular momentum is constant and is known as gyromagnetic ratio (γ).

$$\mu_z = \boldsymbol{I}_z \gamma \quad (10)$$

where $\mu_z$ is the magnetic moment and $\mathbf{I}_z$ is the angular momentum of the spinning nucleus (Figure 10). The energy of the interaction between the nucleus and the magnetic field (B) it experiences can be given as:

$$E_z = -\mu_z B = -m_I \gamma \frac{h}{2\pi} \quad (11)$$

From the above expression, it can be seen that the resonance frequency depends on the strength of the applied magnetic field, which can differ from one instrument to another. Due to varying degrees of shielding caused by neighboring electrons, nuclei in different chemical environments absorb at different magnitudes of the applied magnetic field. Such differences between the absorptions are known as chemical shifts (δ).

$$\delta = \left[\left(\frac{\nu - \nu_0}{\nu_0}\right)\right] . 10^6 \quad (12)$$

There are two major ways in which the NMR can be carried out, solution NMR and solid state NMR. The basic difference between the two is the way the averaging of

the motion of the molecules is carried out. In solution NMR, as the name suggests, the solvent medium is used to homogenize the solute environment and average out all the chemical anisotropies. In case of solid state NMR, this process of removing chemical shift anisotropy is accomplished by using the concept of magic angle spinning. The degree of chemical shift anisotropy varies with the angle between the principal axis of the molecule and the direction of the magnetic field according to the term $(1 - 3\text{Cos}^2\theta)$. Spinning the sample at the magic angle which is $(\theta = 54.74^0)$ makes the term $(1 - 3\text{Cos}^2\theta)$ go to zero and as a consequence the chemical anisotropy vanishes from the spectrum. The spinning speed should be higher than the frequency width of the spectrum, otherwise it may result in the appearance of spinning side bands.[79,80]

Solid state NMR has been widely used in elucidating the structure of both mesoporous silica and zeolites. The technique has been used extensively to understand the coordination environments of aluminum in $^{27}$Al NMR spectra. Figure 11 shows the representative spectrum of zeolite HY with $SiO_2/Al_2O_3 = 30$. There are two different peaks in the spectrum, the peak ~ 0 ppm can be assigned due to the octahedral coordination and the peak ~ 60 ppm originates due to the tetrahedral coordination. The tetrahedral peak corresponds to the framework aluminum whereas the octahedral aluminum corresponds to the extra-framework aluminum.

Solid state NMR can also be used to understand the motional freedom of the molecules in confined environments such as mesoporous silica and zeolites. Aspirin molecules adsorbed in mesoporous silica can be seen in the $^{13}$C CP-MAS spectrum but the –C=O carbon atoms present in aspirin are not observed. This is attributed to the high mobility of aspirin molecules in mesoporus silica that CP is not effective in observing

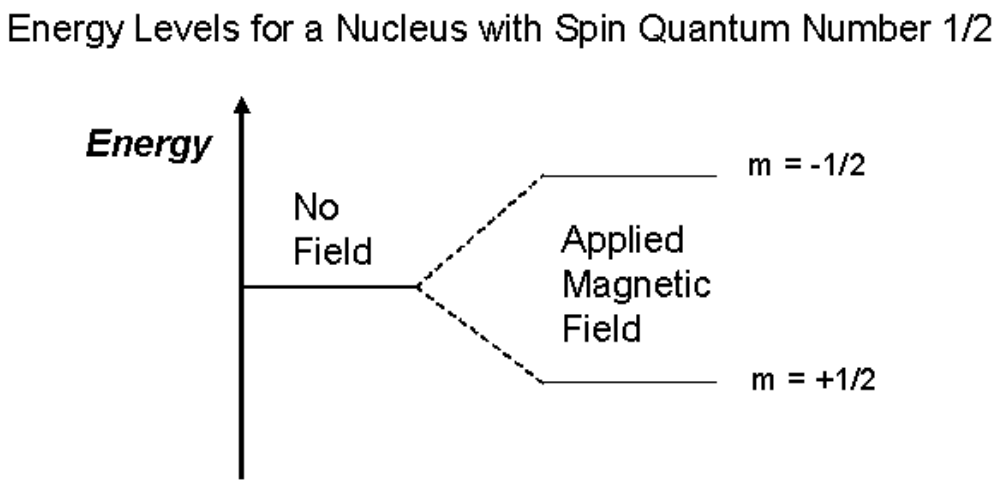


Figure 10. Energy level splitting diagram for a nucleus with I = 1/2.

---

Source: http://www.process-nmr.com/nmr1.htm

those peaks. The single pulse MAS experiment actually shows the –C=O peaks from aspirin. Thus solid state NMR effectively explains the motional freedom of molecules in mesopores.

## 2.6 UV-Vis Spectroscopy

The basic principle behind this spectroscopic method is the absorption of electromagnetic radiation in the visible and ultraviolet regions of the electromagnetic spectrum which results in the change in the electronic structure of molecules or ions. The energy gap required for these electronic transitions is very large ~ $10^5$ J $mol^{-1}$ which in turn corresponds to 200-800 nm in the wavelength units. Since the energy required for these transitions is high, vibrational and rotational transitions also occur. According to the Frank-Condon principle, the nature of electronic transition is very fast and rapid in comparison to vibrational or rotational transitions.

The electronic spectra consist of vibrational and rotational transitions but such transitions are not observed for molecules in solution because of physical interactions between the solute and the solvent molecules, resulting in the collisional broadening of vibrational and rotational fine structure. As a consequence, the band structure collapses and coalesces to form overlapping bands having their absorption maxima at $\lambda_{max}$.

Using the fundamentals of molecular orbital theory for organic compounds, the bonding and non-bonding orbitals are filled and the anti-bonding orbitals are empty. Figure 12 shows the various transitions which are possible. Unsaturated groups, chromophores, are responsible for n to $\pi^*$, and $\pi$ to $\pi^*$ transitions which occur in the near UV and visible region. Such transitions are used for quantitative analysis of the spectrum. Saturated groups, auxochromes, are heteroatoms which influence the absorption spectrum

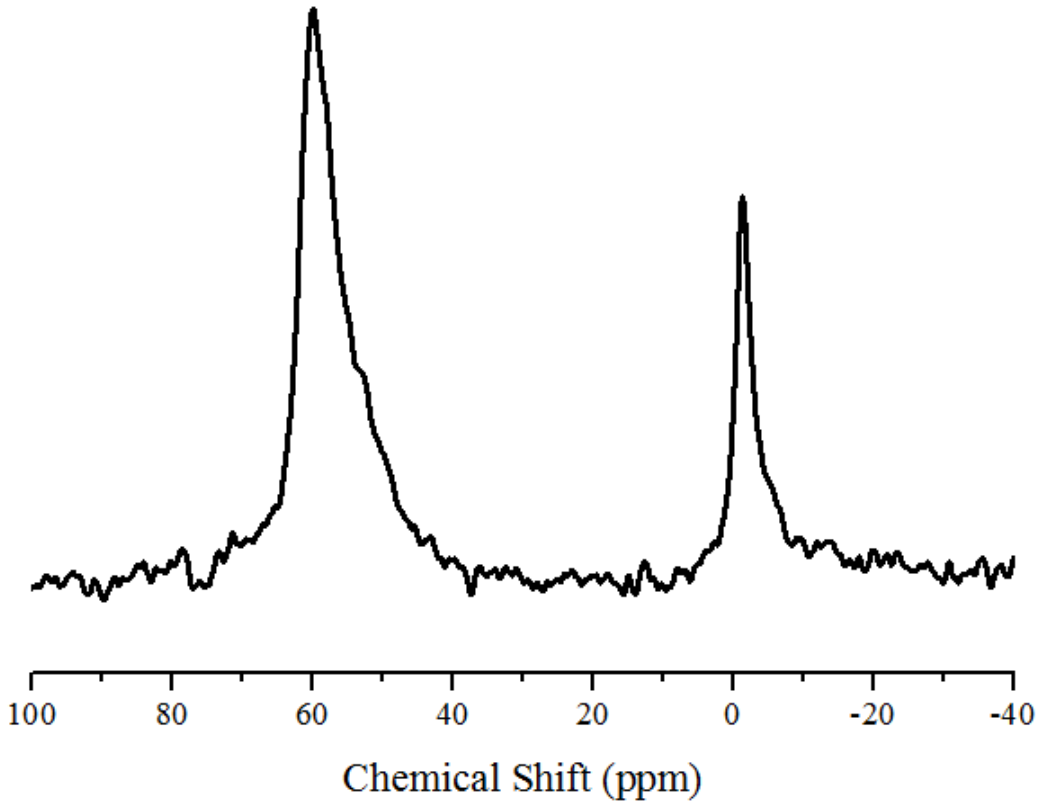


Figure 11. Representative $^{27}Al$ MAS NMR spectrum of zeolite HY with $SiO_2/Al_2O_3 = 30$

and cause shift in the absorption wavelengths.[78]

Figure 13 shows the characteristic UV-Vis spectrum for 5-FU dissolved in phosphate buffer. The spectrum shows the characteristic absorption maximum ~ 266 nm which arises due to the –C=O groups present in the system. Other peaks may appear in the spectrum which can be attributed to the conjugation of the phenyl system.

## 2.7 Electron Microscopy

Electron microscope is a type of microscope which uses a beam of electrons to create an image of the specimen. They are capable of much higher magnifications and have a greater resolving power than light microscopes. Electron microscopes are useful for studying the parameters such as particle size, morphology, pore structure, and the presence of different phases.

Transmission electron microscopy involves the use of high voltage electron beam which is emitted by the cathode and formed with the help of magnetic lenses. The electron beam which is transmitted from the specimen carries the information about the structure of the specimen. The spatial variation in the image is magnified with a series of magnetic lenses before it hits the detector. The images produced by this type of electron microscopy are two dimensional in nature. Figure 14 shows the representative TEM image of mesoporous silica particles MCM-41 and pore can be seen in the image with a bright and dark contrast. Bright regions marking the pores with the dark regions making the pore walls of mesoporous silica.

Scanning electron microscopy produces images by using and detecting the secondary electrons, emitted from the surface due to the excitation by the primary electron beam. In this technique, the electron beam is scanned across the surface of the

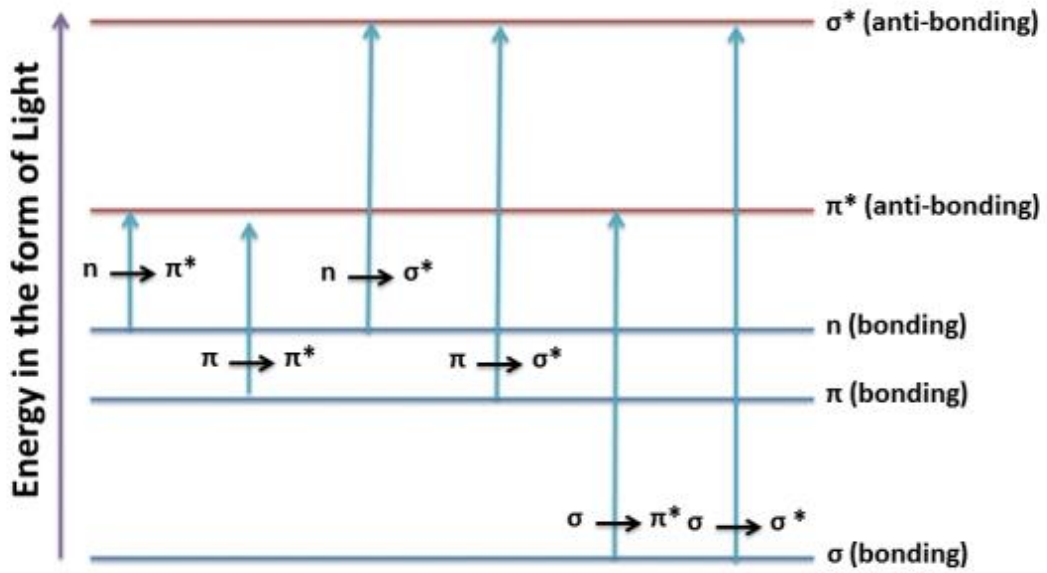


Figure 12. Possible electronic transitions in a hypothetical energy diagram

---

Source: http://pharmaxchange.info/press/2011/12/ultraviolet-visible-uv-vis-spectroscopy-principle/

sample in a raster pattern, which is then detected by the detector. This type of microscopy provides three dimensional images of the samples in consideration thus giving information regarding the topology and morphology of the sample.[81] Figure 14 shows the typical SEM image of mesoporous silica SBA-15.

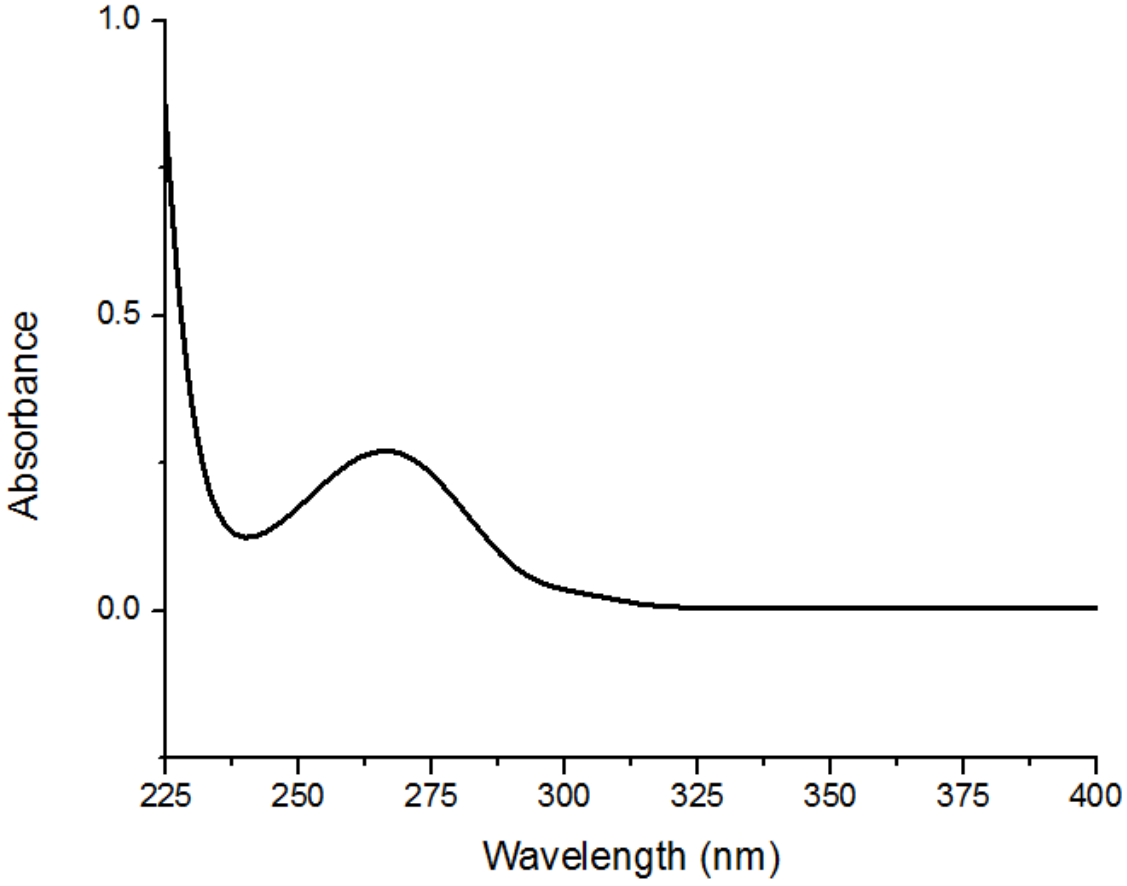


Figure 13. Representative UV-Vis spectrum for 5-FU in phosphate buffer.

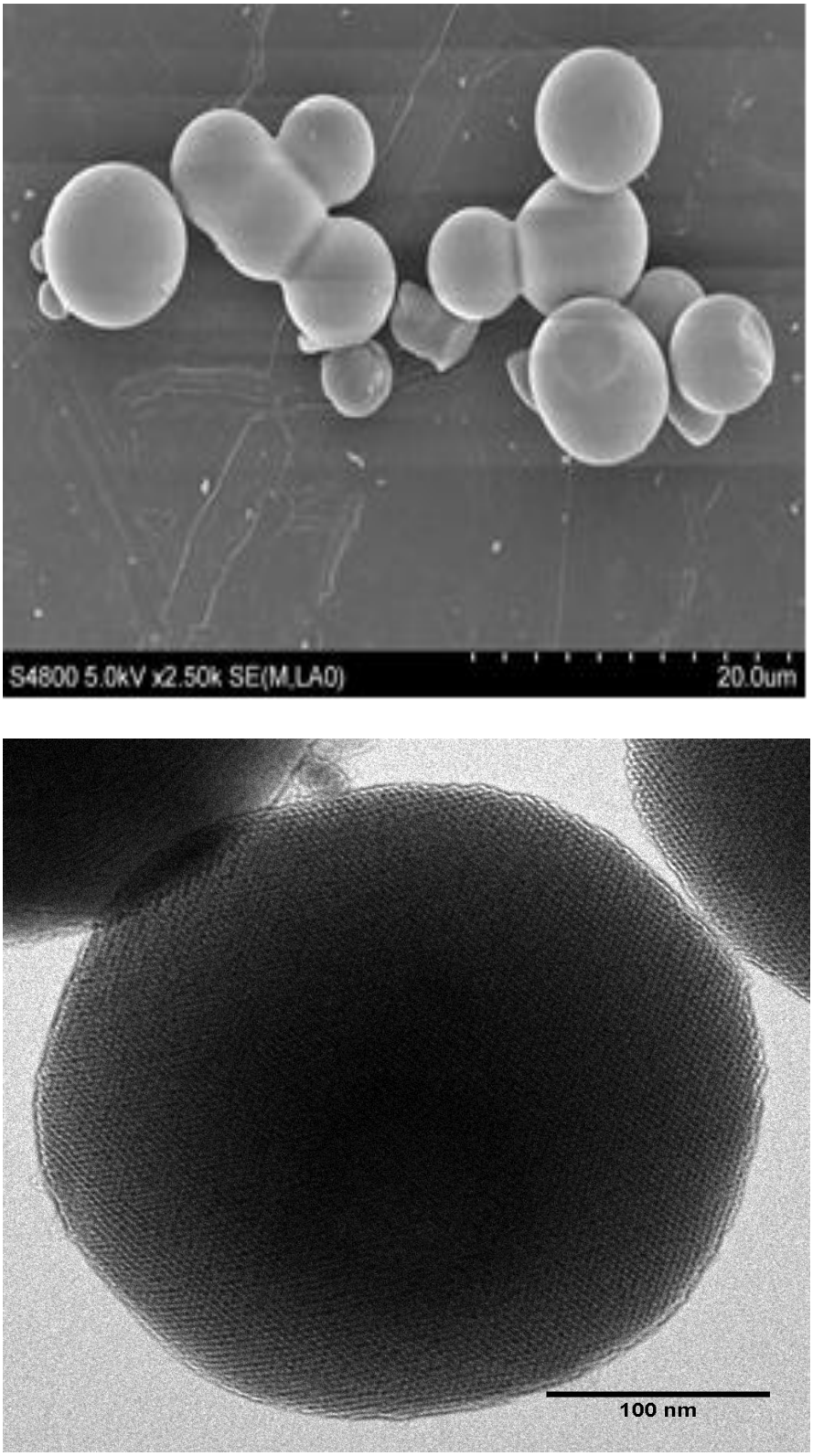


Figure 14. SEM image (top) for SBA-15 and TEM image (bottom) of MCM-41 mesoporous silica.

# CHAPTER 3

# THEORETICAL METHODS

## 3.1 Geometry Optimization

The graph between the potential energy and the bond length of a molecule is known as the potential energy surface (PES). Potential energy surfaces are important because they help us in understanding the relationship between the molecular geometry and the potential energy of the molecular system. Another interesting and important point on the potential energy surface, is the location of the stationary points. Stationary points are the points on the PES at which the surface is flat, i.e. parallel to the horizontal line corresponding to one geometric parameter. A molecule placed at the stationary point will remain there as far as the energy considerations goes but a molecule kept at any other point will try to fall into the region of lowest potential energy. The characterization or the location of the stationary point on the PES and its calculation for the geometry and energy from the PES is known as geometry optimization. The stationary point of interest can be a local minimum, a transition state or the ground state geometry.[82]

## 3.2 Hartree-Fock Method

The term “ab initio” is derived from the Latin term which means “from the beginning”. Ab initio computations are derived directly from theoretical principles. The most common type of ab initio calculation is the Hartree-Fock (HF) calculation, which relies on the central field approximation. According to the central field approximation, the coulombic electron-electron repulsion term is taken into consideration by integrating

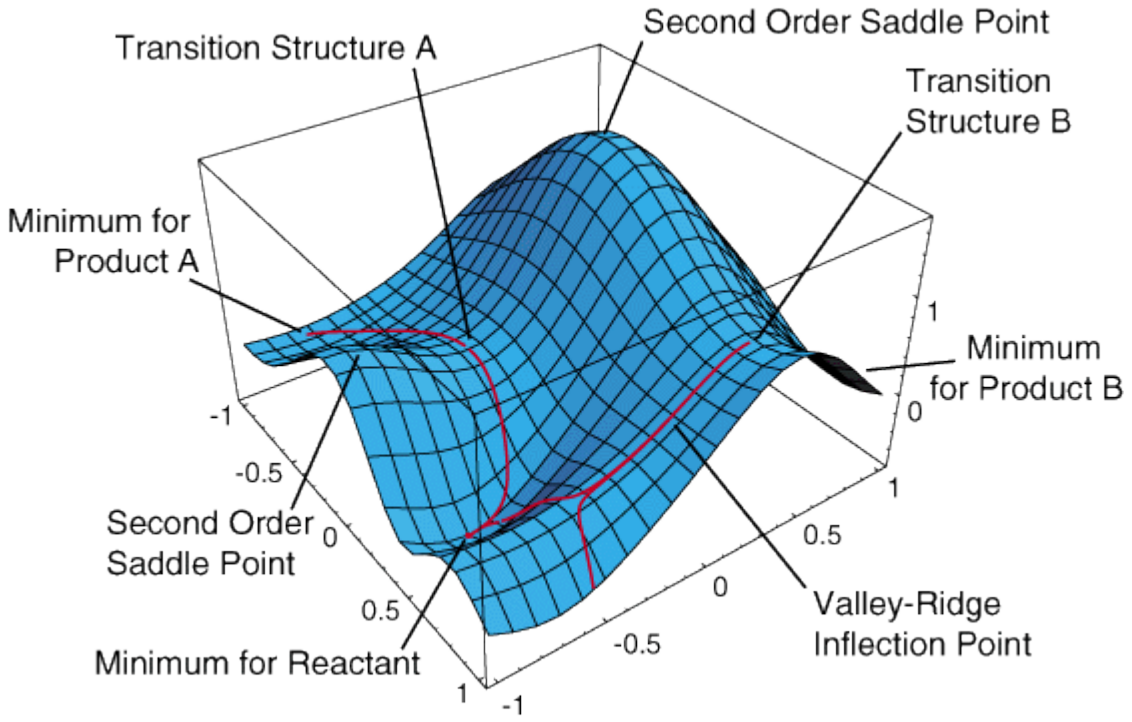


Figure 15. Characteristic potential energy surface showing the progress of the reaction

---

Source: http://www.chem.wayne.edu/~hbs/chm6440/PES.html

the repulsion term, resulting in the average effect of the repulsion rather than explicitly treating the repulsion interaction terms. As a consequence, the energy values calculated using the Hartree-Fock method are always greater than or equal to the exact energy and approach a limiting value as the basis set is varied. The other major approximation used in the Hartree-Fock method, is the definition of the wavefunction of the system by some mathematical function, which is exactly known for only a few electron systems. The type of mathematical functions used to describe the wavefunction for an electron can be classified in terms of basis sets, which can be either Gaussian type or slater type functions. The primary steps in the Hartree-Fock procedure involve an initial guess for the orbital coefficients, usually using a semi-empirical method. This function is used to calculate new orbital coefficients and the energy of the system, which can then be used to compute the same parameters and so on. This procedure continues iteratively until the energies and the orbital coefficients calculated in the different iterations are constant. This iterative procedure is known as the self-consistent field procedure. The following equations are the Hartree-Fock equations where F is the fock operator, acting on the one electron wavefunction which generates the energy value times the wavefunction.[83]

$$F\psi_1(1) = E_1\psi_1(1) \quad (13)$$

$$F\psi_2(1) = E_2\psi_2(1) \quad (14)$$

.

.

$$F\psi_n(1) = E_n\psi_n(1) \quad (15)$$

## 3.3 Density Functional Theory

The basic concept behind Density Functional Theory (DFT) is that the energy of the molecule can be determined from the electron density instead of its wavefunction. This theory was based on the theorem given by Kohn and Hoenburg, in which they used the electron density to determine the ground state energy of the molecule. According to (DFT), the electron density is expressed as the linear combination of basis functions which are similar to the HF orbitals. These basis functions are then expressed in the form of determinants, known as Kohn-Sham orbitals. The electron density given in these determinants is thus used to compute the energy of the system. A density functional is used to compute the energy from the electron density. A functional is usually a function of a function. The functionals can be derived from basic principles of quantum mechanics or by parameterizing the functions to match the exact experimental results. Density functionals can be divided into several different classes, which include both the effect of electron exchange as well as electron correlation. The most important and accurate class of functionals involve functionals which utilize the electron density and its gradient. These type of functionals are known as gradient corrected functionals. In addition, there are hybrid functionals which combine different functional forms from other methods including those from Hartree-Fock methods involving the exchange integrals, to provide the best understanding of the system properties. The advantage of using the density functional theory or electron density for energy calculations is that the integrals for the coulombic repulsion over the electron density, requires a scaling of $N^3$, with some contribution from electron correlation. Thus, the results are faster and accurate in comparison to the Hartree-Fock methods which requires the scaling of $N^4$ or higher.[84]

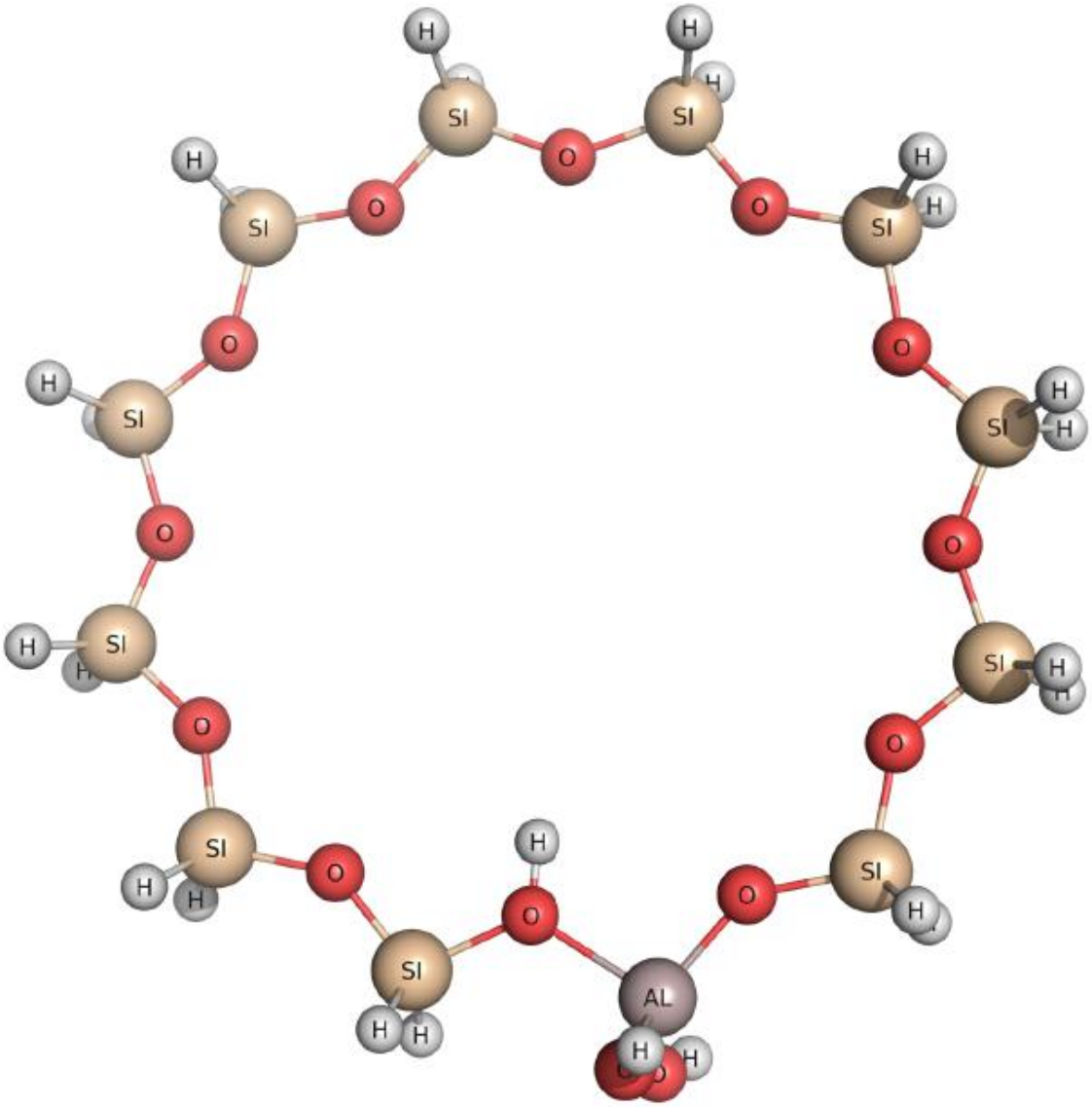


Figure 16. T12 Cluster model used for the quantum calculations of zeolites.

There have been several studies on the quantum calculation on zeolitic models. The literature precedent shows different approaches to model the zeolites, the most common of which is the cluster model. Several groups have used cluster models of zeolites such as ZSM-5, HY, BEA to address problems such as acidity of Brönsted/Lewis acid-base sites, and catalytic activity of the zeolites. In our studies, the approach of cluster model has been used in order to understand the interactions and the orientations of the drug molecules inside the micropores of the zeolite HY. Figure 16 shows one of the cluster models used in our studies. Since the size of the cluster is critical, two cluster models of different sizes were used to represent the zeolite framework.

## 3.4 Molecular Dynamics Simulations

Molecular dynamics is the time-dependent behavior of the molecular system, involving the properties such as vibrational motion or Brownian motion. The energy of the system is calculated based on the principles of molecular mechanics calculations and the energy thus calculated is then used to calculate the different forces acting on the atoms in a given molecular system. The steps involved in a typical molecular dynamics simulation are highlighted below.

Since the above process requires the use of force-field parameters, each system can be described with a set of force field parameters or functions which includes information regarding the system and its form of interactions. There are several algorithms in the literature to perform the numerical integration of the system. The most common algorithm is the Verlet algorithm because it is very fast in computational time and efficiency. The Verlet algorithm uses the positions and accelerations from the previous step to compute the positions and accelerations for the next step and so on.

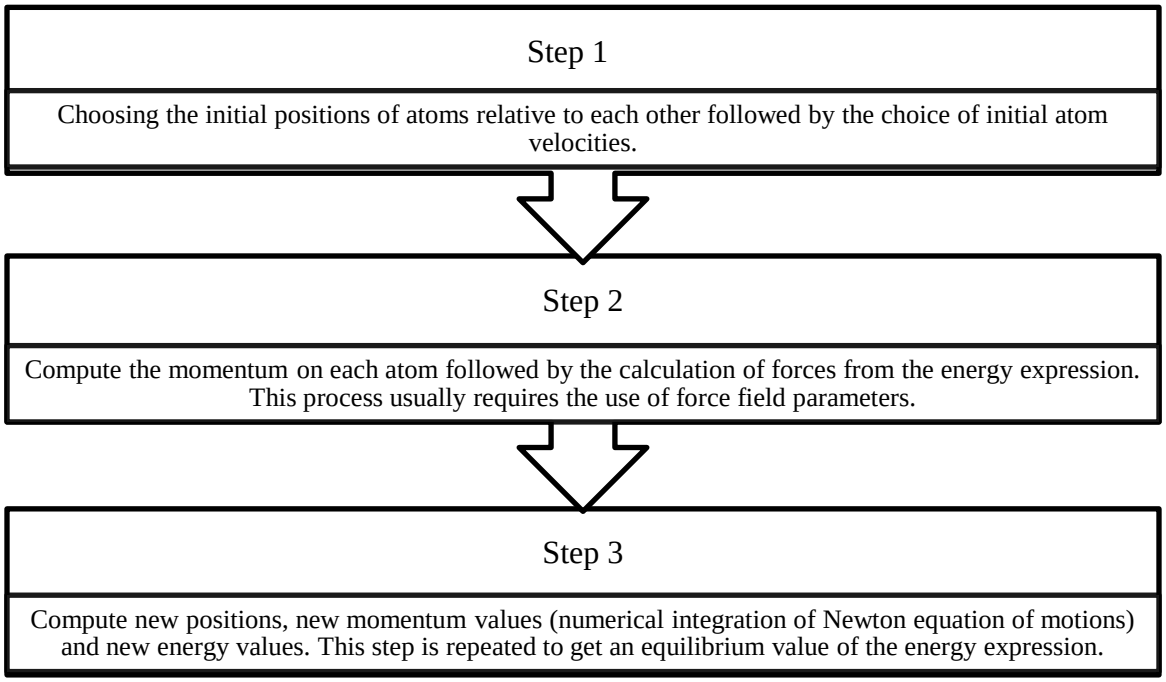


This explanation of molecular dynamics simulations provides a brief introduction to the main theory and concepts. The detailed anaylsis and mathematical description of force field parameters, verlet algorithm, and periodic boundary conditions are given in the literature.[85,86]

The use of molecular dynamics simulations in the case of mesoporous silica is very important in order to understand the physio-chemical processes occuring inside the porous structure. There have been several reports in the literature which show the successful use of molecular dynamics simulations in understanding the nature of interactions of molecular systems such as benzene, ionic liquids with mesoporous silica. The use of molecular dynamics simulations in the field of drug delivery has not been explored yet to the best of our understanding. With the available tools and resources, we have simulated the mesoporous silica which is in close agreement with the literature and mimics the experimental system, used in drug delivery studies. This type of calculation helped us in understanding the nature of interaction of the drug molecules inside the

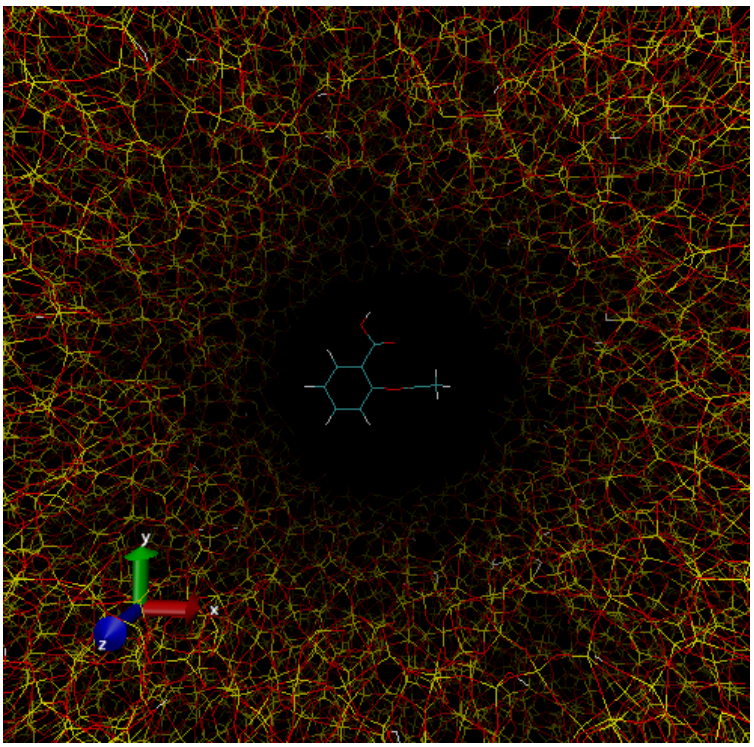


Figure 17. Snapshot of the orientation of aspirin inside the pores of mesoporous silica during a MD simulation.

mesoporous silica. Figure 17 shows the presence of aspirin inside the pores of mesoporous silica.

# CHAPTER 4

# AN EXPERIMENTAL AND COMPUTATIONAL STUDY OF THE LOADING AND RELEASE OF ASPIRIN FROM ZEOLITE HY

## 4.1 Abstract

The anti-inflammatory drug, aspirin, was loaded into three zeolite HY hosts with silica to alumina ratios ($SiO_2/Al_2O_3$) of 5, 30 and 60. The aspirin loading in the zeolite HY samples as measured by thermogravimetric analysis decreased from 106, to 78, to 69 mg aspirin/g zeolite with increasing $SiO_2/Al_2O_3$. The surface areas and pore volumes, measured using nitrogen adsorption-desorption experiments, indicated that the aspirin was loaded into the internal pore surface of these materials. The Fourier Transform Infrared (FTIR) and $^{27}Al$ and $^{13}C$ Magic Angle Spinning Nuclear Magnetic Resonance (MAS NMR) spectra of the aspirin-loaded materials provided molecular level information about aspirin–zeolite interactions. Quantum calculations at both Hartree-Fock (HF) and Density Functional Theory (DFT) levels of theory were conducted in order to understand the nature of intermolecular interactions between the zeolite host and the aspirin. The release of the aspirin from HY was dependent on the hydrophobicity of the zeolite host with more hydrophobic zeolites (higher $SiO_2/Al_2O_3$) releasing the aspirin less readily.

## 4.2 Introduction

Controlled drug delivery requires the optimal release of the drug in efficient amounts while minimizing the side effects that can occur depending on the dosage forms. The conventional dosage forms of various drug molecules may lead to adverse side effects, such as diarrhea and/or nausea, which can be minimized or reduced using drug

delivery methods. Drug delivery systems, such as polymeric systems and mesoporous silica materials, have exhibited potential for application as drug delivery carriers and a great deal of work has been done to explore this potential.[56-58,68,87,88] Relatively fewer studies have been reported exploring the potential of zeolites in drug delivery.

Zeolites are inorganic crystalline materials comprised of silicon, aluminum and oxygen in the three-dimensional structure. The substitution of silicon by aluminum atoms in the framework requires the presence of charge compensating counter-ions in these materials, such as $Ca^{2+}$, $Na^{+}$, $H^{+}$, $K^{+}$ or transition metal elements which impart unique ion-exchange properties.[89] Due to the defined pore structure and pore geometry, zeolites can be used for size selective adsorption and separation of molecules.[90-92] The presence of aluminum leads to the formation of defects in these materials and as a result, zeolites are active catalysts for a number of chemical reactions, such as hydrogenation reactions.[93] The structure of zeolite Y is shown in Figure 18. The sodalite cage is outlined in green and the dimension of the supercage is indicated with the dashed line.

The advantages of using zeolites for biomedical applications, such as the delivery of small drug molecules, are the biocompatibility and low toxicity of zeolites,[94-96] the smaller pore size (relative to mesoporous silica) that more closely matches the drug molecule size relative to mesoporous silica materials and the ability to tune the zeolite properties by varying the $SiO_2/Al_2O_3$ ratio, the exchangeable cation and or the surface functional group.[97,98] There are several examples of biomedical applications of zeolites reported in the literature including imaging,[10,11,13,99-102] wound treatment[103] and drug delivery.[14-18,104-106] These examples demonstrate that different zeolites can be exchanged with cations, functionalized or loaded with drug molecules for specific

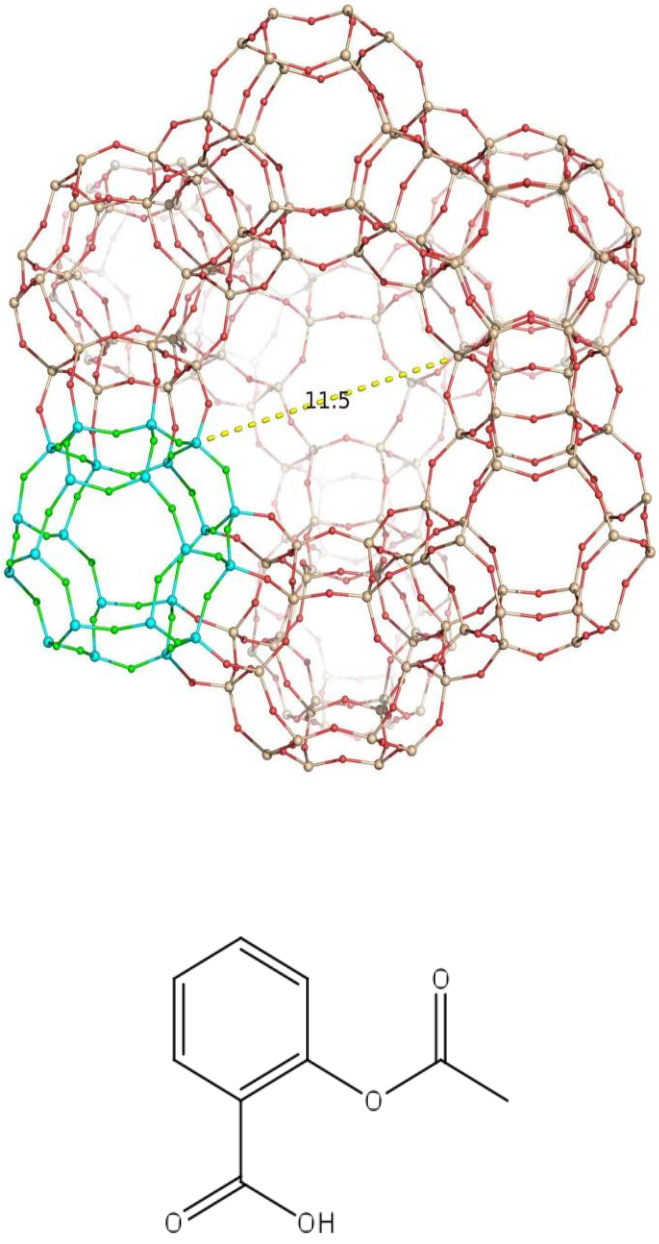


Figure 18. Zeolite Y (top) and aspirin (bottom) structures

biomedical applications. In examples of drug-loading, Zeolite Y/magnetite nanocomposites[105] have been loaded with doxorubicin molecules and paraquat molecules have been loaded into trimethylsilyl functionalized zeolite Y.[17] Recently, the adsorption of sulfonamide antibiotics on zeolite Y has been investigated. [14,15,101-108] The loading and release of anthelminthics and other drugs from zeolites have produced a controlled release of these molecules.[109] For example, dealuminated zeolite Y has been successfully used in the controlled delivery of ibuprofen.[55] Further research is needed to understand fundamental zeolite and drug molecule interactions so that the loading and release of the drug molecules can be better understood and controlled.

Aspirin will be used as a model drug in this study. Aspirin is primarily used for the treatment of cardiovascular diseases[110] and as a non-steroidal anti-inflammatory drug which acts by inhibiting the enzyme cyclooxygenase.[111] The molecular dimensions of the aspirin molecule shown in Figure 18 are 8.1 Å X 6.5 Å X 3.6 Å which indicate that aspirin is capable of entering the pores of zeolite Y and interacting with the supercages, which are 11.5 Å in diameter. In the study reported here, the loading and release of aspirin from zeolite HY samples with different silica to alumina ratios (5, 30 and 60) was investigated. Understanding the role of aluminum will be useful in tailoring drug delivery systems because the properties of zeolites, such as hydrophilicity/hydrophobicity, depend on the $SiO_2/Al_2O_3$ ratio.[112] Spectroscopic methods, including Fourier Transform Infrared (FTIR) and $^{27}Al$ and $^{13}C$ Magic Angle Spinning Nuclear Magnetic Resonance (MAS NMR), and theoretical calculations were conducted to elucidate the aspirin/host interactions and the zeolite properties that control the loading and release.

## 4.3 Experimental Section

### 4.3.1 Sample Preparation

Three zeolites with different $SiO_2/Al_2O_3$ were purchased from Zeolyst International, CBV100 ($SiO_2/Al_2O_3$=5) and CBV720 ($SiO_2/Al_2O_3$=30) and CBV760 ($SiO_2/Al_2O_3$=60). CBV720 and CBV760 had the charge-compensating cation as $H^+$ whereas the CBV100 had the charge-compensating cation as $Na^+$ and was hydrogen exchanged to prepare the H-form of zeolite Y. To H-exchange commercial zeolite NaY, 1 g of commercial zeolite Y was mixed with 0.1 M ammonium nitrate and was stirred for 24 h at room temperature.[113] The sample was centrifuged and washed twice with deionized water. The zeolite powder was dried in the oven at 100 °C overnight and calcined under oxygen flow at 550 °C for 6 h to obtain the H-form of commercial zeolite Y (HY-5). The other two zeolites with different silica to alumina ratios were used as received. The three HY samples will be referred to as HY-5, HY-30 and HY-60 indicating the $SiO_2/Al_2O_3$. Aspirin was used as obtained from Alfa-Aesar (99%).

### 4.3.2 Aspirin Loading and Release

Zeolite Y samples were mixed with aspirin dissolved in ether (25 mg/ml) and were stirred for 24 h at room temperature. The sample vials were sealed in order to prevent the evaporation of the solvent. Before the aspirin loading, the zeolite powders were pretreated at 120 °C for 8 h to activate the zeolite and to remove the physisorbed water from the zeolites. After stirring, the solutions were centrifuged for 20 minutes at 14000 rpm and thoroughly washed with ether twice in order to remove excess aspirin. The amount of aspirin loaded was measured using thermogravimetric analysis (TGA). Known amounts of the aspirin-loaded zeolite were mixed (1 mg/ml) with simulated body

fluid at pH 7.4 and 37 °C. The simulated body fluid was made using known amounts of sodium monobasic phosphate and sodium dibasic phosphate. The samples were stirred at ca. 100 rpm and 2 ml aliquots were removed at regular intervals. The aliquots were centrifuged in order to ensure no solid was in suspension and the supernatants were analyzed for aspirin with UV –Vis spectroscopy (Varian Cary 100 Scan) at λ= 296 nm. The amount of released aspirin was calculated using the following equation:

$$C_{tcorr} = C_t + \frac{v}{V}\sum_0^{t-1} C_t \qquad (16)$$

where $C_{tcorr}$ is the corrected concentration at time t (corrected to account for changes in volume), $C_t$ is the apparent concentration at time t, v is the volume of the sample taken, and V is the total volume of the solution. Experiments were conducted in duplicate and the values were averaged.

### 4.3.3 Theoretical Methods

All calculations were performed with the Gaussian09 package.[114] The 6-31+G(d,p) polarized diffuse split-valence basis set was used. This basis set was chosen to facilitate comparison with the literature for similar zeolite models. For the DFT calculations, the B3LYP functional was used. The zeolite was represented using the zeolite T12 cluster model composed of 12 tetrahedral atoms of the framework respectively.[115-117] The T12 cluster was optimized at HF and DFT (B3LYP) levels of theory with 6-31+G(d,p) basis set. The vibrational frequencies for the T12 cluster models with aspirin and aspirin anion were calculated using HF level of theory. Typically, the scaling factors for scaling the vibrational frequencies range from 0.87 for HF to 0.95 for MP2 calculations. The C=O stretching frequencies for –COOH and $–COO^-$ were scaled using the scaling factor of 0.87 which is optimum for HF level calculations.[105]

## 4.4 Characterization

The zeolites were characterized using a variety of different techniques. The zeolite crystallinity was confirmed using powder X-ray diffraction (pXRD) (Siemens D5000 X-ray diffractometer with Cu Kα and a nickel filter). A broad-range pattern (2θ = 5 to 55 with a 0.04 step size, 1 s/step) was collected for the parent zeolite and the aspirin-loaded zeolites to confirm the crystal phase.

Surface areas of the parent and aspirin loaded zeolite Y samples were measured using nitrogen adsorption and the BET method on a Nova 1200 Nitrogen Adsorption Instrument (Quantachrome). Typically, 100 mg of zeolite powder was dried overnight at 120 °C in vacuum. A 7-point BET isotherm was then recorded and the specific surface area was calculated for the samples ($S_{tot}$). A 50-point adsorption/desorption isotherm was measured and used for calculation of total pore. The total pore volume ($V_{tot}$) was calculated by measuring the amount of adsorbed nitrogen at 0.97 $P/P_o$.

Thermogravimetric analysis (TGA) was performed using the TA Q5000 TGA instrument with a heating rate of 5 °C/min under nitrogen flow. While samples were heated from room temperature to 800 °C, the weight change was recorded. The TGA data was used to calculate the aspirin loading.

FT-IR spectra were recorded using the Nicolet FT-IR spectrometer and the samples were pressed into disks by mixing them in the ratio of 1:5 with KBr. The spectra were recorded in the range of 400-4000 $cm^{-1}$.

Nuclear magnetic resonance (NMR) experiments were conducted on a 500 MHz Bruker Avance III spectrometer with 3.2 mm zirconia rotors. $^{27}Al$ Magic Angle Spinning (MAS) NMR experiments were conducted on both drug loaded and parent zeolite

samples. $AlCl_3$ was used as a chemical shift reference for $^{27}Al$ NMR. The spinning speed for all $^{27}Al$ experiments was 30 kHz. $^{13}C$-$^{1}H$ cross polarization magic angle spinning (CPMAS) experiments were conducted on the aspirin-loaded zeolites with a 3.2 mm rotor. The spinning speed for all $^{27}Al$ experiments was 30 kHz. The $^{13}C$-$^{1}H$ CP-MAS experiments were conducted with the MAS spinning speed of 10 kHz with adamantane as the reference material.

## 4.4 Results and Discussion

### 4.4.1 Physicochemical Characterization of Parent and Aspirin-loaded Zeolite Y

The zeolite Y samples were characterized using several different techniques before and after aspirin loading. Representative powder X-ray diffraction patterns of the zeolites were obtained (Figure 19) and characteristic peaks corresponding to zeolite Y were observed. The powder X-ray diffraction patterns indicate that the characteristic crystalline structure of zeolite Y was preserved after drug loading, with the powder patterns similar to the parent zeolite.

Representative thermal gravimetric analysis (TGA) data for the pure aspirin and aspirin-loaded zeolite are shown in Figure 20. Two distinct weight changes are seen in the TGA data for pure aspirin (inset) around 140 °C and 260 °C which can be attributed to the onset of melting followed by the decomposition of the aspirin molecule.[16] In case of drug-loaded zeolite HY-5, the weight change is extended over the entire temperature range and extends to 650 °C. This observation can be attributed to the interaction of the carboxylic groups of aspirin with the framework of the zeolite causing the weight loss to occur at higher temperatures relative to pure aspirin. A small weight loss was also seen at

~ 130 °C which is attributed to the presence of physisorbed water (and/or ether) in the zeolite. The aspirin loading calculated from the TGA data is listed in Table 1 and ranges from 69 mg/g for HY-60, to 78 mg/g for zeolite HY-30 and 106 mg/g for HY-5. The aspirin loading corresponds to approximately 0.6, 0.6 and 1.0 aspirin molecule per supercage for HY-60, HY-30 and HY-5, respectively. The TGA data indicates that the highest aspirin loadings of 1 aspirin per supercage are achieved for the lowest $SiO_2/Al_2O_3$ and correspondingly greatest hydrophilicity of the zeolite Y.

The nitrogen adsorption-desorption isotherms were measured for the parent zeolite and the aspirin loaded zeolite samples to measure the surface areas and pore volumes. Representative isotherms for zeolite HY($SiO_2/Al_2O_3$=5) with and without aspirin are shown in Figure 22 and surface area and pore volume data is listed in Table 1. The surface areas of the zeolite Y samples range from 594 to 711 $m^2/g$. After aspirin loading, the surface areas decrease by approximately 30-40% indicating that the internal zeolite pores are occupied by aspirin molecules. A corresponding decrease in the pore volume of the aspirin-loaded zeolites relative to the parent zeolites by approximately 50% is also observed which correlates with the presence of aspirin molecules inside the zeolite pores.

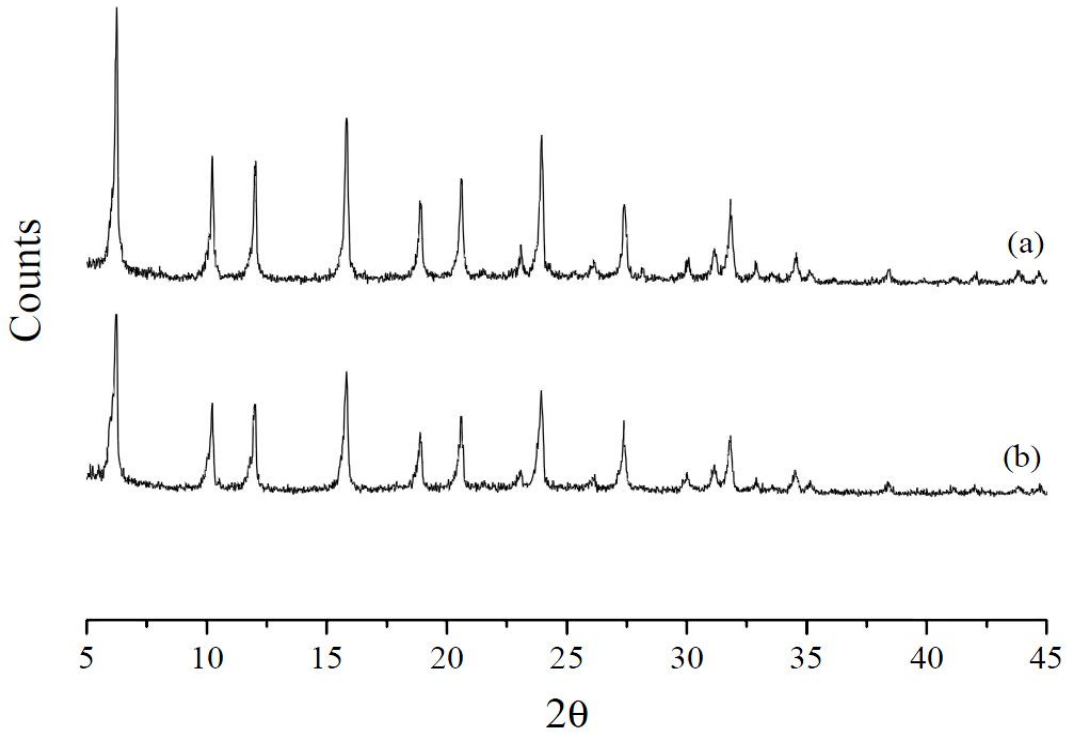


Figure 19. Powder X-ray diffraction patterns of a) parent zeolite Y (HY-5) and b) zeolite Y (HY-5) with aspirin

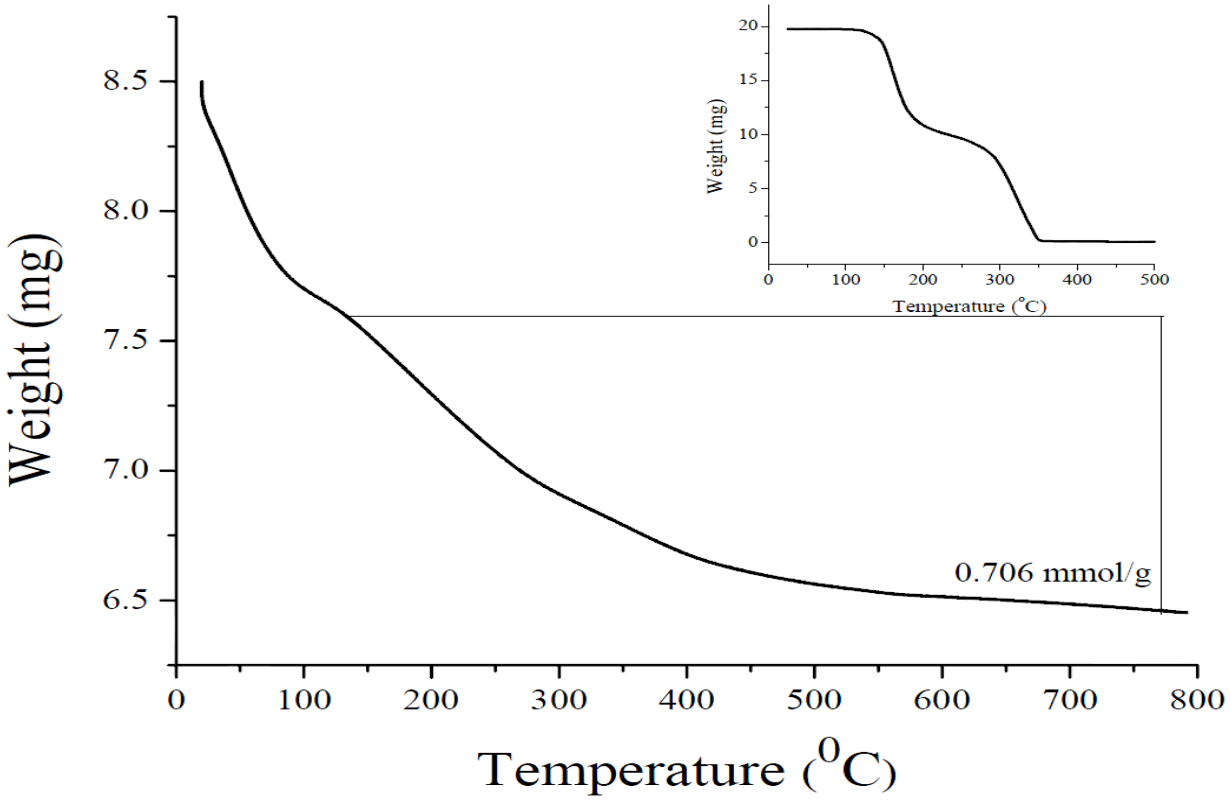


Figure 20. Thermogravimetric Analysis of aspirin loaded zeolite (HY-5); the inset shows the thermogram of the pure aspirin.

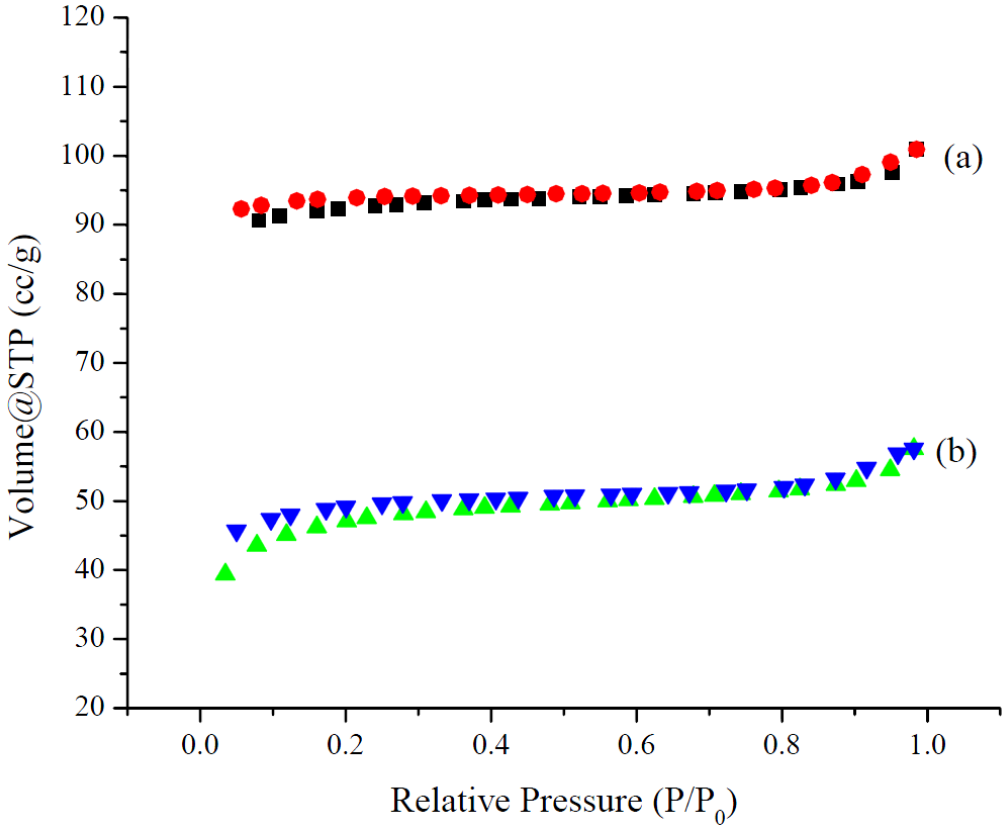


Figure 21. Nitrogen adsorption-desorption isotherm measurements for a) zeolite Y (HY-5) and b) aspirin loaded zeolite HY-5. (representative adsorption isotherms shown in green and black and representative desorption isotherms shown in blue and red).

Table 1. Physicochemical properties of the zeolites before and after aspirin loading

| | $SiO_2/Al_2O_3$ | $V_{pore}$ before (after) aspirin loading, ($cm^3/g$) | SA before (after) aspirin loading ($m^2/g$) | Aspirin loading (mg/g)[a] | # of aspirin molecules per supercage | Drug remaining after release (mg/g)[b] |
|---|---|---|---|---|---|---|
| HY-5 | 5 | 0.26 (0.11) | 594 (232) | 106 | 0.97 | -- |
| HY-30 | 30 | 0.30 (0.18) | 688 (440) | 78 | 0.63 | 29 |
| HY-60 | 60 | 0.31 (0.16) | 711 (396) | 69 | 0.56 | 23 |

### 4.4.2 FTIR and Solid State NMR Characterization

The difference FT-IR spectra (with the parent zeolite subtracted) for pure aspirin and aspirin-loaded zeolite are shown in Figure 22. Figure 22 shows the region from 1300-1800 $cm^{-1}$ which includes many of the characteristic vibrational modes for aspirin. Peaks at ~1750 and 1690 $cm^{-1}$ are observed for pure aspirin and are assigned to the ester and carboxyl acid C=O vibrational modes ($\nu_{C=O}$), respectively.[118] For the spectra of HY-30 and HY-60 with aspirin (Figure 22c, d), a prominent peak at ~1680 $cm^{-1}$ is observed that is assigned to the carbonyl band of the carboxylic acid group, but it is shifted relative to the carbonyl peak for the carboxylic acid of the pure aspirin sample. This is attributed to the interaction of carboxylic acid group of aspirin with the zeolite most likely due to a hydrogen bonding interaction. The ester group could also be involved in hydrogen bonding and appears to shift also as evidenced by the shoulder in the spectra at ~1720 $cm^{-1}$.

The FTIR difference spectrum for HY-5 with aspirin appears quite different in that the strong band at 1680 $cm^{-1}$ is not observed, but broad bands are observed at ~1608 and 1476 $cm^{-1}$. These vibrational bands are assigned to the antisymmetric and symmetric stretches ($\nu^{as}_{COO^-}$ and $\nu^{s}_{COO^-}$), respectively, of the carboxylate form of aspirin. This is consistent with previous FTIR studies of various acids adsorbed on alumina surfaces such that carboxylate species were observed with similar vibrational frequencies to those observed in this study and the strong carbonyl band at ~1700 $cm^{-1}$ was not observed in the FTIR spectra.[119,120] In a previous study on ibuprofen on HY zeolites with different Si/Al, similar FTIR spectra were observed in that the lowest Si/Al sample exhibited an FTIR spectrum with bands at 1563 and 1468 and 1442 $cm^{-1}$ that were assigned to the

antisymmetric and symmetric stretches of a carboxylate group.[55] Based on the FTIR spectra, Vallet-Regi and coworkers proposed the formation of an ibuprofenate species in a bridging fashion with 2 aluminum atoms. Other studies of model acetate complexes have shown that the spacing ($\Delta\nu$) between the antisymmetric and symmetric carboxylate bands are indicative of the bonding to a metal center such that the magnitude of the spacing indicates whether the complex is unidentate or bidentate (bridging or chelating).[121] The $\Delta\nu$ of 132 $cm^{-1}$ observed here for aspirin on HY-5 indicates a bidentate species is being formed with zeolite aluminum in either a bridging (2 aluminum atoms) or chelating (one aluminum atom) model. The $\Delta\nu$ observed in our study lies intermediate between the $\Delta\nu$ typically observed for bridging and chelating species. Our results are consistent with these previous studies and the FTIR results suggest that for HY-5, the aspirin carboxylic acid group is deprotonated through an interaction with the zeolite aluminum species to form a carboxylate.

The hydroxyl group stretching region of the difference FTIR spectra for the zeolites with aspirin are shown in Figure 22. Two main peaks are observed in the FTIR spectra at 3640 and 3739 $cm^{-1}$. These –OH peaks are assigned to O–H groups attached to extraframework aluminum (EFAL) and Si–OH (silanol) groups, respectively.[9] The peaks appear as negative peaks indicating a loss of –OH groups corresponding to Si–OH and/or EFAL–OH presumably due to interactions of these hydroxyl groups with the aspirin molecules. The loss of Si–OH is apparent in the HY-30 sample but not in the HY-5 and HY-60. The loss of EFAL–OH is observed for all three zeolite samples, although it should be noted that the amount of aluminum in HY-30 and HY-60 is reduced relative to

HY-5. For HY-5 with aspirin, the loss of the EFAL–OH peaks suggests that the bidentate carboxylate species involves EFAL species.

Further insight into the aluminum involvement with the aspirin was provided by $^{27}$Al NMR experiments. The $^{27}$Al MAS NMR spectra are shown in Figure 23. Two main peaks are observed in the $^{27}$Al MAS NMR spectra of the parent HY zeolites. The peak at ~60 ppm is assigned to tetrahedral aluminum and the peak at ~0 ppm is assigned to octahedral aluminum. [70,116-120,122-126] The absolute intensities in Figure 23 should not be compared because the samples contain different amounts of aluminum due to the different silica to alumina ratios. After loading with aspirin, the intensity of the octahedral aluminum peak decreases relative to the tetrahedral aluminum peak for HY-5, HY-30 and HY-60. The relative intensities and linewidths are provided in Table 2. The ratio of the intensity of the tetrahedral peak to the intensity of the octahedral peak increases by a factor of two for HY-30 and HY-60 after loading with aspirin. The intensity of the octahedral peak is very small for the parent zeolite, HY-5, so the decrease brings the intensity down to negligible levels and thus the ratio is undefined for aspirin on HY-5. These results suggest that after aspirin loading, the octahedrally coordinated aluminum present in the parent zeolite is converted to tetrahedrally coordinated aluminum. This octahedral to tetrahedral conversion for zeolite Y has been reported previously for ammonia adsorption.[103-105] An increase in the tetrahedral aluminum linewidth was also reported in that study consistent with our observations.[103] In the study by Vallet-Regi and coworkers, EFAL and framework aluminum species were also observed but the relative amounts of each differed compared to our samples.[55] This is

probably due to the different pretreatments for the samples which can affect the amount of EFAL in the sample.

The $^{13}C$ CP-MAS spectra in Figure 24a,b of HY-5 with aspirin loaded and for a physical mixture of HY and aspirin were also recorded and the presence of the peaks attributed to aspirin were seen in the aspirin sample. The peak around 18 ppm corresponds to the $–CH_3$ carbon and the aromatic ring carbons lie in the range of 100 – 155 ppm. The –C=O group carbons (carboxylic acid and ester) were also seen as the broad band in the CP-MAS spectra at ~170 ppm. The $^{13}C$ CP-MAS spectra for the aspirin loaded HY-5 shown in Figure 24b exhibits broader linewidths relative to the physical mixture of HY-5 and aspirin shown in Figure 24a. The increase in line-broadening is attributed to a decrease in motion for the loaded aspirin presumably due to interactions with the zeolite. In addition, the aromatic carbons in the drug loaded spectrum are shifted ~10 ppm in comparison to the physical mixture accounting for the interaction of phenyl group with the zeolite which is similar to what has been observed previously with polymeric and mesoporous silica hosts. [125-129]

### 4.4.3 Aspirin Release from HY

The release profiles for aspirin from zeolites, HY-5, HY-30 and HY-60 are shown in Figure 25a-c. Nearly complete release of aspirin is observed after ~300 minutes for HY-5. The release profiles for HY-30 and HY-60 are similar to each other with maxima of ~60% aspirin release after ~300 minutes. All three HY zeolites show similar initial burst rates of aspirin release with nearly 50% of the aspirin being released from the zeolite within the first hour.

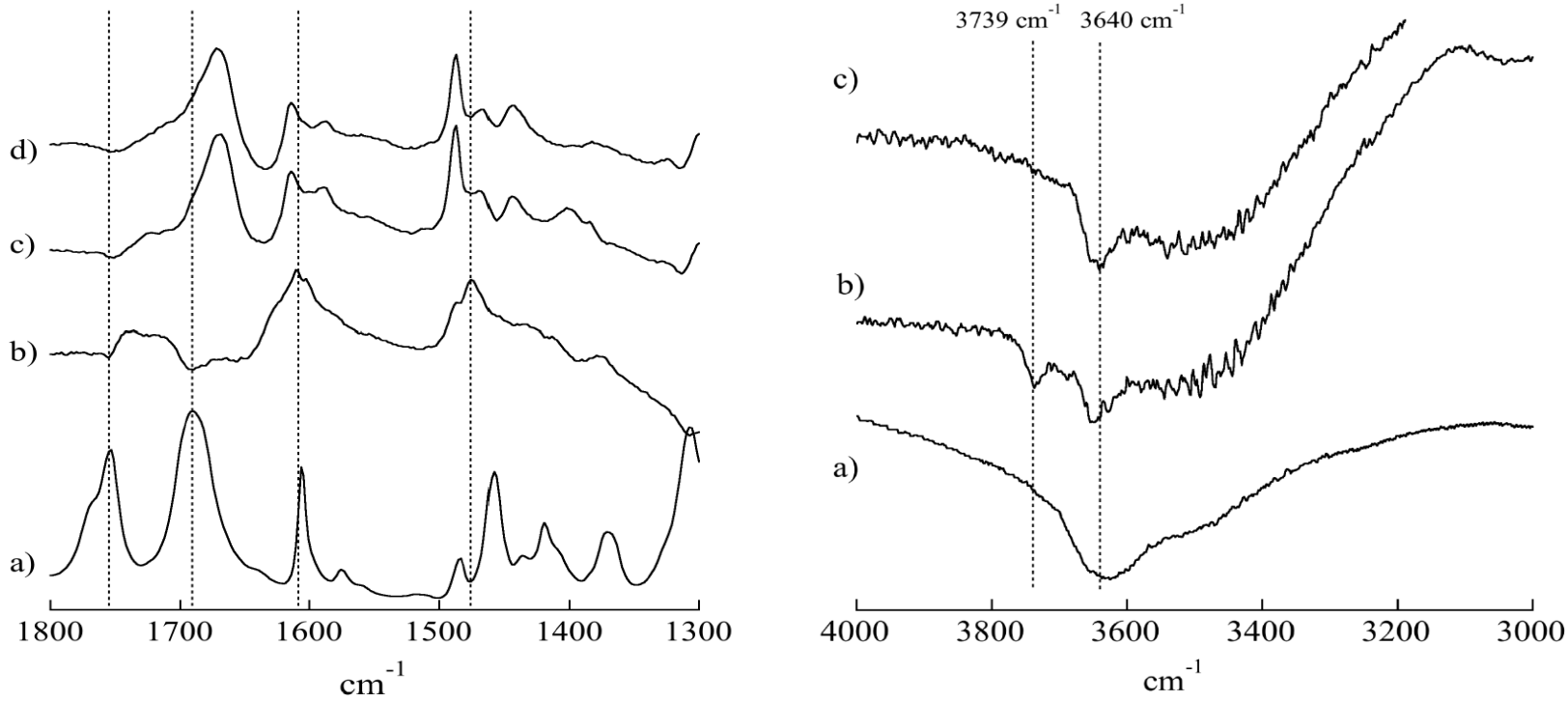


Figure 22. (left figure) FTIR spectra of a) aspirin, b) HY-5 with aspirin, c) HY-30 with aspirin and d) HY-60 with aspirin. The spectra in b-d are the difference spectra of the zeolite with aspirin with the spectrum of the zeolite alone substracted, (right figure) Difference FT-IR spectra of the hydroxyl group region for a) HY-5 with aspirin, c) HY-30 with aspirin and d) HY-60 with aspirin. The spectra in a-c are difference spectra of the zeolite with aspirin with the spectrum of the parent zeolite subtracted.

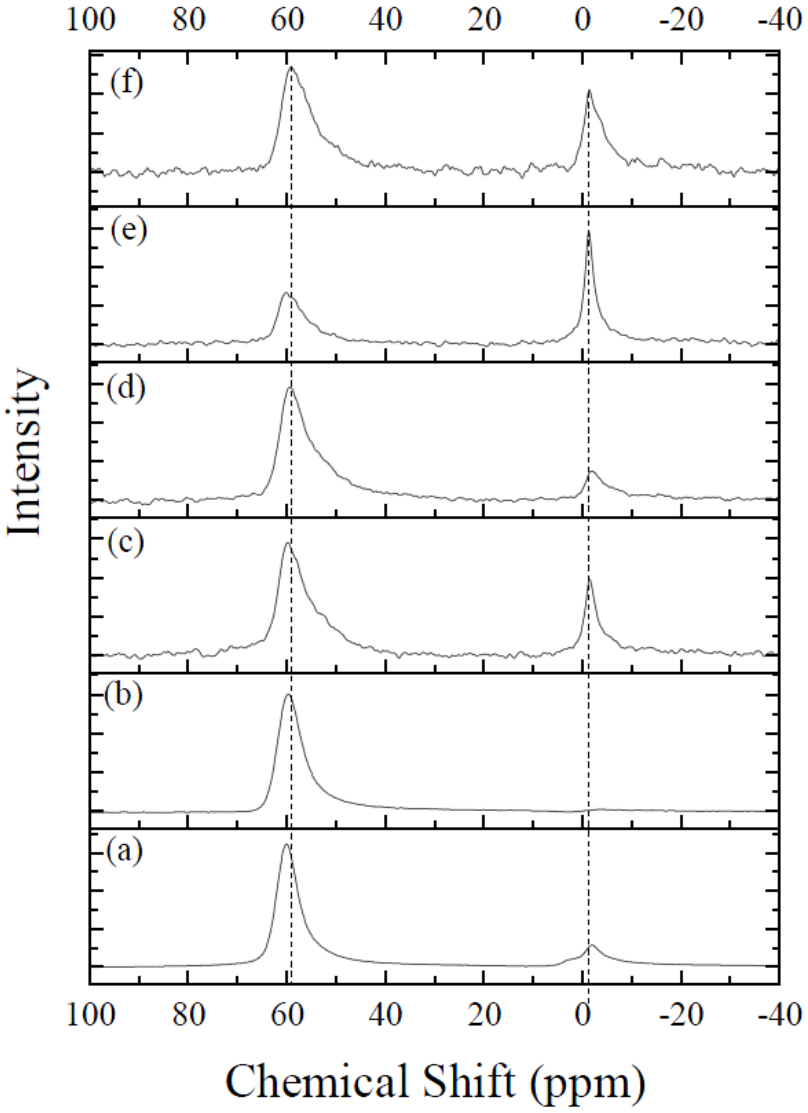


Figure 23. $^{27}$Al MAS NMR spectra for HY-5, HY-30, HY-60 before (a, c, e) and after loading with aspirin (b, d, f), respectively.

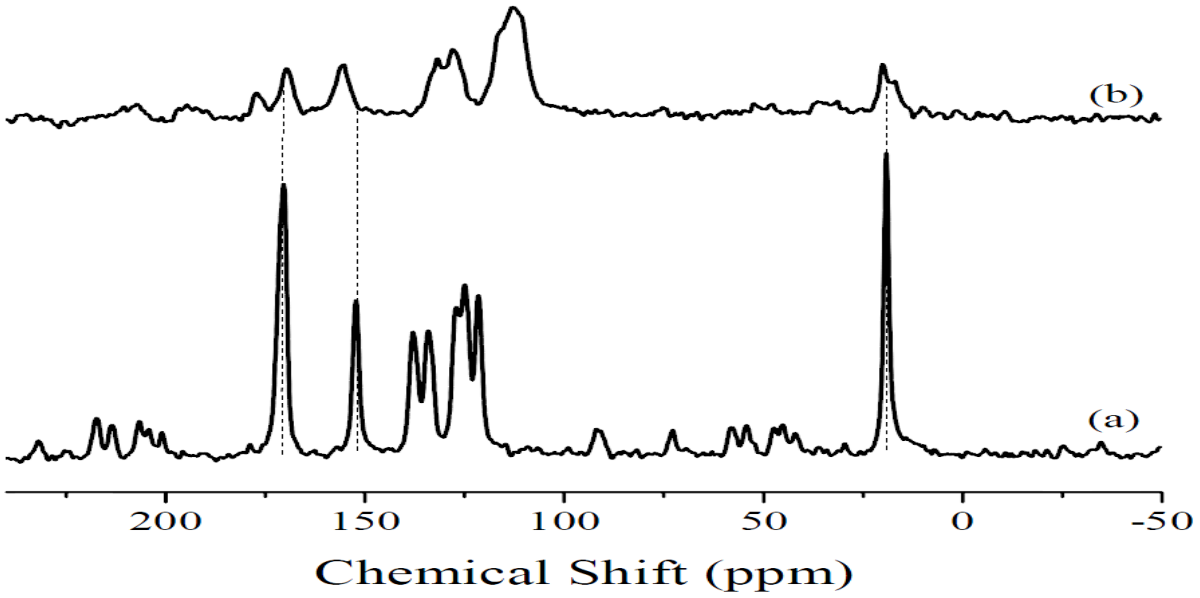


Figure 24. Representative $^{13}C$ CP-MAS NMR spectrum of (a) physical mixture of zeolite Y (HY-5) with aspirin, (b) drug loaded zeolite Y (HY-5) with aspirin.

Table 2. Relative integrated intensities and linewidths (Hz) from the $^{27}$Al MAS NMR spectra

| Sample | $I_{Td}/I_{Oh}$[a] | FWHM ($T_d$)[a] | FWHM ($O_h$)[a] |
|---|---|---|---|
| HY-5 (w/ aspirin) | 5.3 (--) | 2600 (2900) | 2700 (--) |
| HY-30 (w/ aspirin) | 2.9 (6.6) | 3400 (3500) | 1400 (2400) |
| HY-60 (w/ aspirin) | 1.0 (2.1) | 3100 (3500) | 1100 (2100) |

In the literature, there are several models that are used to fit data for drug release from a porous matrix.[106] In this study, the release data was fit using a first-order kinetic model involving an exponential decay:

$$Q = Q_{max}(1 - \exp(-k_1 t)) \qquad (17)$$

where Q is the amount of drug released in time t, $Q_{max}$ is the maximum amount of drug released and $k_1$ is the first order release constant.[121] The parameters $Q_{max}$ and $k_1$ obtained after fitting the release data in Figure 25 are listed in Table 3. $Q_{max}$ was ~100% for HY-5 and 63% for HY-30 and HY-60. The first order release rate constant, $k_1$, was 0.011, 0.032 and 0.028 $min^{-1}$ for HY-5, HY-30 and HY-60, respectively. The change in drug release rate constant for zeolites with high $SiO_2/Al_2O_3$ ratios can be interpreted in terms of the polarizability of the zeolite network. As the hydrophobicity of the zeolite increases, a van der Waals interactions becomes a contributing factor. Complete drug release for zeolite Y with the lowest $SiO_2/Al_2O_3$ ratio can be attributed to the hydrophilicity of the zeolite network, which results in the enhanced release of drug molecules in the buffer solution.[55]

Based on the data, it appears that the aspirin- aluminum complex that forms with the EFAL in HY-5 dissociates in aqueous solution. The patent literature indicates that the formation of aluminum aspirin is useful for sustained drug release in aqueous solution.[120] In a previous study of ibuprofen on zeolite Y, the HY sample with the lowest Si/Al exhibited the lowest release compared to the higher Si/Al ratio HY samples. They suggested that the aluminum ibuprofenate species is more strongly bound to the zeolite relative to the hydrogen bonded ibuprofen species in the higher Si/Al zeolites.

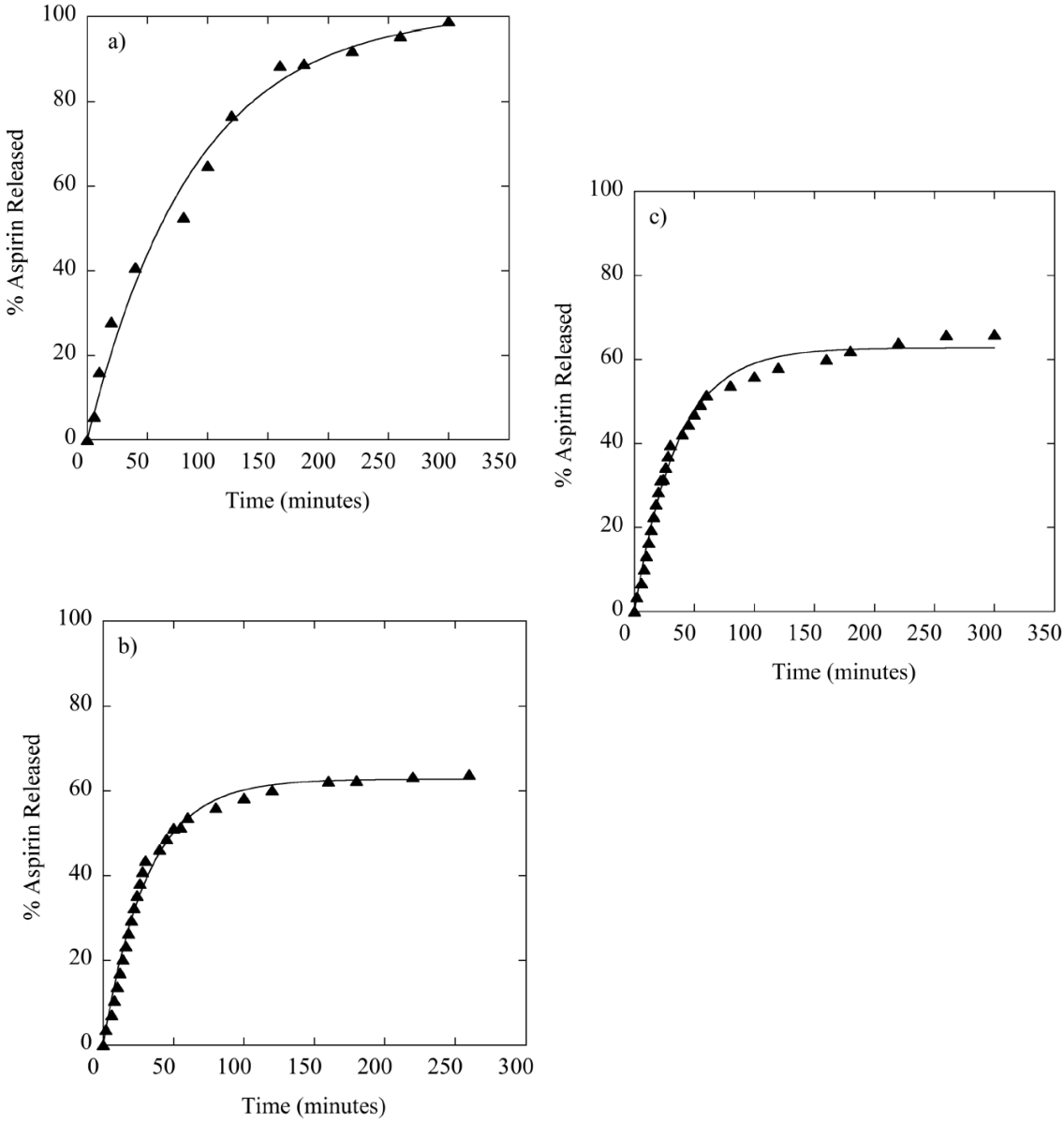


Figure 25. Aspirin release kinetics from a) HY-5, b) HY-30 and c) HY-60. The least squares fits to the function Q=Qmax[1-exp(-k1*t)] are shown by the solid lines. The release was measured at in phosphate buffer solution at pH=7.4.

Table 3. Fitted kinetic release parameters for aspirin release from HY

| Sample | $Q_{max}$,% | $k_1(min^{-1})$ |
|---|---|---|
| HY-5 | 101±4 | 0.011±0.001 |
| HY-30 | 62.8±0.9 | 0.032±0.001 |
| HY-60 | 62.8±0.8 | 0.028±0.001 |

The results reported here differ in that the aspirin aluminum species seems to be the most easily released. These apparent contradictions can be partly explained by the different hydrophobicities of ibuprofen and aspirin. Ibuprofen is more hydrophobic than aspirin and therefore, the release in aqueous solution may be hindered by this while the loading in the more hydrophobic higher Si/Al samples would be favored.

### 4.4.4 Computational Results

There are several methods for representing zeolite frameworks and active sites in computational chemistry studies that are described in the literature.[122] The active sites in zeolites refer to the defects that are created due to the incorporation of aluminum into the zeolite framework. When aluminum replaces silicon in the framework, a Bronsted acid site is formed. In a typical Bronsted acid site, a bridging hydroxyl ($-OH_p$) group is present. Several research groups have used small cluster models to model the zeolite.[106-108] For faujasite type zeolite Y, T3 and T12 cluster models have been used to represent the zeolite framework. It has been observed that the larger the cluster size, the more accurate the representation of the zeolitic framework.[107]

In this study, a T12 cluster model (shown in Figure 26a) was used to study the interaction of the aspirin molecule with the zeolitic framework. The T12 cluster consists of 11 Si atoms tetrahedrally coordinated with O atoms and one aluminum atom which were used to represent the 12 membered ring window of the zeolite. The tetrahedral coordination of the aluminum atom with the bridging $OH_p$ group gives a realistic interpretation of the zeolite structure and also incorporates the possible interactions with other framework atoms. The use of the larger cluster model significantly increases the

stabilization energy of the adsorption complex and provides an improved visualization of the structural dynamics of the system.[98]

The T12 cluster was optimized using both HF and DFT levels of theory. The bridging acid site in the models is characterized by Si-O, Al-O, O-$H_p$, Al-O-Si, and Al-O-$H_p$ bond lengths and bond angles. The optimized Al-O-Si and Al-O-$H_p$ bond angles indicate that the acidic proton is located in the same plane as the Si, Al, and O atoms. The HF and DFT results are very similar except for the bond lengths, which are longer for DFT relative to HF calculations as is generally the case. The results reported here are in close agreement with the literature results for similar clusters.[112,115-120] After the optimization of the cluster models, aspirin (and the aspirin anion) was added to the system and was allowed to optimize by varying the distance of aspirin with the zeolitic models (Bronsted acid site). The optimized aspirin-zeolite structure is shown in Figure 26 b,c and the aspirin anion zeolite structure is shown in Figure 26d. The cluster model energies of the zeolitic systems were found to be in close agreement with the literature.[107,108]

Table 4 lists the calculated (HF) and experimental vibrational frequencies for the model complexes. Frequency calculations were conducted for aspirin and the aspirin anion with the carboxylic acid group in the protonated and deprotonated (carboxylate) forms, respectively. The calculated $\nu_{C=O}$ for the carboxylic acid carbonyl group in aspirin is 1751 $cm^{-1}$ and decreases to 1691 $cm^{-1}$ for aspirin in the T12 cluster. Experimentally, the $\nu_{C=O}$ for the carboxylic acid carbonyl group in aspirin is 1690 $cm^{-1}$ and decreases to 1670 $cm^{-1}$ for aspirin in HY-30 and HY-60. The calculated antisymmetric and symmetric modes for the aspirin anion are 1624 and 1313 $cm^{-1}$ and

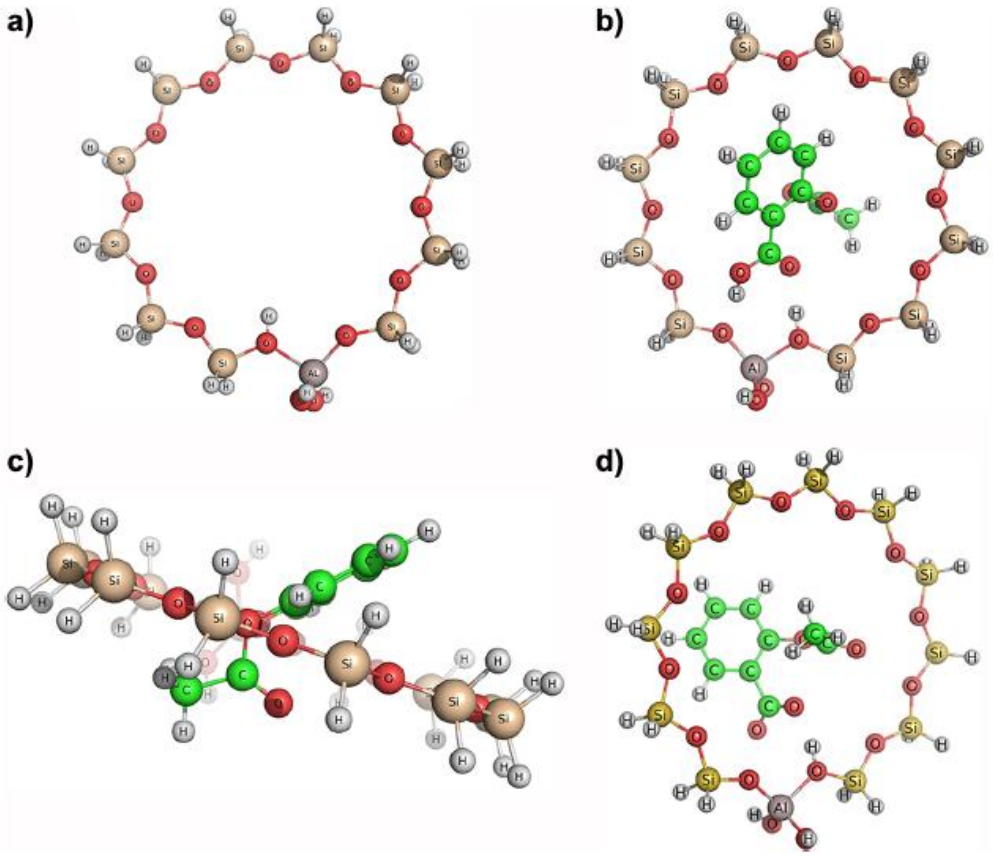


Figure 26. T12 cluster of zeolite Y geometry optimized a) without and b-c) with an aspirin molecule and d) with an aspirin anion. Two different views of the same cluster with aspirin are provided in b) and c).

Table 4. Calculated (HF) and experimental vibrational frequencies (FTIR) for aspirin and aspirin/zeolite Y

| System | $\nu_{C=O}$ ($cm^{-1}$) | $\nu^{as}_{COO^-}$ ($cm^{-1}$) | $\nu^{s}_{COO^-}$ ($cm^{-1}$) |
|---|---|---|---|
| | Calculated Frequencies[a] | | |
| Aspirin | 1751 | - | - |
| Aspirin anion | - | 1624 | 1313 |
| Aspirin in T12 | 1691 | - | - |
| Aspirin anion in T12 | - | 1596 | 1318 |
| | Experimental Frequencies | | |
| Aspirin[118] | 1706 | - | - |
| Aspirin anion [118] | - | 1609 | 1370 |
| Aspirin (this study) | 1690 | - | - |
| Aspirin/HY-5 (this study) | - | 1608 | 1476 |
| Aspirin/HY-30,60 (this study) | 1670 | - | - |

1596 and 1318 $cm^{-1}$ for the aspirin anion in the T12 cluster. Experimentally, for aspirin in HY-5, vibrational frequencies of 1608 and 1476 $cm^{-1}$ are observed in the FTIR spectra and are assigned to the antisymmetric and symmetric stretches of $COO^{-}$, respectively. The calculated vibrational frequencies support the interpretation of the experimental results and indicate that the carboxylic acid group is protonated for aspirin in HY-30 (HY-60) and that the aspirin anion forms in HY-5.[128]

## 4.5 Conclusions

Aspirin was successfully loaded into the pores of zeolite HY with 3 different $SiO_2/Al_2O_3$ ratios (5, 30, 60) and the loading of the aspirin was found to be highest in HY with the lowest $SiO_2/Al_2O_3$. FTIR and solid state NMR ($^{27}Al$, $^{13}C$ ) provided insight into the molecular interactions between aspirin and the zeolite. For HY-5, the formation of a bidentate aspirin anion complex was observed in FTIR. The aluminum MAS NMR suggested that the bidentate aspirin anion complex formed at extraframework aluminum sites in zeolite HY. For the higher $SiO_2/Al_2O_3$ HY zeolites, the aspirin was most likely bound to silanol sites via hydrogen bonding. The loss of the corresponding silanol peaks was observed in FTIR.

The release of the drug from the zeolite matrix at pH=7.4 in aqueous solution followed an exponential decay behavior. HY-5 exhibited nearly complete release of aspirin while HY-30 and 60 exhibited partial release of aspirin in aqueous solution at pH-7.4. The incomplete release was attributed to the increased hydrophobicity of the higher $SiO_2/Al_2O_3$ materials leading to increased Van der Waals interactions.

Theoretical calculations provided a better understanding of the orientation of the drug molecules inside the pore of the zeolite. A T12 model cluster was optimized with an

aspirin and an aspirin anion in the cluster. Calculations of the vibrational frequencies supported the interpretation of the FTIR data that the aspirin anion formed in HY-5 but that the aspirin remained protonated in HY-30 and HY-60.

The results of this work were published in Journal of Physical Chemistry C, 2012, volume 116, pages 21382-21390 and authored by Datt, Fields and Larsen.

# CHAPTER 5

# ASPIRIN LOADING AND RELEASE FROM MCM-41 FUNCTIONALIZED WITH AMINOPROPYL GROUPS VIA CO-CONDENSATION OR POSTSYNTHESIS MODIFICATION METHODS

## 5.1Abstract

A comprehensive study of aspirin loading and release from MCM-41 and amine functionalized MCM-41 was conducted. Two different functionalization methods, co-condensation and post-synthesis modification were utilized and compared. All of the MCM-41 samples were thoroughly characterized before and after aspirin loading by powder X-ray diffraction, nitrogen adsorption isotherms and thermal gravimetric analysis to determine the structure and physicochemical properties such as surface area, pore volume and functional group loading. Molecular level details about the aspirin-MCM-41 interactions were revealed through FTIR and $^{13}C$ solid-state NMR experiments. For the aminopropyl-functionalized MCM-41, the carboxylic acid group of aspirin associates with the amine group of the functionalized MCM-41. In all of the samples, an interaction between the aspirin phenyl group and the mesoporous silica host was hypothesized based on shifts in the phenyl group $^{13}C$ NMR resonances. Molecular dynamics simulations supported the NMR observations in that the phenyl group of the aspirin was determined to be oriented parallel to the pore wall. The release data indicated that both the distribution and loading of the amine functional groups in MCM-41 influenced the release properties of aspirin.

## 5.2 Introduction

A major issue in pharmaceutics is the incorporation of active drug molecules into inorganic materials for controlled release applications. Mesoporous silica materials are inorganic materials, which are synthesized in the presence of surfactants that act as templates for the polycondensation of silica species.[29,129,130] The mesoporous silica material, MCM-41 (Mobil Crystalline Material) is shown in Figure 27. Mesoporous silica materials have pore diameters ranging from 2-15 nm. The pore sizes can be varied during synthesis by varying time, temperature and the choice of the surfactant. High surface areas and large pore sizes make mesoporous silica an ideal material for hosting molecules of different sizes, shapes, and functionalities. Many examples of drug molecules loaded into mesoporous silica materials have been reported in the literature.[57,59,68,87,131-151] Ibuprofen has been extensively studied as a model drug adsorbed on the mesoporous silica materials, such as MCM-41, SBA-15 and hexagonal mesoporous silica (HMS) materials.[18,56,58,152] These mesoporous silica materials (MCM-41, SBA-15 and HMS) differ in their pore diameters, thickness of the walls and the specific synthetic conditions. Anti-cancer drugs have been studied for controlled release using mesoporous silica hosts. [68,153-157] Mesoporous silica is an attractive host due to properties, such as high surface areas, tunable pore sizes with narrow distributions, well-defined surface properties, low toxicity and very good biocompatibility. [150-159] Pore diameters, pore volumes, particle morphology and surface modifications are critical textural properties of mesoporous silica that control the drug loading and release properties. Modification with organic functional groups is an important

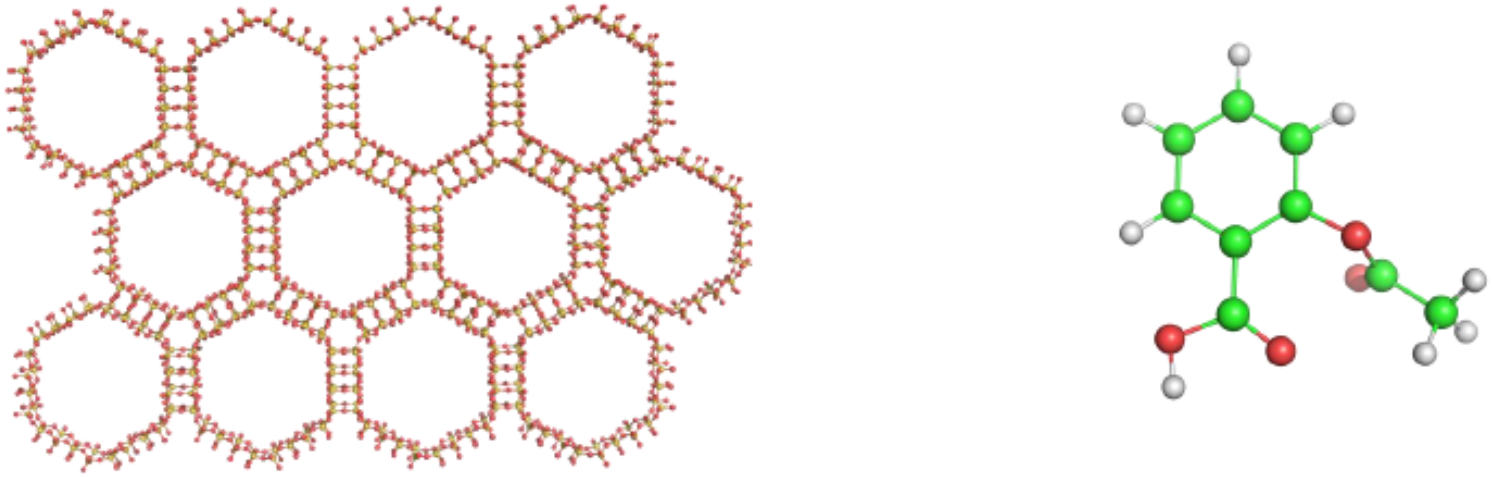

Figure 27. Schematic representations for mesoporous silica (left) and aspirin (right)

method of varying the drug loading and release properties of mesoporous silica materials. The drug molecule – organic group interaction and the location and number of organic groups on the surface are important factors in drug loading and release. Vallet-Regi and coworkers concluded that adsorption of drug molecules on mesoporous silica was related to "surface electrochemistry" whereas release of drug molecules was influenced by the surface area and diffusion through the pores.[157]

In general, mesoporous silica materials can be functionalized using two different methods: co-condensation and post-synthesis grafting as illustrated in Figure 28.[29] In the co-condensation method, an organosilane with the desired functional group is added during the synthesis so that the organic functionality is incorporated into mesoporous silica directly during the synthesis. In post-synthesis grafting, calcined mesoporous silica is treated with the organosilane that reacts with surface silanol groups. The distribution of functional groups varies depending on the method of modification. In the case of co-condensation, the functional groups are more evenly distributed throughout the mesoporous silica while in post-synthesis grafting, the functional groups are less regularly distributed. In post-synthesis methods, reaction of the organosilane at the opening of the mesopores can lead to a reduction in the diffusion of molecules into or out of the mesoporous silica.[29] The amount of loaded functional group can also be controlled by varying the amount of organosilane used during modification. The functional group loading can affect the surface area and the surface charge of the mesoporous materials. Amine functionalized mesoporous silica materials have been prepared by several groups for evaluation as drug delivery hosts.[60,157,158] Studies have addressed adsorption or release and factors such as the loading level of the amine group, the specific amine functionality,

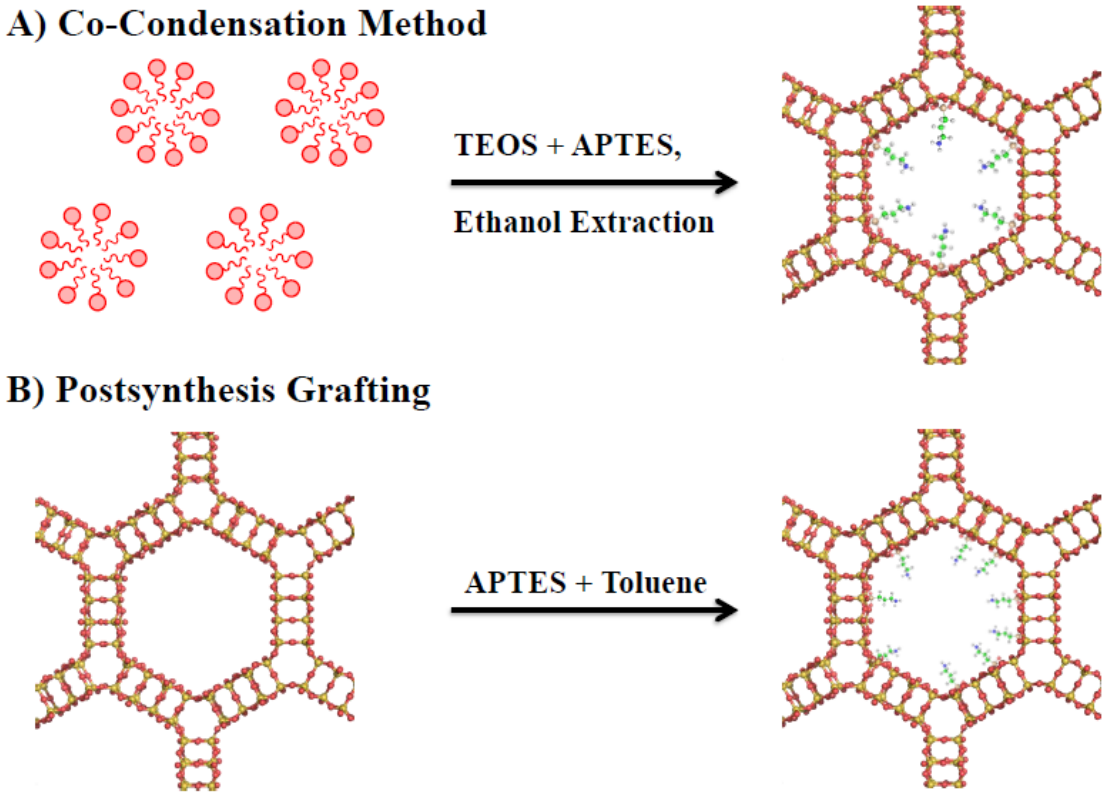


Figure 28. Different methods of functionalization (A) Co-condensation method, and (B) Postsynthesis grafting method

and the nature of the mesoporous silica host.

In the study reported here, aspirin (Figure 27) was chosen as a model drug due to its small molecular size, good pharmacological activity, and short biological half-life.[110,111] In addition, it has a carboxyl group that can interact with surface silanol groups or amino groups on the pore walls and may be useful for the controlled drug release. The loading and release of aspirin from MCM-41 modified with aminopropyltriethoxysilane (APTES) functional groups was investigated in order to develop a fundamental understanding of the interactions of aspirin with the mesoporous silica host and how these impact loading and release properties. Two modification methods, co-condensation and post-synthesis grafting, were evaluated and compared in terms of the effect on the loading and release of the model drug, aspirin. The MCM-41 materials were extensively characterized by powder X-ray diffraction (pXRD), thermal gravimetric analysis (TGA), and nitrogen adsorption for surface area and pore volume measurements. The aspirin loaded materials were characterized spectroscopically using FTIR and solid state NMR before and after aspirin loading. Molecular dynamics (MD) calculations were conducted to provide additional insight into the experimental results.

## 5.3 Experimental Procedures

### 5.3.1 Materials

3-Aminopropyltriethoxysilane (APTES, Sigma Aldrich), tetraethoxysilane (TEOS, Sigma Aldrich), hexadecyltrimethyl-ammonium bromide (CTAB, Sigma Aldrich), and acetylsalicylic acid (Aspirin, Alfa Aesar) were used as received.

### 5.3.2 Synthesis of MCM-41

The MCM-41 was prepared using cetyltrimethylammonium bromide (CTAB) as the surfactant, water as the solution and sodium hydroxide as a catalyst.[60] Tetraethyl orthosilicate (TEOS) was added as a silica source. The mixture contained a molar ratio of 1 CTAB: 7.564 TEOS: 2.551 NaOH: 4652 $H_2O$. The solution was then aged for 2 h until a white product formed. The product was filtered and washed with deionized water, and ethanol. It was then dried in an oven at 373k for at least 12 h. The dried product was heated with air to 600 °C for 6 h.

### 5.3.3 Co-condensation of APTES with MCM-41

The amine functionalization reaction was similar to the synthesis of MCM-41 except that in addition to the silicon source, the amine source (4 mmol and 8 mmol for CC-1 and CC-2 respectively) was added simultaneously. The contents were filtered, washed and dried in an oven overnight. The template removal was done through an extraction process to prevent the removal of the amine groups. In a typical extraction process, 1g of the material was mixed with ethanol and hydrochloric acid and stirred for 24 h. at room temperature. The resulting material was filtered, washed and dried.[29] These samples will be referred to as MCM-41-CC-1 and MCM-41-CC-2 for the lower and higher APTES loaded samples, respectively.

### 5.3.4 Post-synthesis grafting of the APTES on MCM-41

The post-synthesis grafting procedure involved refluxing 1 g of calcined MCM-41 and APTES (4 mmol or 8 mmol) in toluene at 120 °C for 6 h.. The resulting sample was filtered, washed with 1:1 mixture of dichloromethane and diethylether and dried in an

oven at 100 °C. These samples will be referred to as MCM-41-PS-1 and MCM-41-PS-2 for the lower and higher APTES loaded samples, respectively.

### 5.3.5 Aspirin Loading and Release

The mesoporous silica was loaded with the aspirin by mixing the aspirin in ether until it dissolved, then adding the MCM-41 with magnetic stirring for 12-24 h at 25 °C. The solution was filtered and dried at 25 °C overnight. For release profiles, 100 mg of the loaded MCM-41 was placed in a phosphate buffer solution with pH = 7.4 at 37.4 °C. The contents were stirred at approximately 100 rpm and 2 ml aliquots were removed at regular intervals of time. The aliquots were centrifuged in order to ensure no solid was in suspension and transparent supernatants were analyzed for aspirin with UV –Vis spectroscopy (Varian Cary 100 Scan) at λ= 296 nm. The amount of released aspirin was calculated using the following equation:

$$C_{tcorr} = C_t + \frac{v}{V}\sum_0^{t-1} C_t \qquad (16)$$

where $C_{tcorr}$ is the corrected concentration at time t (corrected to account for changes in volume), $C_t$ is the apparent concentration at time t, v is the volume of the sample taken, and V is the total volume of the solution.[58] Experiments were conducted in duplicate and the values were averaged.

## 5.4 Characterization

The textural properties of the MCM-41 materials were characterized using a variety of techniques. The MCM-41 structure was verified using powder X-ray diffraction (pXRD) (Siemens D5000 X-ray diffractometer with Cu Kα and a nickel filter). A broad-range pattern (2θ = 1 to 10 with a 0.04 step size, 1 s/step) was collected.

Surface areas and pore volumes of the MCM-41 materials were measured using nitrogen adsorption and a Nova 1200 Nitrogen Adsorption Instrument (Quantachrome). Approximately 100 mg of MCM-41 was dried overnight at 120 °C in vacuum. A 7-point BET isotherm and a 50-point adsorption/desorption isotherm were measured and used for calculation of the surface area and total pore volume. The total pore volume ($V_{tot}$) was calculated by measuring the amount of adsorbed nitrogen at 0.97 $P/P_o$.[159] The pore diameter of mesoporous silica was calculated using the literature reported relation given below:

$$W_d = cd\left(\frac{\rho V_p}{1+\rho V_p}\right)^{1/2} \quad (2)$$

where $W_d$ is the pore size, $V_p$ is the primary mesopore volume, ρ is the pore wall density (ca. 2.2 $cm^3/g$ for siliceous materials), d is the XRD (100) interplanar spacing and c is the constant dependent on the pore geometry and is usually equal to 1.155 for hexagonally ordered pores.[160] Thermogravimetric analysis (TGA) was conducted using a TA instruments Q5000 with a heating rate of 5 °C/min under a nitrogen atmosphere. The APTES loading was calculated from the weight loss measured by TGA.

FT-IR spectra were recorded using the Nicolet FT-IR spectrometer and the samples were pressed into disks by mixing them in the ratio of 1:5 with KBr. The spectra were recorded in the range of 400-4000 $cm^{-1}$. Nuclear magnetic resonance (NMR) experiments were conducted on a 500 MHz Bruker Avance III spectrometer with 3.2 mm zirconia rotors. $^{13}C$-$^{1}H$ cross polarization magic angle spinning (CPMAS) experiments were conducted on the MCM-41 and aspirin-loaded MCM-41 using a 3.2 mm rotor and a MAS spinning speed of 10 kHz. $^{13}C$ single pulse (SP) MAS experiments were conducted with proton decoupling. Adamantane was the chemical shift reference material.

## 5.5 Theoretical Procedure

Molecular dynamics (MD) simulations were conducted in order to better understand the location of aspirin in the mesoporous silica pores. A two-fold approach was taken in the MD simulations. First, the cubic box of silica was used to perform a MD simulated annealing process to 10000 K in order to obtain liquid silica and then the system was quenched to 25 °C to obtain amorphous silica. Second, the MD simulation was conducted in the presence of aspirin and amorphous silica. For the first step, the CHIK potential parameters were used because this force field has been shown to behave well at high temperatures. For the second step i.e., for the amorphous silica and loaded aspirin simulations, the potential parameters developed by Lee and coworkers were used so that the hydrogen bonding and the interactions of the phenyl ring with the silica surface could be included.[161]

All of the simulations were performed using GROMACS molecular dynamic package. [162-166] Amorphous silica at room temperature (25 °C) and pressure (1 bar) was obtained from silica melt (at higher temperature). The interaction between the particles was calculated using CHIK potential. In order to obtain the silica melt, initially a cubic box containing 32000 O (oxygen) and 16000 Si (silicon) atoms were suitably placed in a simple cubic box. Each simulation box was equilibrated for at least 500 ps at 10,000 K in isothermal-isobaric (NPT) ensemble. The system was coupled to Parrinello-Rahman pressure bath to maintain 1 bar pressure.[164] The temperature of the system was regulated using a V-rescale algorithm as implemented in GROMACS.[162,163] Proper periodic boundary conditions were applied in order to simulate the system in the three dimensions. The leap-frog algorithm was used to integrate the equation of motion with 1 fs time step.

Cut-offs for short-range interactions and the real space part of the Coulomb interactions were set to 1.1 nm. The long-range electrostatic interactions were treated using particle mess ewald (PME) summation technique.[165,166] Simulations were also carried out at a temperature of 3600 K in order to validate the method. This was confirmed by comparing the simulated bulk density and pair distribution functions (O-O, Si-Si and Si-O) with available results in the literature at 3600 K.

A box of silica melt (at 10,000 K) was quenched to 25 °C and allowed to equilibrate for 50 ps in order to obtain the amorphous silica. The dimensions of the amorphous silica box, thus obtained, were approximately 8.98 nm X 8.98 nm X 8.98 nm. A cylindrical silica nanopore of diameter 3.2 nm was obtained by removing the atoms in xy plane along z axis. The total electro-neutrality of the whole system was ensured (assuming charges for Si as +2e, O as -1e, H as +0.5e) by adding H atoms to dangling oxygen atoms near the pore. The distance between oxygen and hydrogen atoms was kept at around 1 Å.[167,168] The unsaturated oxygen atom to add hydrogen to was chosen randomly. Aspirin parameters were taken from general AMBER force field (GAFF). In order to convert the AMBER type parameters to use in Gromacs package, we used the script developed by Sorin et al.. The initial configuration of the system of aspirin and mesoporous silica was generated with aspirin being in the center of the nanopore of the silica. [167-170 173] The Lennard-Jones (LJ) parameter for Si, O and H were taken from Lee *et al*.[161] The cross LJ parameters for silica and as well as the drug molecule were calculated using Lorentz Berthelot combination rules. Proper periodic boundary conditions were applied to the whole system and NVT ensemble for 400 ps. The Si, O and H atoms of the silica nanopore were frozen during the course of the NVT simulation.

## 5.6 Results

### 5.6.1 Synthesis and Characterization of MCM-41 Functionalized with APTES by Co-Condensation and Post-Synthesis Grafting

MCM-41 was synthesized, characterized and functionalized with APTES using co-condensation and post-synthesis grafting methods**.** Figure 29 shows the representative pXRD patterns for MCM-41 and for MCM-41 functionalized with APTES by co-condensation and post-synthesis grafting.

The powder X-ray diffraction patterns exhibit strong reflection peaks at (100), (110), (200) (2θ~2.2, 4.0 and 4.6, respectively) indicating a hexagonally ordered mesoporous structure. The diffraction patterns for the amine functionalized and aspirin loaded materials generally exhibit maxima of decreased intensity indicating that the long range ordering of the mesoporous structure decreased significantly after drug loading and with the incorporation of organic groups but the mesoporous structure was retained after the loading of the drug molecules. This is attributed to the pore filling by organic groups, as a result of which higher order diffraction peaks (110 amd 200) are observed with weaker intensities in functionalized and drug loaded samples. In the diffraction patterns, the intensity of the parent peak of MCM-41 (2θ ~ 2.2) has also decreased in the functionalized and drug loaded samples. The decreased intensity can again be attributed to the pore filling but can also be partially attributed to other factors such as incomplete hydrolysis of the siloxane bridges during synthesis of the mesoporous silica. It should be noted that the higher order peaks decrease more for samples prepared by post-synthesis modification relative to those prepared by co-condensation. This is due to the fact that

the APTES functional groups were added during the synthesis in the co-condensation method, so the structure is not affected as much as during post-synthesis modification. The pore diameters ($W_d$) calculated from the XRD patterns and [1] are provided in Table 5. As expected, the pore diameter decreases after functionalization, relatively more for the post-synthesis modified samples relative to the co-condensed samples. The pore diameters also decrease after aspirin loading.

The surface areas, pore volume and pore size distributions were analyzed using the nitrogen adsorption-desorption measurements for all MCM-41, APTES functionalized and aspirin loaded MCM-41 samples. A representative isotherm for MCM-41 with and without aspiring is shown in Figure 30. The surface areas and pore volumes are provided in Table 5.

Isotherms for all of the samples are provided as supplementary information. All of the samples exhibit capillary condensation process from $P/P_0$ from 0.1-0.3. The isotherms exhibit a type IV isotherm which is characteristic of the mesoporous materials having cylindrical mesopores.[159] The surface area and pore volume decrease both with amine and aspirin loading. The decrease in pore volume, pore diameter and surface area all indicate that the aspirin is adsorbed into the pores of MCM-41.

TGA was conducted on all of the samples. A representative TGA of MCM-PS-1 is shown in Figure 31. The thermogram of pure aspirin seen in inset shows two distinct

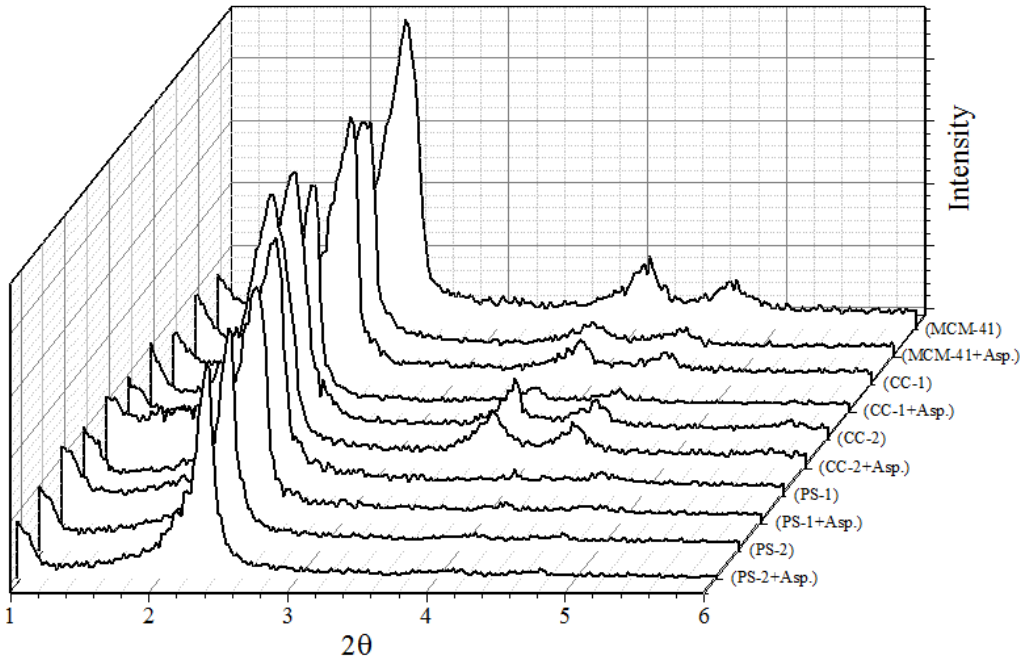


Figure 29. Powder X-ray diffraction patterns of both parent and functionalized mesoporous silica MCM-41 samples before and after drug loading.

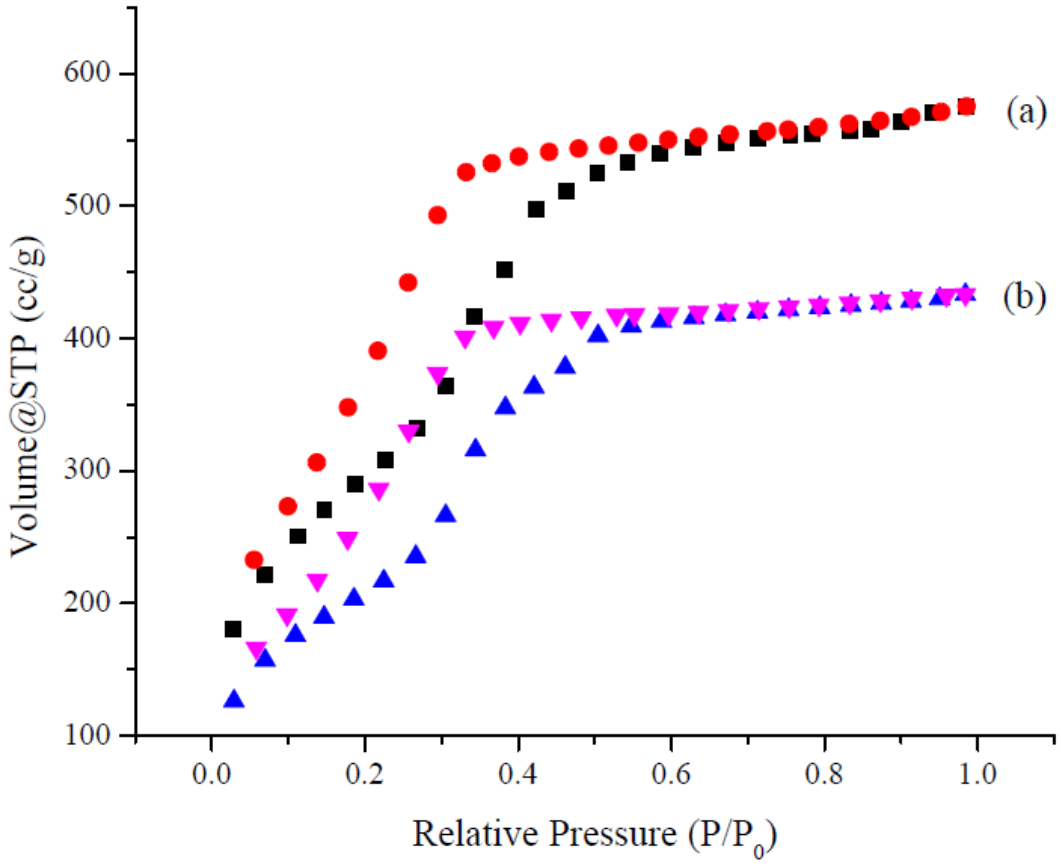


Figure 30. Nitrogen adsorption-desorption isotherms for (a) parent MCM-41 material and (b) MCM-41 with aspirin.

Table 5 Physicochemical properties of the MCM-41 before and after aspirin loading

| Sample | SA before (after), $m^2/g$[a] | $V_{pore}$ before (after), $cm^3/g$[a] | $W_d$ nm[a] | APTES Loading[b], mmol/g | Aspirin loading[b], mmol/g (mg/g) | Aspirin remaining after release[c], mg/g |
|---|---|---|---|---|---|---|
| MCM-41 | 1120(810) | 0.91 (0.67) | 3.50 (3.33) | -- | 0.55 (100) | 10 |
| MCM-CC-1 | 803 (661) | 0.68 (0.53) | 3.34 (3.17) | 0.45 | 0.67 (120) | 44 |
| MCM-CC-2 | 744 (520) | 0.41 (0.28) | 2.96 (2.66) | 0.54 | 0.94 (170) | 116 |
| MCM-PS-1 | 757 (618) | 0.48 (0.35) | 3.08 (2.84) | 0.54 | 0.67 (120) | 59 |
| MCM-PS-2 | 729 (518) | 0.46 (0.31) | 3.05 (2.75) | 0.60 | 0.72 (130) | 71 |

[a] before aspirin loading (after aspirin loading)

[b] calculated from the TGA data

[c] measured by UV/Vis

weight losses around 140 °C and 260 °C which may be attributed to the onset of melting followed by the decomposition of the drug. The first weight loss in the pure aspirin can be attributed to the elimination of acetic and salicyclic acids on heating the compound followed by the second weight loss which accounts for the decomposition of the solid residue. Similar trends could be seen in the drug-loaded samples in the different host systems with an extended range of temperature for the decomposition of the drug. In case of APTES functionalized samples, two weight changes are seen corresponding to the loss of physisorbed water followed by the decomposition of the functional group around 250 °C onwards. The TGA data was used to determine the amine group and aspirin loading for the MCM-41 samples from the measured weight loss. The complete results are listed in Table 5. The APTES loadings range from 0.45 to 0.60 mmol/g and the aspirin loadings range from 0.55 to 0.94 mmol/g. The highest APTES loading was observed for MCM-PS-2 and the highest aspirin loading was observed for MCM-CC-2.

### 5.6.2 NMR and FTIR Characterization of the MCM-41 and Aspirin Loaded MCM-41 Samples

$^{13}$C-CP-MAS experiments were conducted on all of the samples and on a physical mixture of aspirin and MCM-41. Representative $^{13}$C NMR spectra are shown in Figure 32. Characteristic resonances corresponding to aspirin were observed in the spectra. The peak at approximately 170 ppm was assigned to the carbonyls of the carboxylic acid and ester groups of the aspirin which are not resolved. The peaks in the region from 116 ppm – 150 ppm were assigned to the aromatic carbons of the phenyl ring in aspirin. The peak from the methyl group of aspirin was observed at approximately 19 ppm with two additional peaks coming from the propyl chain of the APTES moiety for the APTES

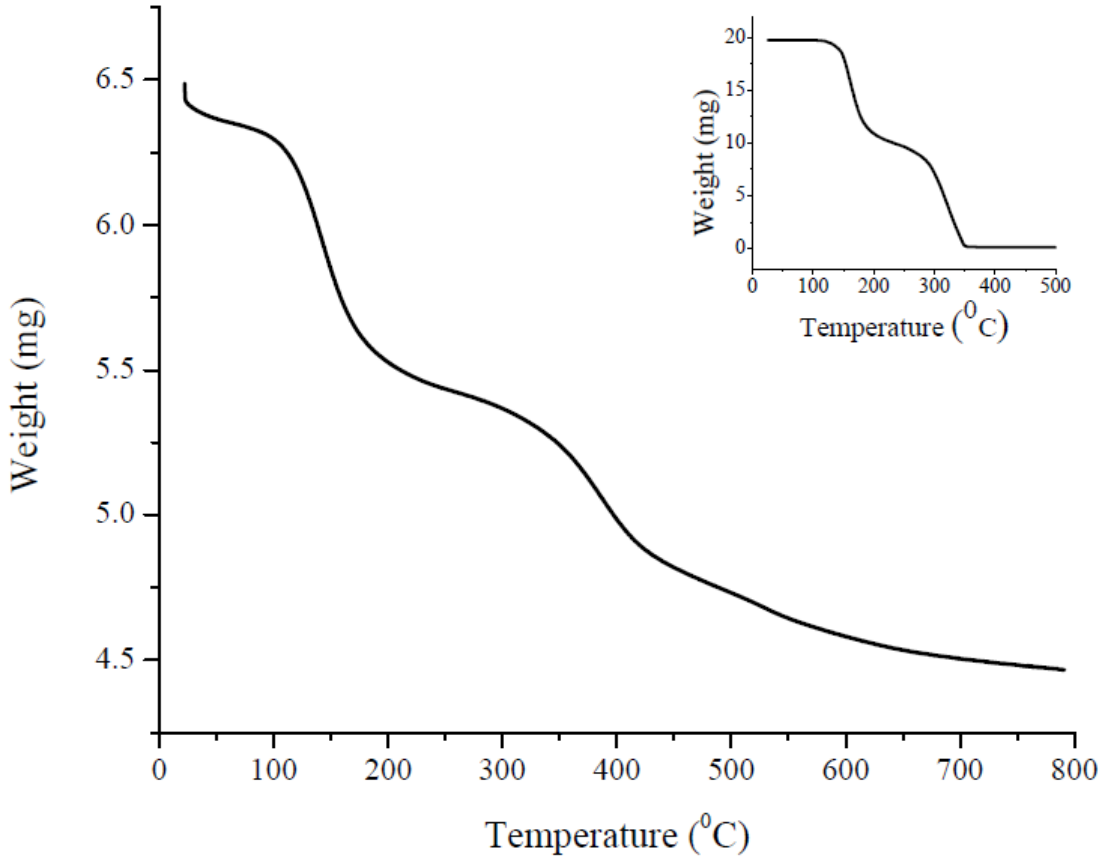


Figure 31. TGA plots of MCM-PS-1 loaded with aspirin and pure aspirin as an inset.

functionalized MCM-41 samples. The phenyl ring carbon peaks for all of the aspirin loaded samples (Fig. 32 b-e) are shifted for the MCM-41 samples relative to the physical mixture (Fig. 32a) indicating that the phenyl ring interacts with the MCM-41 surface. A similar shift has been observed for aspirin loaded in polymeric hosts and was attributed to an aspirin/host interaction.[171] In addition, the peak due to the phenyl group carbon bonded to the oxygen of the ester group (~150 ppm) is broadened and shifted for the APTES functionalized MCM-41 samples (Fig. 32 d,e) relative to the physical mixture.

In contrast, for the parent MCM-41, resonances due to the carbonyl carbons do not appear in the CPMAS NMR spectrum (Fig. 32b). In previous NMR studies of drug molecules, such as ibuprofen, incorporated into porous materials, this "missing" carbonyl peak has been attributed to the high mobility of the drug molecules in the pores which results in a decreased efficiency of the CP due to a decrease in the $^{13}C$-$^{1}H$ dipolar coupling. [172-177] To support this interpretation of the data, the single pulse MAS $^{13}C$ NMR spectrum with proton decoupling was obtained and is shown in Figure 32c. The carbonyl carbon signals due to both the carbonyl in the carboxylic acid and in the ester are observed in the NMR spectrum at ~ 170 ppm.The increased broadening in the $^{13}C$ NMR data for aspirin in the APTES-functionalized MCM-41 samples suggests that these samples undergo substantially less motion relative to aspirin in the parent MCM-41 sample, most likely due to the interaction between aspirin and the amine functional group.

The FTIR spectra of MCM-41 and aspirin are shown in Figure 33. In the case of parent MCM-41 sample (Figure 33a, black), there are several large peaks in the 1000-

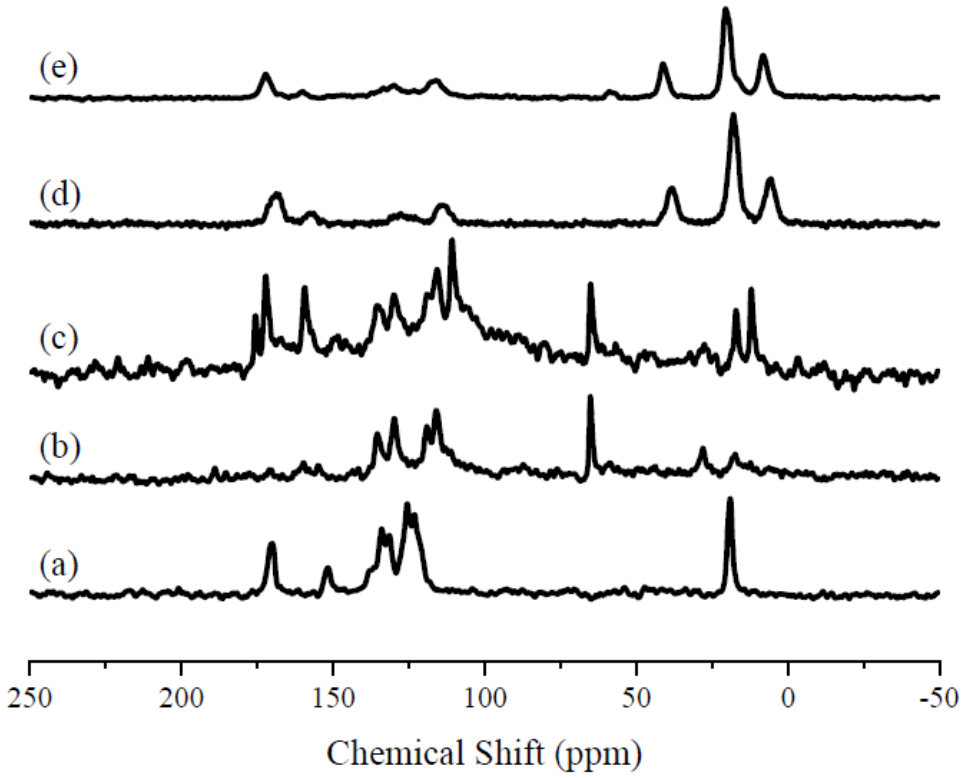


Figure 32. Solid State $^{13}C$ NMR of (a) physical mixture of mesoporous silica and aspirin (CP-MAS), (b) MCM-41 with aspirin (CP-MAS), (c) MCM-41 with aspirin (SP with decoupling), (d) MCM-CC-1 with aspirin (CP-MAS), and (e) MCM-PS-1 with aspirin (CP-MAS).

1250 $cm^{-1}$ range that are attributed to Si-O vibrations. [58,134-139,178-183] Another prominent peak is present at approximately 1636 $cm^{-1}$ and is due to water physisorbed on MCM-41. After aspirin loading (Figure 33a, red), a peak at ~1700 $cm^{-1}$ which is assigned to the carbonyl carbon. Relatively weaker peaks are also observed at 1486, 1425 and 1368 $cm^{-1}$ and these are attributed to aspirin phenyl group vibrations.

For the APTES functionalized MCM-41 sample, MCM-PS-1 (Figure 33b), a characteristic peak assigned to the bending mode of the amine groups is observed at ~ 1590 $cm^{-1}$ for both co-condensed and post-synthesis modification samples. Strong vibrational peaks are observed in the C–H stretching region around 2900 $cm^{-1}$. After loading the sample with aspirin, only small changes are observed in the FTIR spectra due to the overlapping vibrational bands of the APTES and aspirin. The carbonyl vibration at ~1700 $cm^{-1}$ is not observed and this is attributed to the strong interaction of the carbonyl carbon of the carboxylic acid with the amine groups. This lack of a carbonyl vibration at ~1700 $cm^{-1}$ has been observed in previous studies of aspirin on various mesoporous silica functionalized materials and has been attributed to the formation of a carboxylate species. The FTIR spectra for all of the APTES functionalized samples (included in supplementary information) have characteristics similar to Fig. 33b. The $^{13}C$ NMR spectra provide evidence that the carboxylic acid groups are present in the aspirin loaded samples even though they are not directly observed in the FTIR spectra.

### 5.6.3 Molecular Dynamics Simulation of Aspirin in MCM

41

The results of the molecular dynamics simulation of aspirin in mesoporous silica are shown in Figure 34. Figure 34a shows an aspirin molecule located in the center of the

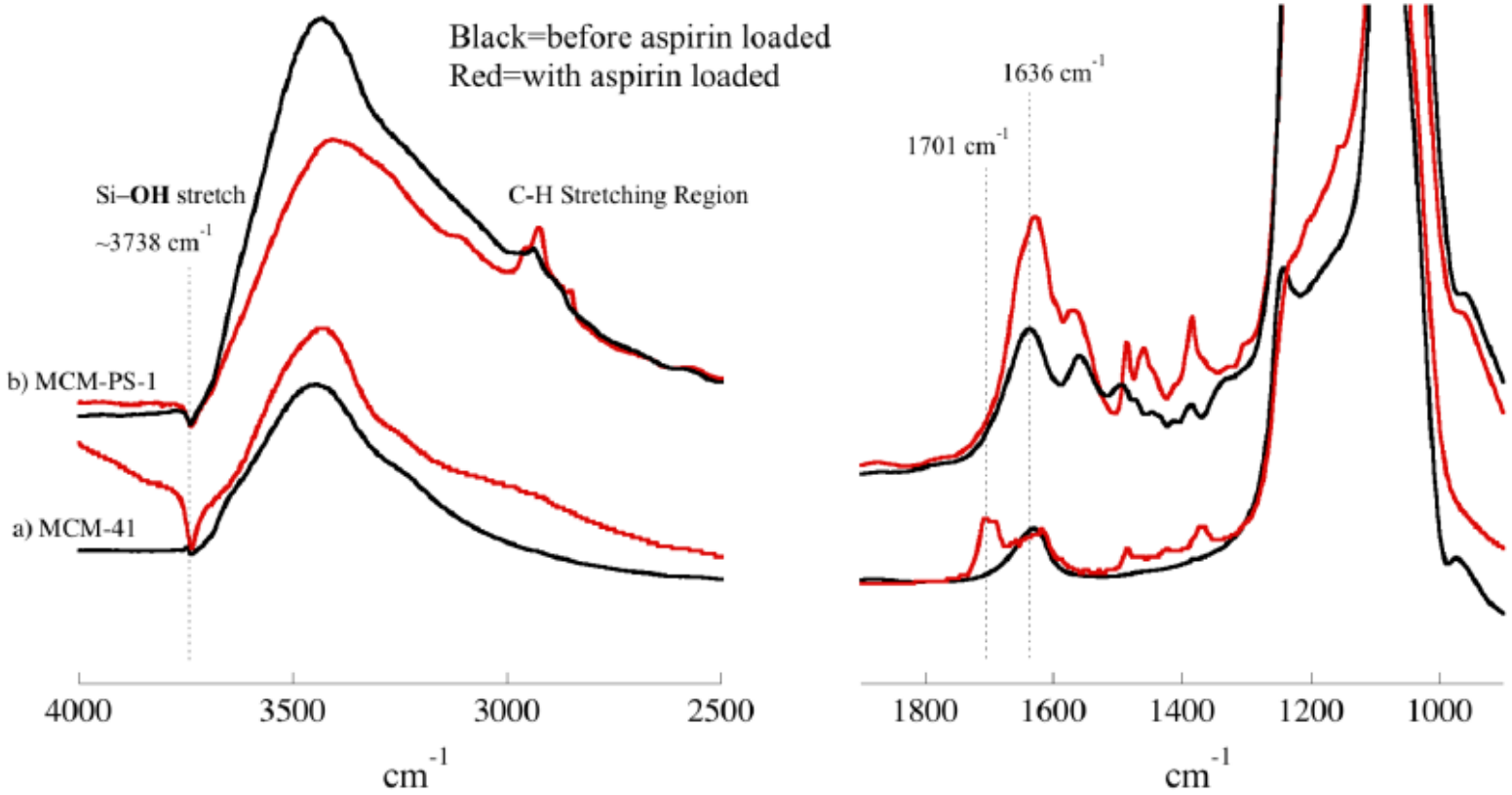


Figure 33. FTIR spectra of (a) MCM-41 and (b) MCM-PS-1 with (red) and without (black) aspirin loaded. The FTIR spectra before and after loading have been scaled to the strong framework Si−O vibration from ~1000−1200 cm−1 for display purposes.

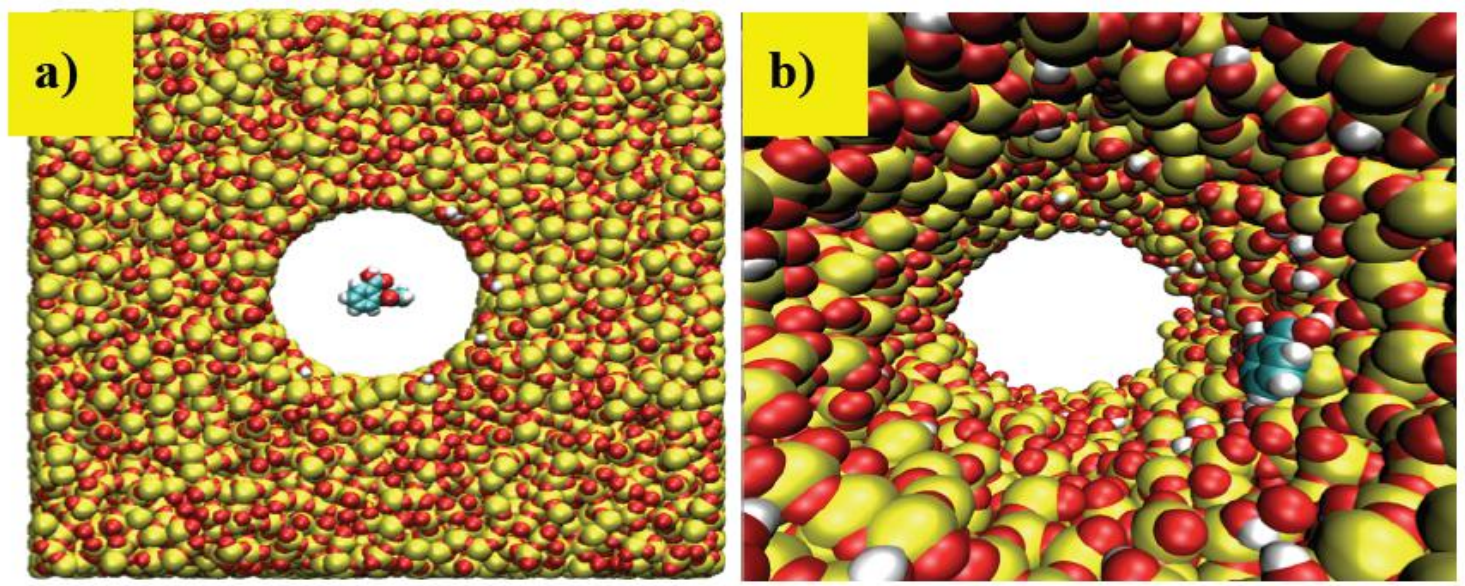


Figure 34. Results of the molecular dynamics simulation showing (a) the starting configuration with aspirin in the center of the 3 nm mesopore and (b) after 400 ps with the phenyl ring of aspirin orientated parallel to the pore wall.

Figure

3 nm pore at the beginning of the molecular dynamics simulation. After 400 ps, the aspirin is oriented along the pore wall, such that the phenyl group of the aspirin is parallel to the pore wall (Fig. 34b). The molecular dynamics results provide further support for the $^{13}C$ NMR results which show that the peaks assigned to the phenyl carbons are shifted relative to the pure aspirin suggesting that the phenyl group of aspirin interacts with the pore walls.

### 5.6.4 Aspirin Release from MCM-41

The aspirin release profiles for the MCM-41 and APTES modified MCM-41 are shown in Figure 35. Drug release from porous media can follow several different models. In some cases, the release process is governed by Fick's diffusion and can be described using a simplified Higuchi model, $Q=K_Ht^{0.5}$, where Q=the amount of drug release, $K_H$ is the Higuchi dissolution constant, and t is the time.[181] The Korsmeyer-Peppas model is similar except that a release exponent, n, is introduced into the model such that $Q=at^n$, where a is a constant. This equation can be modified to include a burst effect (b), such that

$$Q = at^n + b \qquad (19)$$

which is also called the Power Law.[181] In other cases, the drug release follows the first-order kinetic exponential decay model [179-186], with the equation represented as:

$$Q = Q_{max}(1 - \exp(-k_1 t)) \qquad (17)$$

where Q is the amount of drug released in time t, $Q_{max}$ is the maximum amount of drug released and $k_1$ is the first order release constant. For unmodified mesoporous silica materials such as MCM-41, the drug release is often governed by Fick's diffusion and

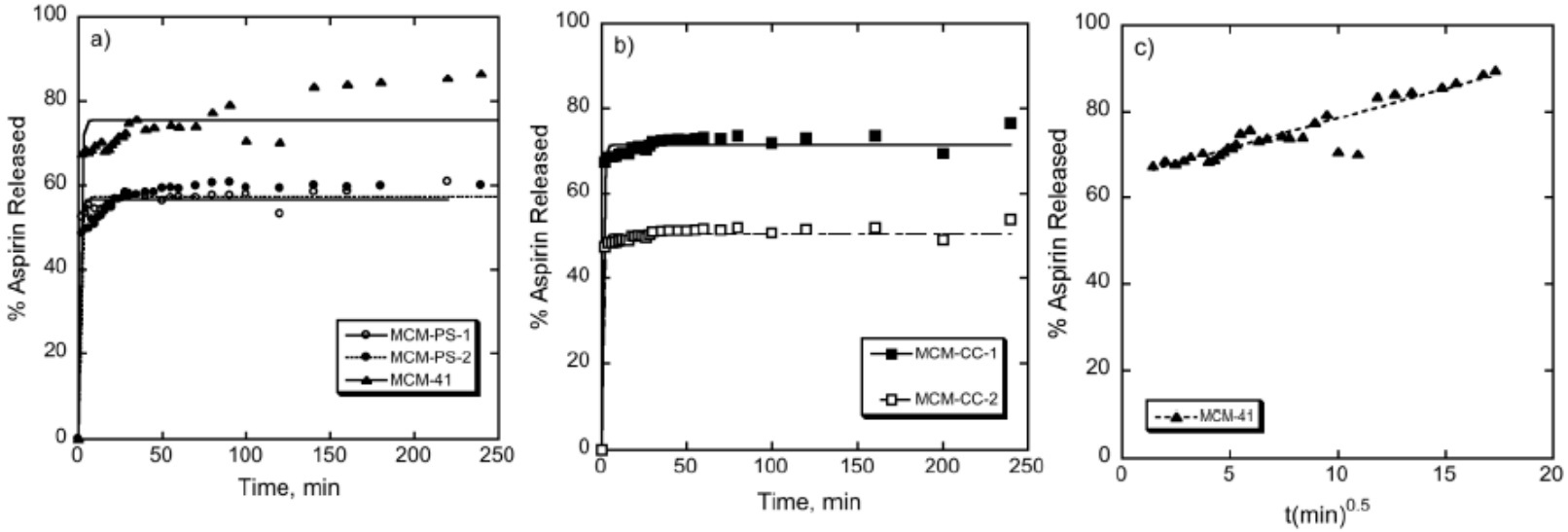


Figure 35. Aspirin release kinetics from MCM-CC-1 (filled square), MCM-CC-2 (open square), MCM-PS-1 (open circle), MCM-PS-2 (filled circle),and MCM-41 (filled triangle) are shown.

can be described using the Higuchi model.[152] The Korsmeyer-Peppas model has been used to describe the release of aspirin from bimodal mesoporous silica materials. For amine-modified MCM-41 and SBA-15, the drug release for ibuprofen and sodium alendronate has been described using the first order kinetic model described by [3].[143,146,157,158,160] Based on the previous work, the data from this study was analyzed using the first order kinetic model for the functionalized samples and the Power Law for the parent MCM-41.

The release profiles for aspirin from MCM-41 and MCM-41-CC and MCM-41-PS samples are plotted in Figure 35. Initially all of the release profiles were fitted using the first order kinetic model (equation [4]) and the fits to the data are indicated by the solid curves. The parameters $Q_{max}$ and $k_1$ obtained after fitting this release data with [4] are listed in Table 6. The parent MCM-41 release data does not fit this model very well as indicated by the $R^2$ value of 0.81 compared to $\geq$0.9 for all of the other samples. The parent MCM-41 data could be fit using the Power Law model with n=0.5 indicating Fickian diffusion and with a y-intercept which indicates a burst effect. The data and the fit (a=1.37 and b=64.5; $R^2$=0.85) are shown in Figure 35c. The diffusion of the drug molecules from the pores is largely dependent on the nature of the interaction of the drug molecule with the pore and the intrinsic mobility of the drug molecules inside the pores. The modification of the samples with functional groups causes steric hindrance as a result of which the diffusion deviates from the Fick's law.

From the release data shown in Table 6, it can be concluded that the total amine group loading and the method of loading (co-condensation or post-synthesis modification) both effect the release of the aspirin. The first order rate constant, $k_1$, is

approximately the same (~1.4 $min^{-1}$) for all of the samples, except for MCM-PS-2 in which the $k_1$ is smaller (0.78 $min^{-1}$). The reason for this may have to do with the higher loading of the amine group leading to increased pore-blocking, but it should also be noted that the $R^2$ value has also declined for MCM-41-PS-2 suggesting that the goodness of fit has also declined. For the samples prepared by co-condensation, the maximum release ($Q_{max}$) of the drug decreased from 71 to 50% most likely due to increased pore blocking due to the higher APTES content. In case of post-synthesis grafting, the $Q_{max}$ was not correlated with the loading of amine groups, which is attributed to the presence of amine groups at the pore entrances, which is similar for the post-synthesis samples, independent of the overall amine loading.

## 5.7 Discussion

A comparison of the loading and release for the different samples is provided in Figure 36. The loading of aspirin into ATPES functionalized MCM-41 was enhanced by 20-70% relative to the unfunctionalized MCM-41. The increase in aspirin loading in the amine functionalized MCM-41 materials is attributed to the favorable amine group and aspirin interaction. If the APTES loadings are further increased (data not shown), the aspirin loading declines due to pore blocking in both co-condensed and post-synthesis modification samples. The highest overall aspirin loading is achieved for the MCM-CC-2 sample. The literature suggests that the functional groups in MCM-41 samples prepared via co-condensation are more accessible and less likely to cause pore blocking relative to comparable samples prepared by post-synthesis modification. This accounts for the higher aspirin loading for the co-condensed sample with comparable APTES loading relative to the post-synthesis prepared sample. The data reported here is

consistent with this view in that the higher APTES loading observed for MCM-PS-2 does not result in increased aspirin loading under these conditions. So while the aspirin loadings are comparable due to the favorable interactions with the amine group, the distribution and amount of functional groups also impacts the aspirin loading and release properties.

The spectroscopic studies (FTIR and solid state NMR) indicate that the aspirin molecules are loaded intact into the MCM-41 samples. The spectroscopic data also indicate that aspirin is more weakly bound in MCM-41 relative to APTES functionalized MCM-41-CC and MCM-41-PS samples. In FTIR spectroscopy, the carbonyl band is observed for MCM-41 but is not observed for APTES functionalized MCM-41 samples suggesting a weak interaction with the parent and a stronger interaction between the APTES functionalized MCM-41 and the aspirin. The NMR data supports this interpretation as well in that the cross-polarization is not very efficient for aspirin on MCM-41 and this is attributed to motion of the aspirin in the pore which suggests weak interactions with the framework consistent with hydrogen bonding to the silanol groups of the mesoporous silica. The MCM-41-CC and MCM-41-PS $^{13}C$ NMR spectra are broadened relative to the physical mixture of MCM-41 and aspirin and also the carbonyl carbon peak is observed in the $^{13}C$-$^{1}H$ CP-MAS experiments. These observations indicate that the motion is restricted in the amine functionalized MCM-41 samples relative to the parent MCM-41. Previous NMR studies of ibuprofen on mesoporous materials exhibit similar behavior with respect to the $^{13}C$-$^{1}H$ cross polarization NMR. A shift of the $^{13}C$ phenyl group carbon resonances of aspirin is also observed in the $^{13}C$

Table 6. Fitted kinetic parameters for the release of aspirin from MCM-41 samples

| *Sample* | $Q_{max}$,% | $k_1(min^{-1})$ | $R^2$ |
|---|---|---|---|
| MCM-41 | 75±1 | 1.0±0.3 | 0.81 |
| MCM-CC-1 | 71.4±0.4 | 1.4±0.2 | 0.98 |
| MCM-CC-2 | 50.4±0.3 | 1.4±0.2 | 0.98 |
| MCM-PS-1 | 56.6±0.4 | 1.3±0.2 | 0.96 |
| MCM-PS-2 | 57.3±0.6 | 0.78±0.1 | 0.90 |

$Q_{max}$=maximum aspirin released (%); $k_1$=release rate constant

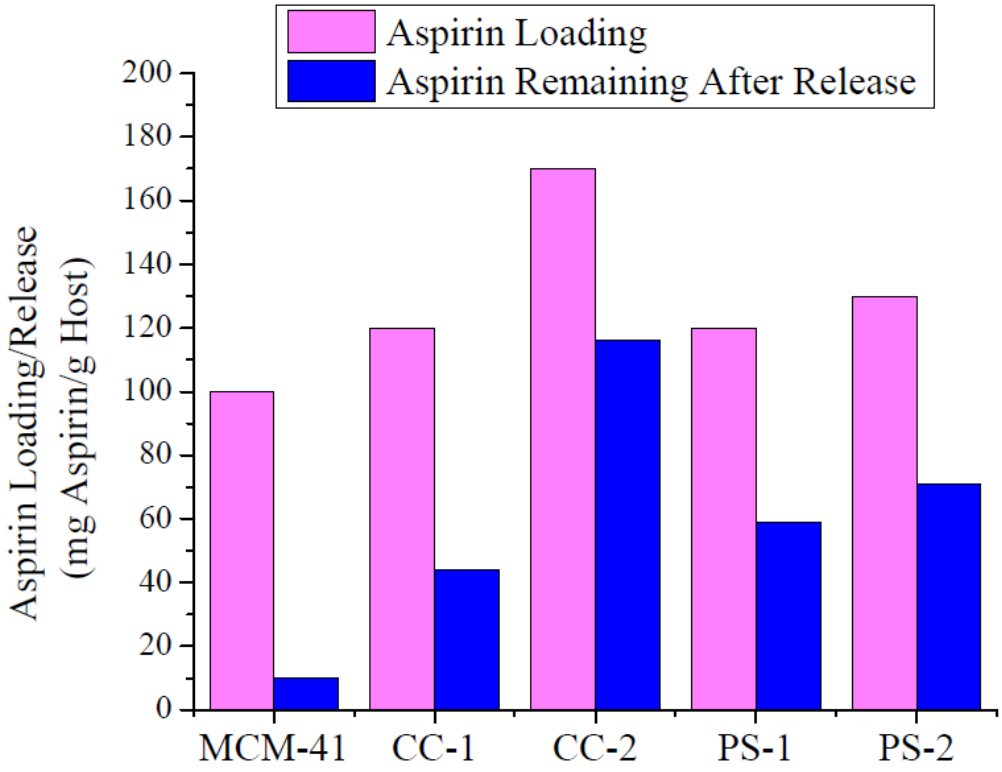


Figure 36. Summary of drug release

NMR suggesting that the phenyl group of aspirin interacts with the MCM-41 host. The MD simulations support the idea from the $^{13}C$ NMR data that the phenyl ring of aspirininteracts with the pore walls as shown in Figure 34b.

The release data can be understood by considering the molecular level details revealed in the FTIR and NMR experiments. The aspirin in the parent MCM-41 is weakly bound to silanol groups and the release follows Fick's diffusion. For the APTES functionalized MCM-41 samples, the aspirin undergoes a stronger interaction with the amine group and is released to a lesser extent relative to the parent MCM-41. For the co-condensed MCM-41 samples with aspirin loaded, a 71% release of the aspirin in 4 h. is observed whereas with higher loadings the release decreases to 50% after 4 h. In case of post-synthesis MCM-41 samples, the release reaches a plateau at approximately 57% aspirin release for both samples. A similar effect has been observed previously for sodium alendronate loaded on SBA-15 functionalized with APTES in two different ways. In that study, the $Q_{max}$ decreased for the samples functionalized by a catalytic method and the loading increased with increasing functionalization similar to our co-condensed sample. For the sample prepared by anhydrous post-synthesis modification, the drug loading and $Q_{max}$ remained about the same independent of APTES loading. This is consistent with the hypothesized location of amine functional groups at the pore mouth for the samples prepared by post-synthesis modification independent of loading. The functional group content and distribution of functional groups in the pores are both important factors governing the loading and release of aspirin from MCM-41.

## 5.8 Conclusions

This integrated experimental and computational study of aspirin loading and release from MCM-41 and amine functionalized MCM-41 provided insight into the molecular level interactions of aspirin with the mesoporous host. These insights were used to understand the loading and release data. The findings show that the distribution and loading of the functional groups are both important factors. In this study, the aspirin loading was maximized for APTES functionalized MCM-41 samples prepared by the co-condensation method because the functional groups are more evenly distributed in this method relative to the post-synthesis modification method. The aspirin release data for the parent MCM-41 was fitted using the Power Law, which is a modified form of the Korsmeyer-Peppas model for a diffusion based process that also takes into account a burst release. The release profiles for the APTES functionalized MCM-41 samples were fitted using a first order kinetic exponential decay model. The difference in release models was explained by the relatively weaker interaction of aspirin with the parent MCM-41 relative to the APTES functionalized samples. Solid state NMR and FTIR provided detailed molecular information about the aspirin binding to the mesoporous silica host that supported these conclusions. MD simulations indicated that the phenyl group of the aspirin was oriented parallel to the pore wall in agreement with the NMR data.

The results of this work were published in Journal of Physical Chemistry C, 2012, volume 116, pages 18358-18366 and authored by Datt, Maazawi and Larsen.

.

# CHAPTER 6

# LOADING AND RELEASE OF 5-FLUOROURACIL FROM HY ZEOLITES WITH VARYING $SIO_2/AL_2O_3$ RATIOS

## 6.1 Abstract

Zeolite Y with different silica to alumina ratios varying from 5 to 60 was used as a host for the chemotherapy drug, 5-fluorouracil. The 5-fluorouracil content in the zeolites was approximately 90-110 mg/g as determined by thermogravimetric analysis. Nitrogen adsorption-desorption measurements were used to measure the surface area and the pore volume of the zeolites before and after 5-fluorouracil loading. The decrease in surface areas and pore volumes after drug loading was attributed to the inclusion of 5-fluorouracil in the zeolite pores. FTIR spectroscopy provided evidence of molecular level interactions of the 5-fluorouracil with the zeolite. $^{27}$Al NMR indicated that the 5-fluorouracil interacted with the zeolite through the extraframework aluminum sites. Release profiles under physiological conditions were also conducted and indicated that the aluminum content was critical in determining the extent of release of 5-fluorouracil. HY-5 with the lowest $SiO_2/Al_2O_3$ released less than 5% of the loaded 5-fluorouracil while HY-30 and HY-60 released approximately 56 and 63% of the loaded 5-FU, respectively.

## 6.2 Introduction

The design of new materials for targeted drug delivery and drug release has been an area of great interest due to the potential to decrease drug toxicity and side effects, to avoid drug resistance and to increase drug efficacy.[64,184,185] The basic requirements for a drug delivery system are low toxicity, biodegradability and biocompatibility. Over the

past decades, materials such as polymeric systems and porous materials, such as mesoporous silica,[59,146,186] zeolites[187] and metal organic frameworks,[188] have shown potential for drug delivery.

Zeolites are microporous materials with a three-dimensional framework consisting of silicon, aluminum and oxygen. Due to the well-defined pore structure and pore topology, zeolites are widely used for adsorption, catalysis and separations.[89] The use of zeolites in drug delivery,[15,17,18,189,190] adsorption of pharmaceuticals[106] and imaging[10,13,99,101,102,191] has been explored in the literature. Specifically, the loading and release of drugs, such as sulfonamide antiobiotics,[14] ibuprofen, doxorubicin, and mitoxantrone[189] in zeolites have been investigated.

5-fluorouracil (5-FU) (Figure 37) is widely used in cancer treatment and has been particularly effective in the treatment of colorectal cancer.[192,193] 5-fluorouracil functions as an anti-cancer drug by inhibiting thymidylate synthase and the incorporation of its metabolites into RNA and DNA. However, the degradation of 5-FU before it reaches the cancerous areas, low 5-FU retention in tumors, drug resistance and toxicity are all problems that limit the clinical use of 5-FU in cancer treatment. Recently, controlled release applications of 5-FU with chitosan complexes,[194] clays,[195] zeolitic imidazolate frameworks (ZIFs)[196] and polymer nanoparticles[197] have been reported in the literature.

In this study, the loading and release of 5-fluorouracil (5-FU), a fluorinated pyrimidine (Figure 37), from zeolite HY with different silica to alumina ratios was investigated. 5-fluorouracil was used as a model drug for establishing the efficacy of zeolite hosts for small drug molecules. The molecular dimensions of the 5-fluorouracil

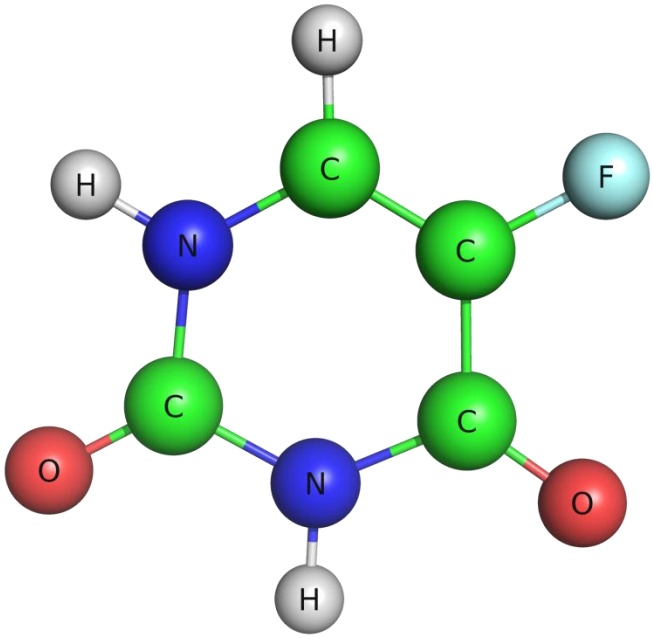


Figure 37. 5-FU

molecule are 4.9 Å X 5.3 Å. 5-fluorouracil is capable of entering the pores of zeolite Y and interacting with the supercage, which is ~12 Å in diameter. The present study focuses on the interactions between the zeolite HY pore walls and the 5-FU loaded inside and how these molecular interactions control the extent of release. This information can be used to tailor future zeolite-based drug delivery systems based on the zeolite physicochemical properties.

## 6.3 Experimental Section

### 6.3.1 Sample Preparation

Three zeolites with different $SiO_2/Al_2O_3$ ratios were purchased from Zeolyst International, CBV100 ($SiO_2/Al_2O_3$=5), CBV720 ($SiO_2/Al_2O_3$=30), and CBV760 ($SiO_2/Al_2O_3$=60). CBV720 and CBV760 were purchased with the charge-compensating cation $H^+$, whereas the CBV100 contained the charge-compensating cation $Na^+$. CBV100 was hydrogen exchanged in-house. Briefly, 1 g of commercial zeolite Y was mixed with 0.1 M ammonium nitrate and was stirred for 24 h at room temperature.[113] The sample was centrifuged and washed twice with deionized water. The zeolite powder was dried in an oven at 100 °C overnight and calcined under oxygen flow at 550 °C for 6 h to obtain the H-form of CBV-100 which will be referred to as HY-5. CBV720 and CBV760 were used as received. Throughout the manuscript, the three HY samples will be referred to as HY-5, HY-30 and HY-60 indicating the $SiO_2/Al_2O_3$ ratio. 5-Fluorouracil was used as obtained from Sigma Aldrich (99%).

### 6.3.2 5-Fluorouracil Loading and Release

Zeolite Y samples were mixed with 5-fluorouracil dissolved in water (12 mg/ml) and were stirred for 24-48 h at room temperature. Before the 5-fluorouracil loading, the zeolite powders were pretreated at 120 °C for 8 h to activate the zeolite and to remove the physisorbed water from the zeolites. After stirring, the solutions were centrifuged for 20 minutes at 14000 rpm and thoroughly washed with water twice in order to remove excess 5-fluorouracil. The amount of 5-fluorouracil loaded was calculated using thermogravimetric analysis (TGA) data.

To determine the release profile, 5-fluorouracil-loaded zeolite was mixed (1 mg/ml) with simulated body fluid at pH 7.4 and 37 °C in an Erhlenmeyer flask. The simulated body fluid was prepared with sodium monobasic phosphate and sodium dibasic phosphate. The ~100 mL samples were stirred at ca. 100 rpm and 2 ml aliquots were removed at regular intervals. To maintain a constant volume, 2 ml aliquots of simulated body fluid were added at each step. The aliquots were centrifuged in order to ensure no solid was in suspension and the supernatants were analyzed for 5-fluorouracil with UV – Vis spectroscopy (Varian Cary 100 Scan) at λ= 266 nm. The amount of released 5-fluorouracil as calculated using the following equation[198]:

$$C_{tcorr} = C_t + \frac{v}{V}\sum_0^{t-1} C_t \qquad (16)$$

where $C_{tcorr}$ is the corrected concentration at time t (corrected to account for previously taken samples). $C_t$ is the apparent concentration at time t, v is the volume of the sample taken, and V is the total volume of the solution. Experiments were conducted in duplicate and the values were averaged.

## 6.4 Characterization

The zeolites were characterized using several different techniques. The zeolite crystallinity was evaluated using powder X-ray diffraction (pXRD) (Siemens D5000 X-ray diffractometer with Cu Kα and a nickel filter). A broad-range pattern (2θ = 5 to 55 with a 0.04 step size, 1 s/step) was collected for the parent HY zeolites and the 5-FU-loaded HY zeolites.

Nitrogen adsorptions of the parent and 5-FU-loaded zeolite HY samples were measured using a Nova 1200 Nitrogen Adsorption Instrument (Quantachrome). Approximately 100 mg of zeolite powder was dried at 120 °C under vacuum overnight. A 7-point BET isotherm was then recorded and the specific surface area was calculated for the samples ($S_{tot}$). A 50-point adsorption/desorption isotherm was measured and used for calculation of total pore volume from the amount of adsorbed nitrogen at 0.97 $P/P_o$.

Thermogravimetric analysis (TGA) was conducted using the TA Q5000 TGA instrument with a heating rate of 5 °C/min under nitrogen flow. Samples were heated from room temperature to 800 °C and the weight change was recorded. The TGA data was used to calculate the 5-FU loading.

FT-IR spectra were recorded using the Nicolet FT-IR spectrometer. The samples were pressed into disks by mixing them with KBr in a 1:5 ratio. The spectra were recorded in the range of 400-4000 $cm^{-1}$.

Nuclear magnetic resonance (NMR) experiments were conducted on a 500 MHz Bruker Avance III spectrometer with 3.2 mm zirconia rotors. $^{27}Al$ Magic Angle Spinning (MAS) NMR experiments were conducted on both 5-fluorouracil loaded and parent HY

zeolite samples. $AlCl_3$ was used as a chemical shift reference for $^{27}Al$ NMR. The spinning speed for all $^{27}Al$ experiments was 30 kHz.

## 6.5 Results and Discussion

### 6.5.1 Physicochemical Characterization of Zeolite HY Before and After 5-FU Loading

The zeolite HY samples were characterized using several different techniques before and after 5-fluorouracil loading. The representative powder X-ray diffraction (pXRD) patterns of zeolite HY-30 before and after 5-FU loading are shown in Figure 38. Characteristic pXRD peaks corresponding to zeolite Y were observed. The pXRD patterns after 5-FU loading were similar to the parent zeolite powder X-ray diffraction patterns indicating that the zeolite HY framework structure did not change. However, there was an overall reduction in intensity of the peaks after loading indicating a slight decrease in the cqrystallinity after 5-FU adsorption. The pXRD patterns of the other zeolites are similar and are provided as supporting information.

Figure 39 shows the thermograms for the pure drug molecule and the 5-FU loaded zeolite, HY-30. From the thermograms, it can be seen that the drug molecule decomposes below 300 °C and in the range of 280 °C to 675 °C for the 5-FU loaded zeolite sample. The extended decomposition range for the 5-FU loaded zeolite is due to the interactions of drug molecule with the zeolite framework. The 5-FU loadings for all 3 HY samples calculated from TGA data are listed in table 7. The 5-FU loadings range from 90-110 mg 5-FU/g HY with the 5-FU loading increasing with increasing aluminum content (decreasing silica to alumina ratio).

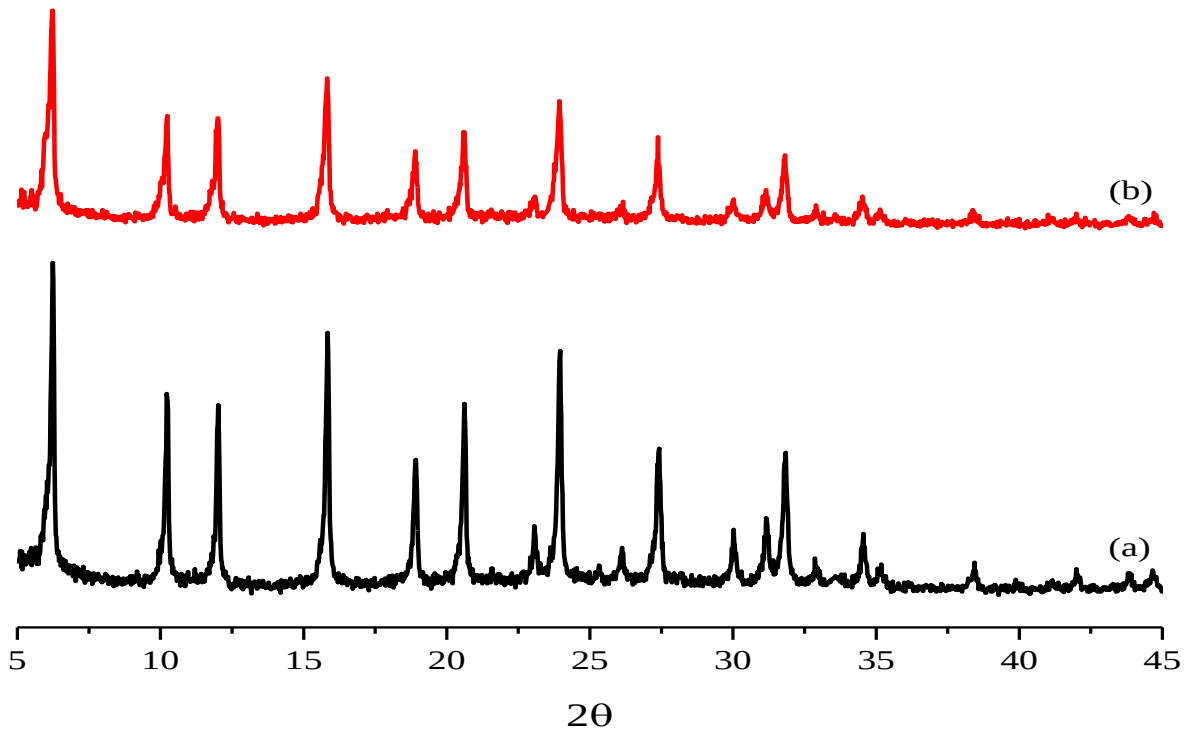


Figure 38. Powder X-ray diffraction patterns of a) parent zeolite Y (HY-30) and b) zeolite Y (HY-30) with 5-fluorouracil.

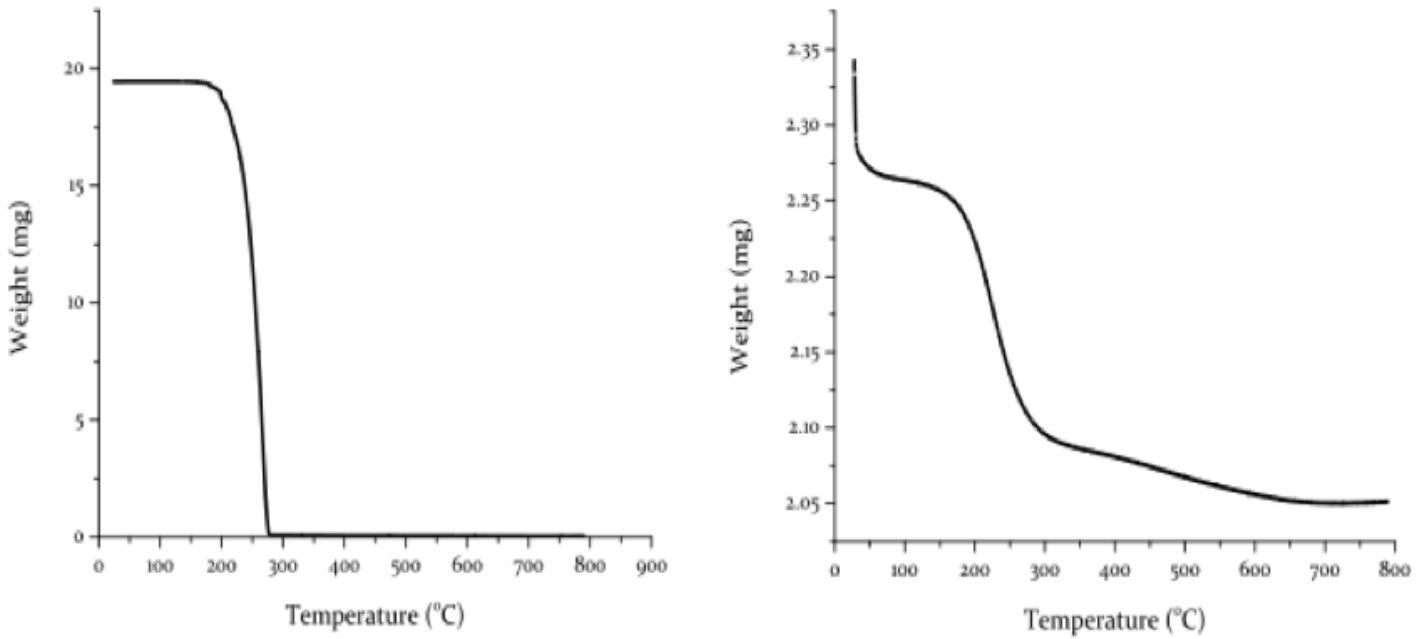


Figure 39. TGA of pure 5-fluorouracil (left) and zeolite HY-30 with 5-fluorouracil (right).

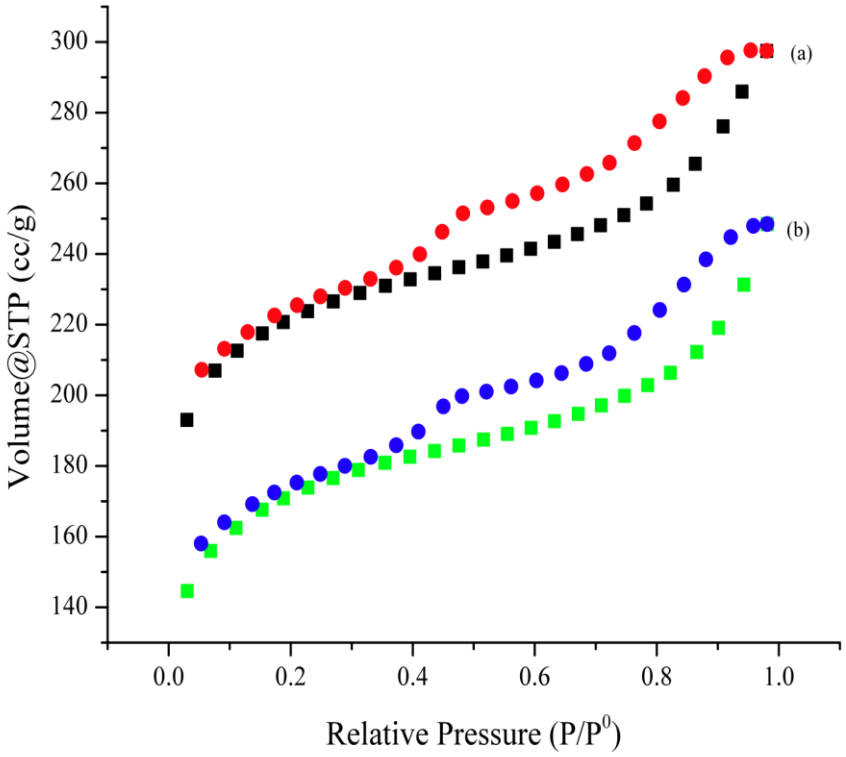


Figure 40. Nitrogen adsorption-desorption isotherms for (a) HY-30 and (b) HY-30 with 5-FU. ● represents the desorption branch and ■ represents the adsorption branch of the nitrogen isotherms.

Table 7. Physicochemical properties of parent and drug loaded zeolites

| Sample | Surface Area ($m^2/g$)[a] | Pore Volume ($cm^3/g$)[a] | 5-FU Loading (mg/g)[b] | 5-FU Remaining after Release (mg/g)[c] |
|---|---|---|---|---|
| HY-5 | 594 (357) | 0.26 (0.14) | 110 | 105 |
| HY-30 | 688 (455) | 0.30 (0.19) | 105 | 45 |
| HY-60 | 711 (514) | 0.31 (0.20) | 90 | 32 |

[a] before (after) 5-FU loading; [b] calculated from TGA data; [c] calculated from UV/Vis data

Nitrogen adsorption-desorption isotherms were used to calculate the surface area and total pore volume before and after adsorption of the drug molecule. A representative isotherm for HY-30 with and without 5-FU loaded is shown in Figure 40 and the complete results are provided in Table 7. A decrease in the surface areas (~30-40%) and the pore volumes (~35-45%) after drug loading in the HY zeolite samples was observed confirming that the 5-FU is loaded in the pores of the zeolites.

### 6.5.2 FTIR and NMR Results

FTIR experiments were conducted to probe the molecular level interactions of 5-FU with zeolite HY. The FTIR spectra of the expanded region from 1200-1900 $cm^{-1}$ of the 5-FU and 5-FU loaded HY zeolites are shown in Figure 41. Vibrational peaks and their assignments for the FTIR spectra of 5-FU (Figure 37) and 5-FU loaded in HY zeolites are listed in Table 8. The parent drug molecule, 5-FU, has characteristic vibrations at 1771, 1723, 1665 and 1245 $cm^{-1}$. The peaks at 1771 and 1723 $cm^{-1}$ are assigned to the carbonyl vibrational bands for the C2 and C4 carbonyl groups, respectively, through a comparison with the FTIR spectrum of 5-FU in an Ar-matrix. The peak at 1665 $cm^{-1}$ is assigned to the C5=C6 stretching mode of 5-FU and the peak at 1245 $cm^{-1}$ is assigned to the C-F bending vibration according to the literature. The HY samples loaded with 5-FU have characteristic vibrations at 1756, 1717, 1690 and 1247 $cm^{-1}$. These peak are assigned to the C2 and C4 carbonyl groups, the C5=C6 stretching vibration and the C-F bending vibration, respectively. The carbonyl bands are red-shifted slightly relative to the parent 5-FU, but the largest shift is observed for the C5=C6 stretching mode which is blue-shifted from 1665 to 1690 $cm^{-1}$ for 5-FU compared to HY/5-FU. There is also a peak at ~1633 $cm^{-1}$ in the FTIR spectra of the 5-FU loaded HY

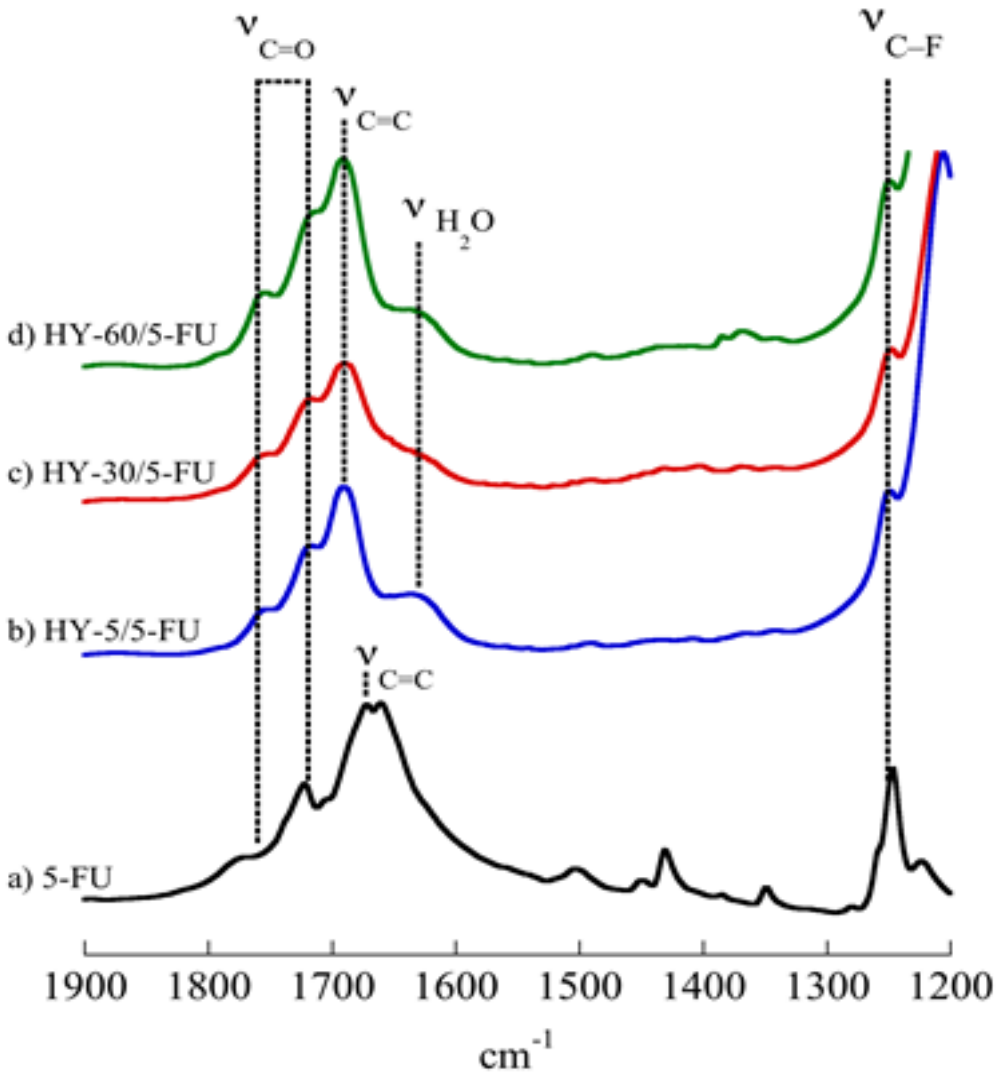


Figure 41. FTIR spectra of a) 5-FU, b) HY-5/5-FU, c) HY-30/5-FU and d) HY60/5-FU.

Table 8 Experimental FTIR frequencies for selected vibrational bands of 5-FU and zeolite HY/5-FU

| | $\nu_{C=O}$ (C2) | $\nu_{C=O}$ (C4) | $\nu_{C=C}$(C5-C6) | $\nu_{CF}$ | **Reference** |
|---|---|---|---|---|---|
| 5-FU | 1771 | 1723 | 1665 | 1247 | This study |
| HY-5/5-FU | 1756 | 1717 | 1690 | 1247 | This study |
| HY-30/5-FU | 1756 | 1717 | 1690 | 1247 | This study |
| HY-60 /5-FU | 1756 | 1717 | 1690 | 1247 | This study |
| 5-FU (Ar matrix) | 1780 | 1746 | 1686 | 1247 | [199] |
| 5-FU montmorillonite | 1723 | 1681 | 1618 | 1255 | [200] |

zeolites and this is attributed to the bending mode of water adsorbed on the zeolite. This peak is also observed on the parent zeolites without any 5-FU present.

The FTIR results confirm that the 5-FU is loaded intact into the zeolite HY hosts. The shift of the C5=C6 vibrational frequency from ~1665 $cm^{-1}$ for pure FU to 1690 $cm^{-1}$ for 5-FU loaded into HY is consistent with an interaction of the ring (specifically near the fluorine group) with the zeolite framework. In previous work of 5-FU intercalated in the clay material, montmorillonite, it was suggested based on FTIR results that the 5-FU was coordinated to Lewis acid centers through water molecules.

In order to elucidate the role of aluminum in the loading and release of 5-FU in zeolite Y, $^{27}Al$ MAS NMR spectra were acquired for HY parent and 5-FU loaded samples (Figure 42). The aluminum NMR shows characteristic peaks at approximately 0 ppm and 60 ppm corresponding to octahedral (extraframework aluminum or EFAL) and tetrahedral aluminum coordination, respectively. An interesting observation from the aluminum NMR spectra was the decrease in the intensity of the octahedral peak after 5-FU loading relative to the parent zeolite sample. This decrease in intensity of the octahedrally coordinated aluminum can be attributed to an increase in the linewidth or to a decrease in the amount of octahedral aluminum. An increase in linewidth could be caused by an increase in the quadrupole coupling constant for the octahedral aluminum or to a change in the coordination of the octahedral aluminum leading to a decrease in intensity. Either scenario points to the involvement of the 5-FU with the octahedral aluminum sites causing a change in coordination and/or quadrupole coupling. It should also be noted that the HY-5 sample has a much higher concentration of aluminum relative to the HY-30 and HY-60.

### 6.5.3 5-Fluorouracil Release from HY Zeolites

The release profiles for 5-fluorouracil from zeolites, HY-5, HY-30 and HY-60 are shown in Figure 43. The release data for HY-30 and HY-60 are comparable with release maxima around 60%. HY-5, the zeolite with the highest aluminum content, deviated significantly from this pattern. The amount of the drug released from HY-5 is almost negligible (~ 5%) over the period of 300 minutes.

Release profiles for drug molecules adsorbed in porous media can be analyzed using empirical[181] or mechanistic models.[201-203] In this work, the release profiles were fitted to the first order kinetic model for drug release from a porous matrix.[157] The first order exponential decay model equation can be represented as:

$$Q = Q_{max}(1 - \exp(-k_1 t)) \qquad (17)$$

where Q is the amount of drug released in time t, $Q_{max}$ is the maximum amount of drug released and $k_1$ is the first order release constant. The parameters $Q_{max}$ and $k_1$ were obtained after fitting the release data shown in Figure 43. The fitted parameters are tabulated in Table 9, which shows $Q_{max}$ for HY-30 and HY-60 as 56% and 63% respectively. The first order release rate constant for the HY-30 and HY-60 samples were 1.4 and 1.5 $min^{-1}$ respectively. The drug release parameters for HY-5 were not calculated because the very small 5-FU release resulted in a very poor fit to the data.

Based on the release data, it appears that the aluminum content in the zeolite has an important role in determining the drug release profiles. The zeolite HY-5 with the highest aluminum content has the capacity to interact with the fluorouracil species both

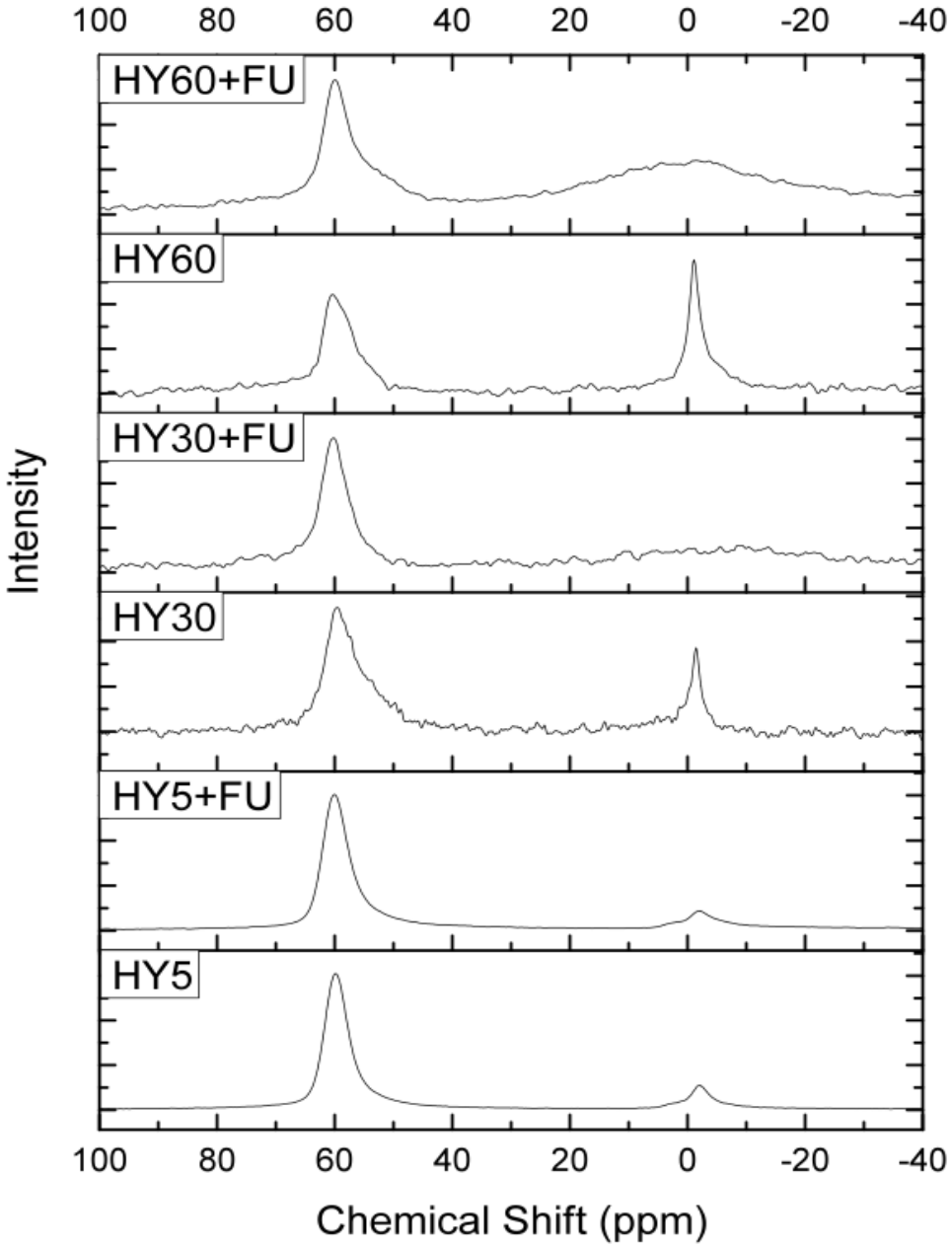


Figure 42. $^{27}$Al MAS spectra of parent and 5-FU loaded HY zeolites

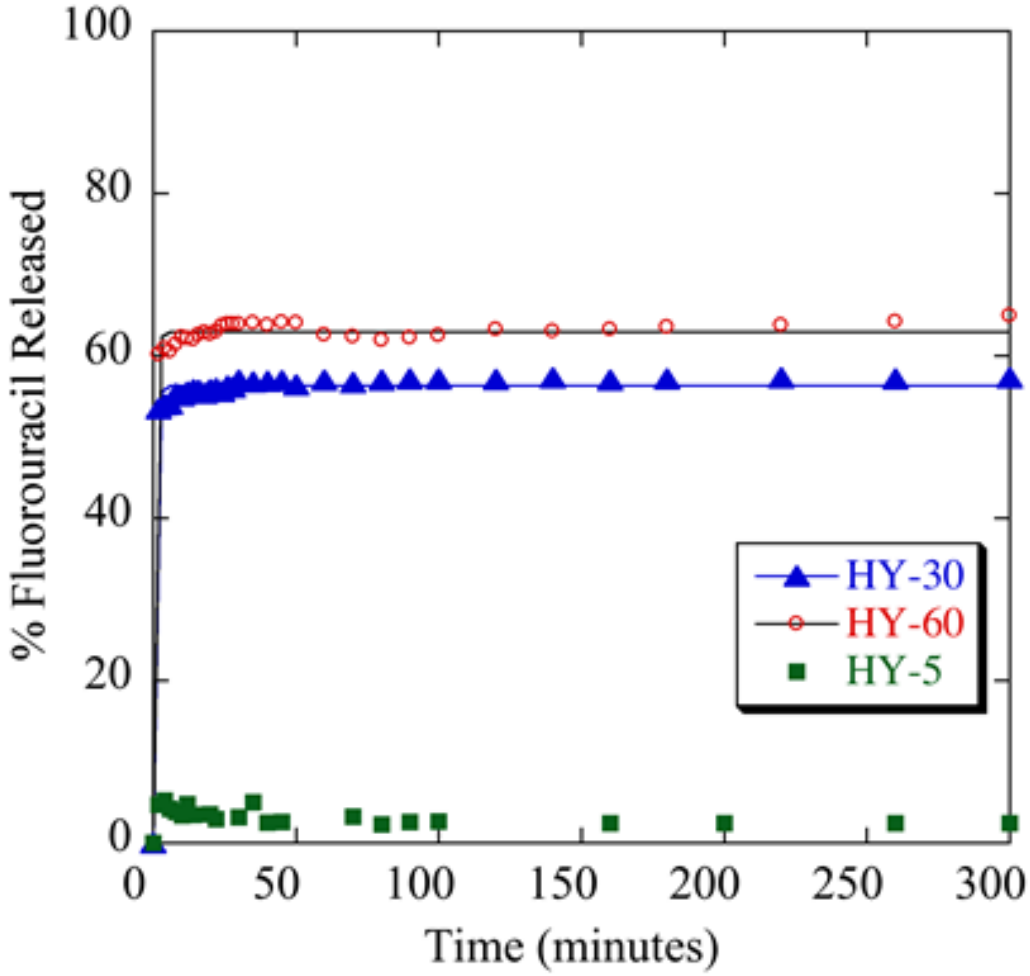


Figure 43. 5-FU release kinetics from HY-5, HY-30 and HY-60. The least squares fits to the function Q=Qmax[1-exp(-k1*t)] are shown by the solid lines for HY-30 and HY-60. The release was measured in phosphate buffer solution at pH=7.4.

Table 9. Fitted Kinetic Release Parameters for 5-fluorouracil Release from HY

| **Sample** | **$Q_{max}$,%** | **$k_1$($min^{-1}$)** |
|---|---|---|
| HY-5 | -- | -- |
| HY-30 | 56.3±0.2 | 1.4±0.1 |
| HY-60 | 63.0±0.2 | 1.5±0.2 |

$Q_{max}$=maximum 5-fluorouracil released (%); $k_1$=release rate constant

by hydrogen bonding as well as coordination complexation between the 5-FU molecules and the zeolite aluminum atoms. A similar trend was observed in case of the zeolite-ibuprofen interactions with different silica to alumina ratios. In the ibuprofen/zeolite HY study it was proposed that the ibuprofen bound to the EFAL was more strongly bound and thus less readily released.

### 6.5.4 Discussion

The aluminum content in the zeolite has a critical role in determining the drug loading and release profiles. The 5-FU loadings increased with increasing aluminum content for 90 to 110 mg/g for HY-60, HY-30 and HY-5, respectively. Different release behaviors indicated that aluminum has an integral role in governing the interactions between HY zeolites and 5-FU. A graph of the relationship between the loading and release of 5-FU and the $SiO_2/Al_2O_3$ ratio of HY is shown in Figure 44. The zeolite HY-5 with the highest aluminum content may interact with the 5-fluorouracil species by hydrogen bonding of the carbonyl oxygen atoms with the zeolite hydroxyl groups as well through coordination between the drug molecules and the aluminum atoms, specifically the EFAL. A similar trend was observed in case of the ibuprofen interactions with zeolites with different silica to alumina ratios. Vallet-Regi and coworkers proposed that the ibuprofen was strongly coordinated to the EFAL resulting in less drug release. A similar behavior was observed for 5-FU on HY zeolites in that the HY with the greatest aluminum content has a decreased release of 5-FU. In addition, the literature precedent shows that the 5-FU forms complexes with aluminum such as the binding of the 5-fluorouracil drug molecule with the –C=O and –N-H moieties with the $Al^{3+}$ species.[204] As a consequence, the zeolite HY-5 with having the highest aluminum content may result in

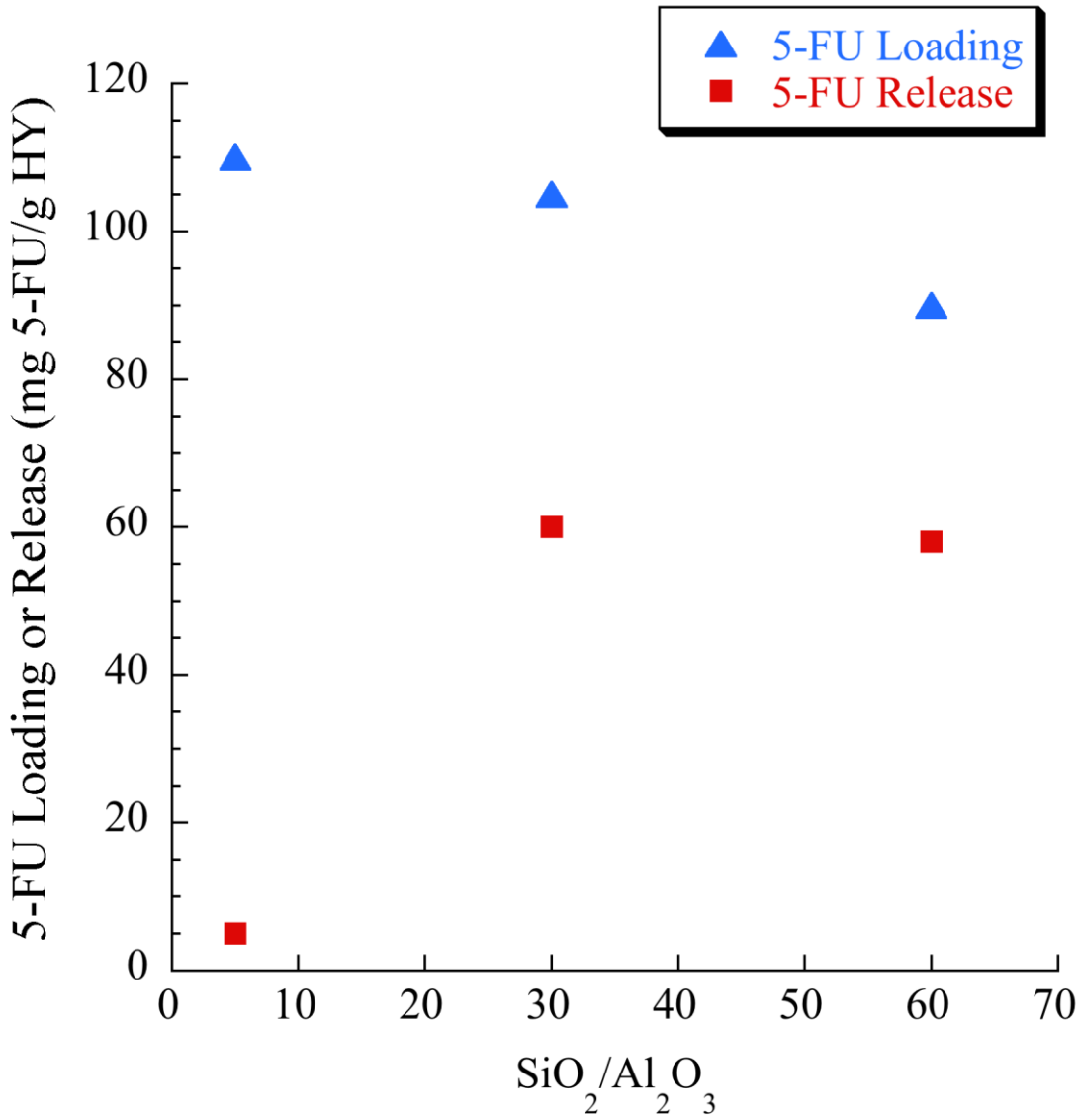


Figure 44. The loading and release of 5-FU from HY as a function of silica to alumina ratio.

the formation of such strongly bound complexes in the drug loaded zeolite, thus limiting the release of the drug from the parent zeolite. The $^{27}$Al MAS NMR also indicates that aluminum has a major role in the interaction of 5-FU with the zeolite.

## 6.6 Conclusions

The loading and release of 5-FU from zeolite HY with different silica to alumina ratios varying from 5 to 60 was investigated. Thermogravimetric analysis and nitrogen adsorption data indicated that the 5-FU was located within the zeolite HY pores. The FTIR spectra of the 5-fluorouracil-loaded zeolites showed characteristic 5-FU vibrations and $^{27}$Al NMR indicated that the 5-fluorouracil interacts with the zeolite through the extraframework aluminum sites. Release profiles under physiological conditions were also conducted and indicated that the aluminum content was critical in determining the release of 5-fluorouracil. HY-5 with the lowest $SiO_2/Al_2O_3$ did not release the 5-fluorouracil while HY-30 and HY-60 released approximately 56 and 63% of the 5-FU, respectively. This is attributed to the formation of a complex between 5-FU and EFAl in the zeolite as supported by the $^{27}$Al NMR data.

The results of this work were published in Microporous and Mesoporous Materials, 2012, In Press and authored by Datt, Burns, Dhuna and Larsen.

# CHAPTER 7

# LOADING AND RELEASE OF SMALL DRUG MOLECULES USING AMINE FUNCTIONALIZED MESOPOROUS SILICA SBA-15

## 7.1 Abstract

A comprehensive study of aspirin loading and release from SBA-15 and amine functionalized SBA-15 was conducted. Both the parent and functionalized SBA-15 samples were thoroughly characterized before and after aspirin loading by nitrogen adsorption isotherms and thermal gravimetric analysis to determine the structure and physicochemical properties such as surface area, pore volume and functional group loading. Molecular level details about the aspirin-SBA-15 interactions were revealed through FTIR and $^{13}C$ solid-state NMR experiments. For the aminopropyl-functionalized SBA-15, the carboxylic acid group of aspirin associates with the amine group of the functionalized SBA-15. In all of the samples, an interaction between the aspirin phenyl group and the mesoporous silica host was hypothesized based on shifts in the phenyl group $^{13}C$ NMR resonances. The release data indicated that loading of the amine functional groups in SBA-15 influenced the release properties of aspirin.

## 7.2 Introduction

There has been a tremendous growth in the design of novel drug delivery systems because of their therapeutic and healthcare principles. The potential of a drug delivery system lies in its effectiveness to decrease drug toxicity and side effects, to avoid drug resistance and to increase drug efficacy.[181] The basic requirements for a drug delivery system are low toxicity, biodegradability and biocompatibility. Over the past decades, materials such as polymeric systems[64] and porous materials, such as mesoporous silica[205-

[207], zeolites[187,208] and metal organic frameworks[209], have shown potential for drug delivery. A good drug delivery system should possess a sustained/controlled release profile, and should be easily tunable for a wide variety of therapeutics.

Mesoporous silica has attracted a lot of attention in the past decades due to their widespread applications. They have been extensively studied in the field of adsorption, catalysis, biosensors and drug delivery.[129] The biomedical applications in particular have been one of the most extensively investigated areas for mesoporous silica recently. Large pore sized materials namely SBA-15 are potential candidates for such biological applications due to their large range of pore dimensions in comparison to other mesoporous silica. SBA-15 mesoporous silica has pore sizes ranging between 20 and 300 Å, and use non ionic block copolymers as structure directing agents in highly acidic media.[210,211] In addition to their large pore sizes, SBA-15 materials possess higher hydrothermal stability due to their thicker pore walls than MCM-41 materials. Due to its attractive properties such as high surface area, tunable pore volumes and pore diameters, several attempts have been made to harness the potential of SBA-15 as a drug delivery system.[147,212] However, there remains a need to design suitable functionalized mesoporous systems in order to introduce stronger host-guest interactions beyond weak hydrogen bonding interactions.

In the study reported here, aspirin was chosen as a model drug due to its small molecular size, good pharmacological activity, and short biological half-life. In addition, it has a carboxyl group that can interact with surface silanol groups or amino groups on the pore walls and may be useful for the controlled drug release. The loading and release of aspirin from SBA-15 modified with aminopropyltriethoxysilane (APTES) functional

groups was investigated in order to develop a fundamental understanding of the interactions of aspirin with the mesoporous silica host and how these impact loading and release properties. Post synthesis grafting method was used as a means of functionalization and the effect of the functionalization agent was also studied. The SBA-15 materials were extensively characterized by thermal gravimetric analysis (TGA), and nitrogen adsorption for surface area and pore volume measurements. The aspirin loaded materials were characterized spectroscopically using FTIR and solid state NMR before and after aspirin loading.

## 7.3 Experimental Procedures

### 7.3.1 Materials Required and Synthesis

Materials: 3-Aminopropyltriethoxysilane (APTES, Sigma Aldrich), tetraethoxysilane (TEOS, Sigma Aldrich), hexadecyltrimethyl-ammonium bromide (CTAB, Sigma Aldrich), Pluronic Acid (P123, Sigma Aldrich), and acetylsalicylic acid (Aspirin, Alfa Aesar) were used as received.

Synthesis of SBA-15: SBA-15 was synthesized using Pluronic P123 (Polyethylene glycol –block- polypropylene glycol –block- polyethylene glycol) as the surfactant and CTAB as a co-surfactant. The molar ratio of the mixture was 1 CTAB: 0.314 P123: 54.7: 27.4 TEOS: 208 EtOH: 842 $H_2O$. P123 was dissolved in the HCl and in a separate beaker CTAB was dissolved in water until both solutions were transparent. The solutions were then mixed together and ethanol was added while the reaction was heated to 313 K. The TEOS was added dropwise and the reaction was stirred for 30 minutes, then the mixture was transferred to a Teflon autoclave and aged in an oven at 353 k for 3 days.[213,214]

Post Synthesis Grafting of SBA-15: The post-synthesis grafting procedure involved refluxing 1 g of calcined SBA-15 and APTES (4 mmol or 8 mmol) in toluene at 120 °C for 6 h. The resulting sample was filtered, washed with 1:1 mixture of dichloromethane and diethylether and dried in an oven at 100 °C. These samples will be referred to as SBA-15-PS-1 and SBA-15-PS-2 for the lower and higher APTES loaded samples, respectively.

### 7.3.2 Drug Loading and Release

The mesoporous silica SBA-15 was loaded with the aspirin by mixing the aspirin in ether until it dissolved, then adding the SBA-15 with magnetic stirring for 12-24 h at 25 °C. The solution was filtered and dried at 25 °C overnight. For release profiles, 100 mg of the loaded SBA-15 was placed in a phosphate buffer solution with pH = 7.4 at 37.4 °C. The contents were stirred at approximately 100 rpm and 2 ml aliquots were removed at regular intervals of time. The aliquots were centrifuged in order to ensure no solid was in suspension and transparent supernatants were analyzed for aspirin with UV –Vis spectroscopy (Varian Cary 100 Scan) at λ= 296 nm. The amount of released aspirin was calculated using the following equation:

$$C_{tcorr} = C_t + \frac{v}{V}\sum_0^{t-1} C_t \qquad (16)$$

where $C_{tcorr}$ is the corrected concentration at time t (corrected to account for changes in volume), $C_t$ is the apparent concentration at time t, v is the volume of the sample taken, and V is the total volume of the solution. Experiments were conducted in duplicate and the values were averaged.

### 7.3.3 Characterization

The textural properties of the SBA-15 materials were characterized using a variety of techniques. The SBA-15 structure was verified using powder X-ray diffraction (pXRD) (Siemens D5000 X-ray diffractometer with Cu Kα and a nickel filter). A small-range pattern (2θ = 1 to 5 with a 0.02 step size, 1 s/step) was collected. Surface areas and pore volumes of the SBA-15 materials were measured using nitrogen adsorption and a Nova 1200 Nitrogen Adsorption Instrument (Quantachrome). Approximately 100 mg of SBA-15 was dried overnight at 120 °C in vacuum. A 7-point BET isotherm and a 50-point adsorption/desorption isotherm were measured and used for calculation of the surface area and total pore volume. The total pore volume ($V_{tot}$) was calculated by measuring the amount of adsorbed nitrogen at 0.97 $P/P_0$. The pore diameter was calculated using the BJH method by looking at the adsorption branch of the nitrogen isotherm.

Thermogravimetric analysis (TGA) was conducted using a TA instruments Q5000 with a heating rate of 5 °C/min under a nitrogen atmosphere. The APTES loading was calculated from the weight loss measured by TGA.

FT-IR spectra were recorded using the Nicolet FT-IR spectrometer and the samples were pressed into disks by mixing them in the ratio of 1:5 with KBr. The spectra were recorded in the range of 400-4000 $cm^{-1}$. Nuclear magnetic resonance (NMR) experiments were conducted on a 500 MHz Bruker Avance III spectrometer with 3.2 mm zirconia rotors. $^{13}C$-$^{1}H$ cross polarization magic angle spinning (CPMAS) experiments were conducted on the SBA-15 and aspirin-loaded SBA-15 using a 3.2 mm rotor and a MAS spinning speed of 10 kHz

## 7.4 Results and Discussion

### 7.4.1 Physiochemical Properties

The powder diffraction patterns for the parent and the drug loaded samples showed no diffraction peaks, due to the amorphous nature of the material. For the porosity of the SBA-15 materials, nitrogen adsorption-desorption isotherm measurements were conducted. Figure 45 displays the typical nitrogen adsorption-desorption plots for the parent SBA-15 and the drug loaded samples. All the samples show the typical type IV hysteresis curve, accouting for a well ordered pore structure. In the nitrogen adsorption-desorption isotherms, the capillary condensation step occurs in the range of 0.4-0.8 partial pressures, which is expected for SBA-15 type materials.[211] The surface area and pore volume for the parent SBA-15 was found out to be 790 $m^2/g$ and 1.33 $g/cm^3$ respectively.

### 7.4.2 Aspirin Loaded SBA-15

The porosity of aspirin loaded SBA-15 materials were characterized using nitrogen adsorption-desorption isotherms. The surface areas and pore volumes of the aspirin loaded SBA-15 materials decreased after functionalization with APTES molecules and aspirin loading. The decrease in the surface area for aspirin loaded materials was about 50% and 65% for SBA-15-PS-1and SBA-15-PS-2 samples relative to the parent material. The pore volumes and the pore diameters for the drug loaded samples are shown in Table 10.

Thermogravimetric analysis measurements were performed in order to obtain the amounts of the amine groups grafted on the surface as well as the aspirin loading. The

Table 10. Physicochemical properties of SBA-15 materials before and after drug loading

| Samples | Surface Area ($m^2/g$) | Pore Volume ($cm^3/g$) | APTES Loading, mmol/g | Drug Loading, mg/g[a] | Drug Remaining after release, (mg/g)[b] |
|---|---|---|---|---|---|
| SBA-15 | 790 | 1.33 | -- | -- | -- |
| SBA-PS1 | 570 | 0.96 | 0.80 | -- | -- |
| SBA-PS2 | 471 | 0.52 | 1.05 | -- | -- |
| SBA+Asp. | 598 | 1.03 | -- | 80 | 11 |
| SBA-PS1+Asp. | 396 | 0.76 | 0.80 | 125 | 75 |
| SBA-PS2+Asp. | 284 | 0.44 | 1.05 | 140 | 114 |

[a] Determined from TGA

[b] Determined from UV-Vis.

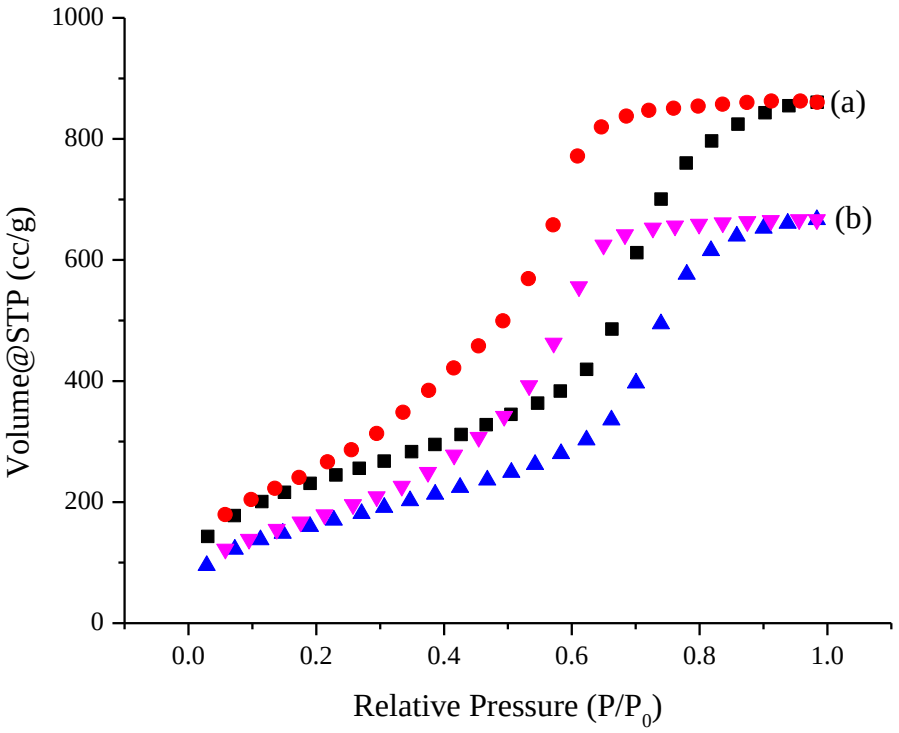


Figure 45. Nitrogen isotherm plots for (a) parent SBA-15, and (b) SBA-15 with aspirin

thermograms for amine functionalized samples show a cumulative weight loss starting from 220 °C accounting for the loss of the grafted APTES molecules. For the aspirin loaded materials, the cumulative weight was recorded and was then subtracted from its parent functionalized sample to obtain the amount of aspirin encapsulated. For the parent SBA-15 loaded sample, the thermogram shows two distinct weight changes around 140 °C and 260 °C which may be attributed to the onset of melting followed by the decomposition of the drug. Table 10 shows the complete analysis of the obtained amounts of the APTES as well as the aspirin loaded samples. Representative thermogram showing the weight loss due to SBA-15-PS2 sample is shown in Figure 46 with the inset of pure aspirin.

$^{13}C$ CP-MAS solid state NMR studies were conducted in order to provide molecular insights of aspirin in the parent and functionalized samples. $^{13}C$ NMR spectra are shown in Figure 47. Characteristic resonances corresponding to aspirin were observed at approximately 170 ppm which was attributed to the carbonyls of the carboxylic acid and ester groups of the aspirin. The peaks in the region from 116 ppm – 150 ppm were assigned to the aromatic carbons of the phenyl ring in aspirin. The peak from the methyl group of aspirin was observed at approximately 19 ppm with two additional peaks coming from the propyl chain of the APTES moiety for the APTES functionalized SBA-15 samples. The phenyl ring carbon peaks for all of the aspirin loaded samples are shifted for the SBA-15 samples relative to the physical mixture indicating that the phenyl ring interacts with the SBA-15 surface. The results obtained for the solid state NMR were similar to that of aspirin loaded in MCM-41 mesoporous silica matrices (Figure 32).

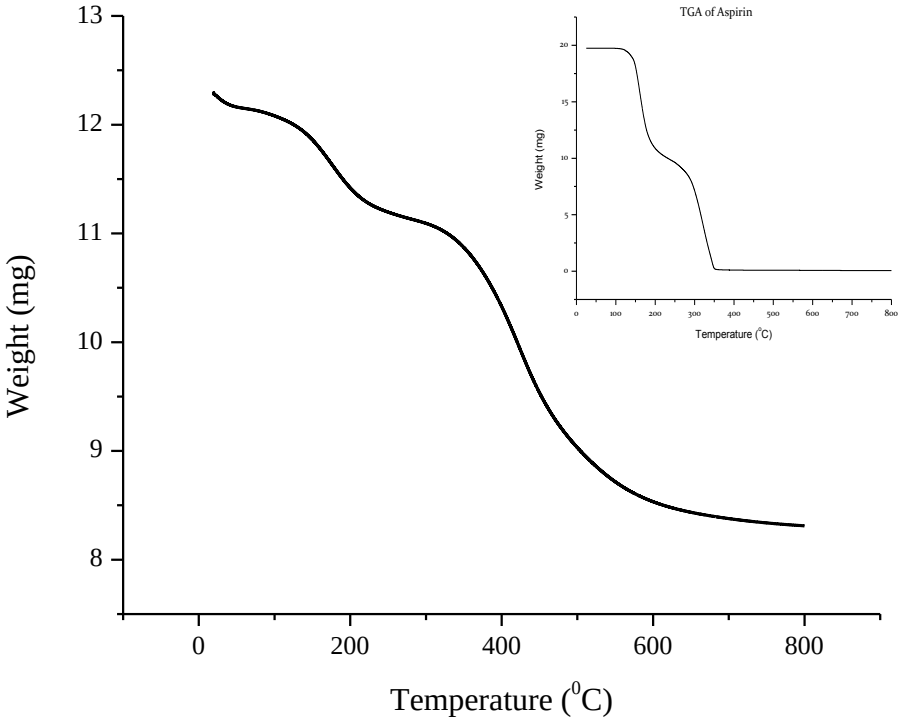


Figure 46. Thermograms of (inset) pure aspirin and SBA-15-PS1 with aspirin

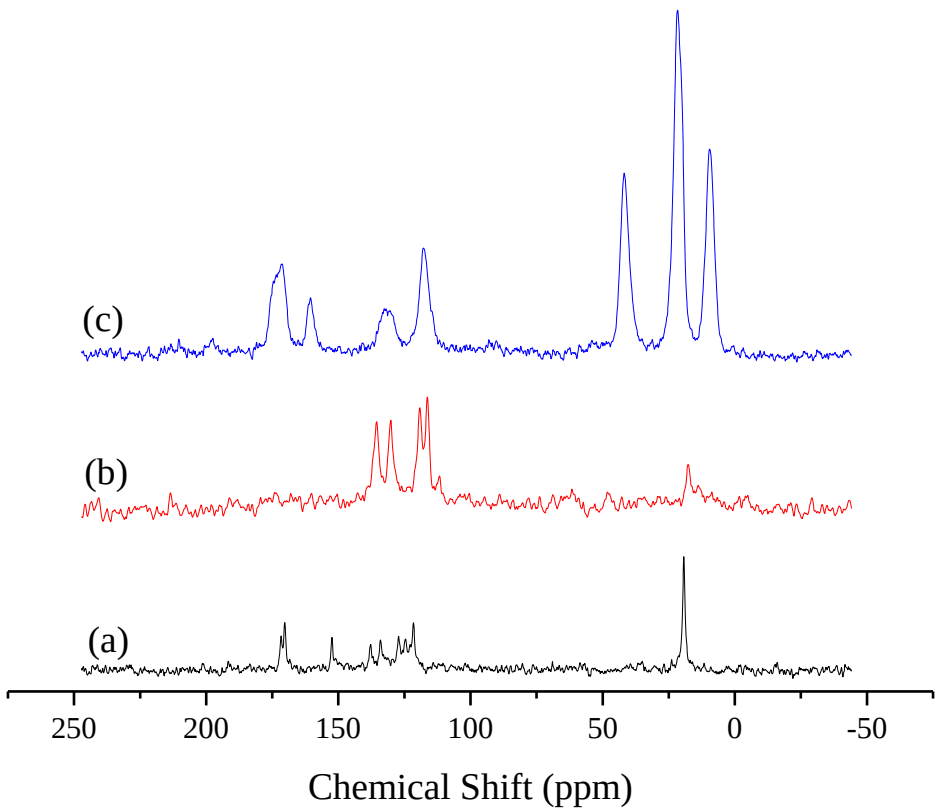


Figure 47. $^{13}C$ CP-MAS Solid State NMR spectra for (a) physical mixture of SBA-15 and aspirin, (b) SBA-15 with aspirin, and (c) SBA-15-PS2 with aspirin

The FTIR spectra of SBA-15 and aspirin are shown in Figure 48. In the case of parent SBA-15 sample, the peak in the 1000-1250 $cm^{-1}$ range that are attributed to Si-O vibrations. Another prominent peak is present at approximately 1636 $cm^{-1}$ and is due to water physisorbed on SBA-15. After aspirin loading, the peak at ~1700 $cm^{-1}$ which is assigned to the carbonyl carbon is shifted to 1657 $cm^{-1}$ which accounts for the presence of hydrogen bonding in the system. Stronger peaks are also observed at 1486, 1448 and 1368 $cm^{-1}$ and these are attributed to aspirin phenyl group vibrations.

For the APTES functionalized SBA-15 sample, the shoulder observed at ~ 1590 $cm^{-1}$ is assigned for the bending mode vibrations of $NH_2$ group in APTES. Strong vibrational peaks are observed in the C–H stretching region around 2900 $cm^{-1}$. After loading the sample with aspirin, only small changes are observed in the FTIR spectra due to the overlapping vibrational bands of the APTES and aspirin.

The aspirin release profiles for the SBA-15 and APTES modified SBA-15 are shown in Figure 49. Drug release from porous media can follow several different models. In some cases, the release process is governed by Fick's diffusion and can be described using a simplified Higuchi model, $Q=K_H t^{0.5}$, where Q=the amount of drug release, $K_H$ is the Higuchi dissolution constant, and t is the time. In other cases, the drug release follows the first-order kinetic exponential decay model with the equation represented as:

$$Q = Q_{max}(1 - \exp(-k_1 t)) \qquad (17)$$

where Q is the amount of drug released in time t, $Q_{max}$ is the maximum amount of drug released and $k_1$ is the first order release constant. For unmodified mesoporous silica

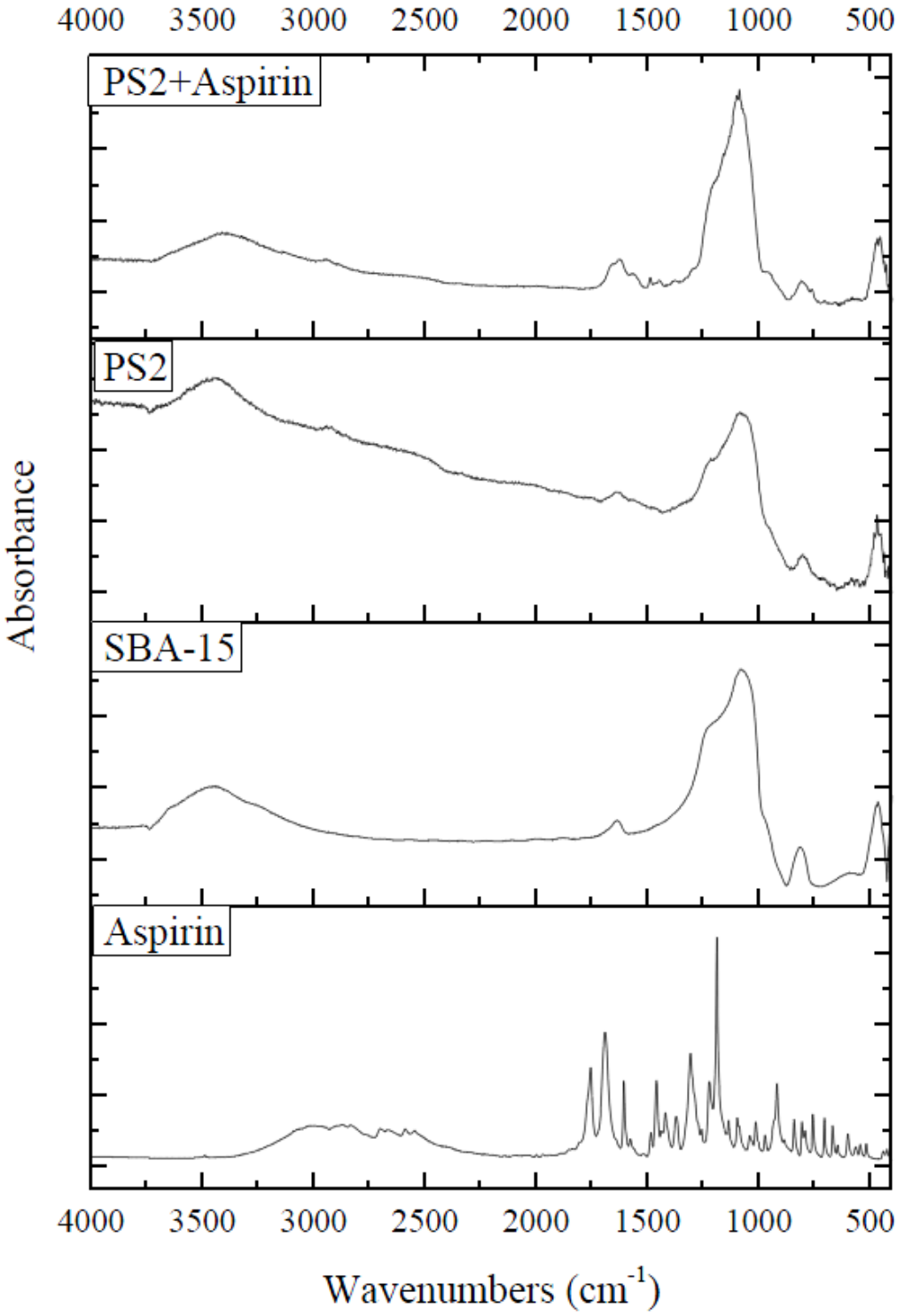


Figure 48. FT-IR spectra showing the vibrations from SBA-15 materials with aspirin

Table 11 Kinetic parameters for the aspirin release from the parent and functionalized SBA-15 samples.

| Sample | $Q_{max}$ | k | $R^2$ |
|---|---|---|---|
| SBA-15+Aspirin | 67 | 0.04 | 0.54 |
| SBA-15-PS1-Aspirin | 50 | 0.03 | 0.98 |
| SBA-15-PS2-Aspirin | 26 | 0.33 | 0.97 |

materials such as SBA-15, the drug release is often governed by Fick's diffusion and can be described using the Higuchi model. Figure 50 shows the Higuchi model plots for both parent and functionalized SBA-15 with aspirin. The Korsmeyer-Peppas model has been used to describe the release of aspirin from bimodal mesoporous silica materials. The release profiles for aspirin from SBA-15 and SBA-15-PS samples are plotted in Figure 49. Initially all of the release profiles were fitted using the first order kinetic model (equation [2]) and the fits to the data are shown in the Table 11. The parameters $Q_{max}$ and $k_1$ obtained after fitting this release data with [2] are listed in Table 11.

From the release data shown in Table 11, it can be concluded that the total amine group loading has an effect on the release of the aspirin. The first order rate constant, $k_1$, is approximately the same (~0.03 $min^{-1}$) for SBA-15 and SBA-15-PS1 samples with an exception for SBA-15-PS2 in which the $k_1$ is larger (0.33 $min^{-1}$). This can be due to the lack of the goodness of the fit in case of the SBA-15-PS2 sample. From the parent aspirin loaded SBA-15 to the amine functionalized samples, the maximum release ($Q_{max}$) of the drug decreased from 67% to 26% most likely due to increased pore blocking due to the higher APTES content

A comparison of the loading and release for the different samples is provided in Figure 49. The loading of aspirin into APTES functionalized SBA-15 was enhanced by 40% relative to the unfunctionalized SBA-15. The increase in aspirin loading in the amine functionalized SBA-15 materials is attributed to the favorable amine group and aspirin interaction.

The spectroscopic studies (FTIR and solid state NMR) indicate that the aspirin molecules are loaded intact into the SBA-15 samples. The NMR data supports this

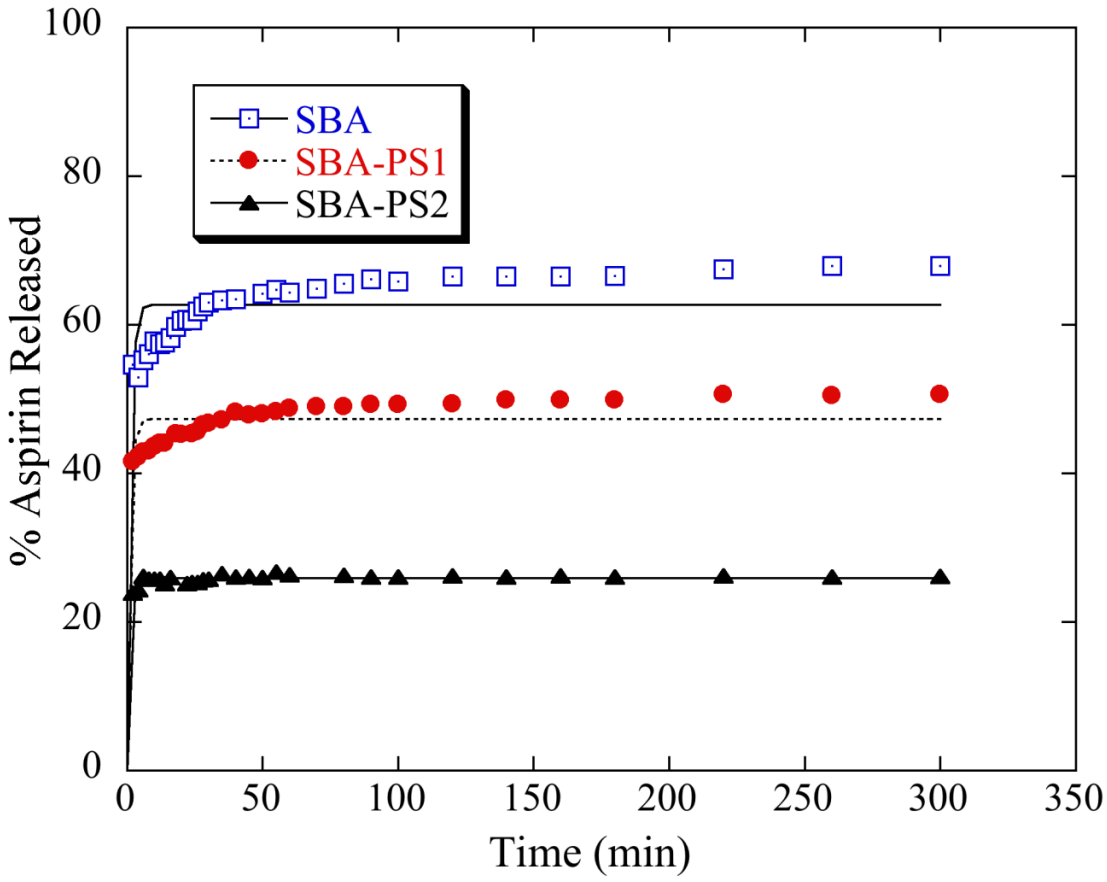


Figure 49. Drug release profiles for different SBA-15 type materials (a) SBA-15 with aspirin, (b) SBA-15-PS1 with aspirin, and (c) SBA-15-PS2 with aspirin

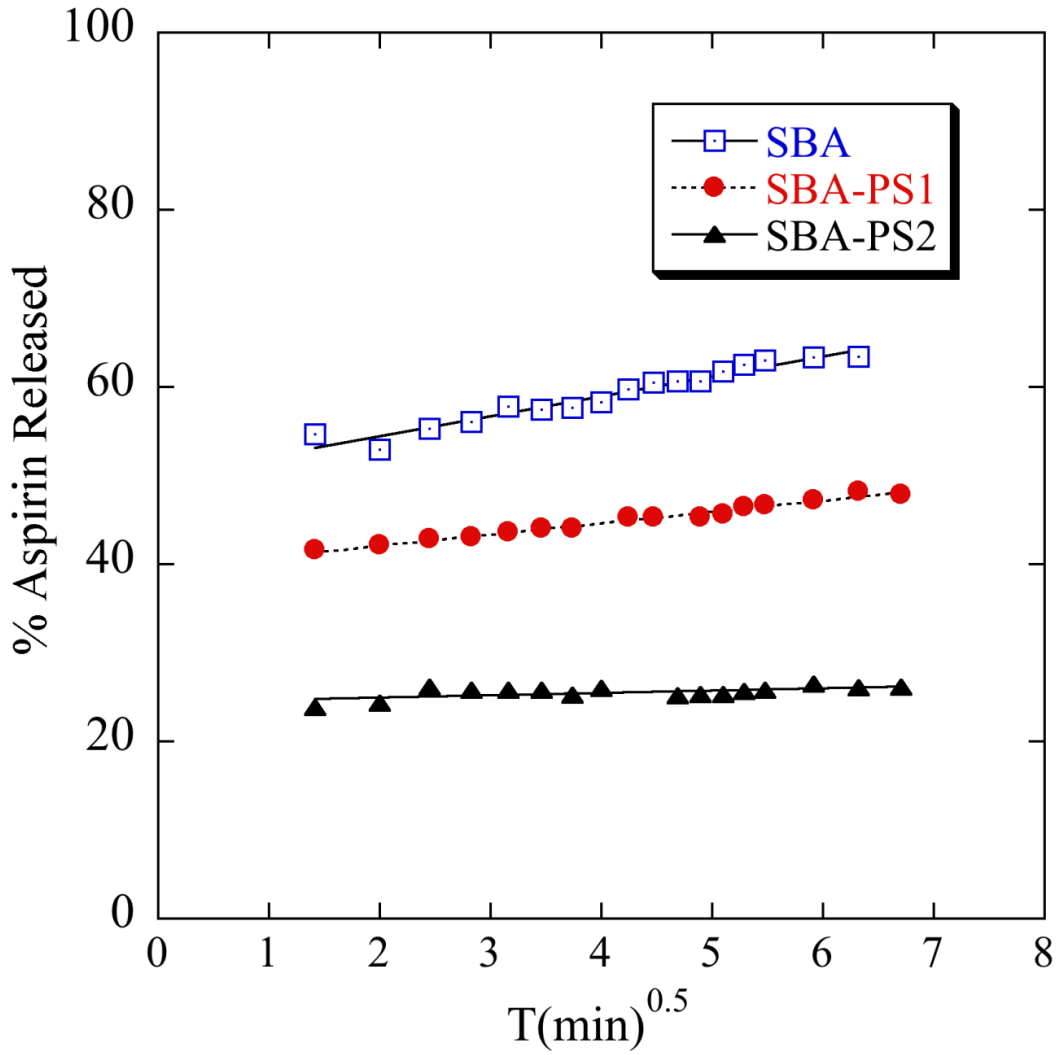


Figure 50. Higuchi model fit for the drug release profiles from SBA-15 mesoporous silica

interpretation as well in that the cross-polarization is not very efficient for aspirin. on SBA-15 and this is attributed to motion of the aspirin in the pore which suggests weak interactions with the framework consistent with hydrogen bonding to the silanol groups of the mesoporous silica. The SBA-15-PS-Aspirin $^{13}C$ NMR spectra are broadened relative to the physical mixture of SBA-15 and aspirin and also the carbonyl carbon peak is observed in the $^{13}C$-$^{1}H$ CP-MAS experiments. These observations indicate that the motion is restricted in the amine functionalized SBA-15 samples relative to the parent SBA-15. Previous NMR studies of ibuprofen on mesoporous materials exhibit similar behavior with respect to the $^{13}C$-$^{1}H$ cross polarization NMR. A shift of the $^{13}C$ phenyl group carbon resonances of aspirin is also observed in the $^{13}C$ NMR suggesting that the phenyl group of aspirin interacts with the SBA-15 host. Previous studies on MCM-41 with aspirin have showed the interaction of the phenyl system with the pore wall which is responsible for the shift of the aromatic peaks in the NMR spectrum.[128]

The release data can be understood by considering the molecular level details revealed in the FTIR and NMR experiments. For the APTES functionalized SBA-15 samples, the aspirin undergoes a stronger interaction with the amine group and is released to a lesser extent relative to the parent SBA-15. In case of post-synthesis SBA-15 samples, the release reaches a plateau at approximately 50% and 26% aspirin release for PS1 and PS2 samples. A similar effect has been observed previously for sodium alendronate loaded on SBA-15 functionalized with APTES in different ways.[161]

## 7.5 Conclusions

This study investigates the interaction of aspirin with large pore SBA-15. Both the parent and the functionalized SBA-15 were studied for aspirin loading and release. With

an increase in the amine content in the mesoporous silica the amount of the aspirin loaded increased. The increase in the aspirin loading was not significant when the higher and lower amounts of APTES samples were compared. Nevertheless, the extent of release of aspirin in the phosphate buffer was significantly different for both parent and functionalized samples. This can be explained on the basis of the pore blocking in post synthesis grafting method. As the concentration of the APTES was increased in the functionalization reaction, the probability by which the aspirin can be released was decreased. The release profiles for both the parent and the APTES functionalized SBA-15 samples were fitted using a first order kinetic exponential decay model. The difference in release models was explained by the relatively weaker interaction of aspirin with the parent SBA-15 relative to the APTES functionalized samples. Solid state NMR and FTIR provided detailed molecular information about the aspirin binding to the mesoporous silica host that supported these conclusions.

# CHAPTER 8

# ASPIRIN TEMPLATED MESOPOROUS SILICA SYNTHESIS

## 8.1 Abstract

A novel drug templated synthesis of silica particles is proposed using aspirin as a templating agent. Aspirin molecules were encapsulated with a one-step co-condensation mechanism using aminopropyl triethoxysilane and tetraethylorthosilicate for the synthesis of aspirin templated silica material. The resulting material was characterized using different physicochemical techniques such as powder X-ray diffraction, nitrogen adsorption isotherms, and thermogravimetric analysis. Spectroscopic characterization using FTIR and $^{13}C$ CP-MAS NMR of the silica based material shows the presence of aspirin molecules. The drug release profile of the aspirin templated silica showed a sustained release profile.

## 8.2 Introduction.

Mesoporous silica materials have been used in the field of drug delivery for over a decade now. The major area of focus in the literature so far has been the ability to tune the pore size, pore morphology, and tailorable properties such as functionalization of the surface in these silica based materials. The general strategy to synthesize these materials uses structure directing agents which act as templates for the formation of the mesostructure. The synthesis conditions require a sol-gel approach method which typically uses surfactants or block copolymers as the templates. Mesoporous silicas such as MCM-41, SBA-15 have been synthesized using anionic and cationic surfactants.[215,216] Recently, mesoporous silica using the biocompatible surfactants has been synthesized. Based on the concentration of the surfactant in the synthesis system, a variety of

nanostructures can be obtained including from spheres, tubes, films.[217,218] The other important parameters which play a contributing role in the overall structure of the silica system are temperature and pH. In addition to the surfactants as templates, the literature precedent shows the use of organic polymers for the synthesis of these materials.[219] Quantum dots have also been used as the core of the mesoporous silica synthesis.[220] The use of small organic molecules, such as amino acids,[221,222] or toluene in addition to the surfactant systems has been shown to formulate amorphous/mesoporous silicas with ordered morphology. Due to their large surface areas and tunable pore volumes, mesoporous silica materials have been widely used in different applications such as adsorption, catalysis, biosensors and drug delivery.

There has been a considerable amount of research done over the last decade for formulating a drug delivery system using mesoporous silica materials. Such drug delivery systems will aid the field of modern medication and will help in retaining the pharmaceutical activity of the drug molecules over a longer period of time when administered. Other systems which have shown potential interest for being used as drug delivery systems are micelles,[223,224] polymeric nanoparticles such as chitosan nanoparticles,[225] and liposomes.[226] Mesoporous silica has emerged as an interesting drug delivery system due to tunable surface properties such as pore sizes, and surface modifications. In addition, the non-toxic and biocompatible nature of these mesoporous silica materials makes them an attractive candidate for drug delivery systems. The literature precedent shows the use of mesoporous silica materials in the delivery of various drugs such as ibuprofen, aspirin, and doxorubicin. The basic mode of loading the drugs in mesoporous silica systems is by a post synthetic route in which the mesoporous

silica system is synthesized and then is used to load the drug molecules. The interaction of the drugs with the pore walls of silica can be hydrogen bonding or by covalent linking with the grafted groups on the silica surface. There is a need to design a system in which the drug molecules can be loaded in the silica material during its synthesis process. The advantages of the one step system for encapsulating drug molecules will be (i) avoiding the use of harsh treatments such as calcination, extraction of the template, and (ii) reducing the number of steps required for the processing of the drug delivery system.

In the study reported here, aspirin was chosen as a model drug due to its small molecular size, good pharmacological activity, and short biological half-life. In addition, it has a carboxyl group that can interact with surface silanol groups or amino groups on the pore walls and may be useful for the controlled drug release (Figure 51). In this study, we investigate a new method for encapsulating aspirin molecules in the silica system by using aspirin as a templating agent during the synthesis of mesoporous silica.

## 8.3. Experimental Details

### 8.3.1. Materials Required & Synthetic Procedure

Materials Required: (3-Aminopropyl)triethoxysilane (Sigma Aldrich, 99%), Tetraethyl orthosilicate (Sigma Aldirch, 98%), Aspirin (Sigma Aldrich, 99%), and de-ionized water.

Synthetic Procedure: In a typical procedure, known amount of drug (aspirin) was first dissolved in water. To this clear solution, APTES solution was added dropwise until the pH of the solution became neutral. The contents were stirred for 2 h at room temperature followed by the addition of TEOS. The final reaction mixture was then stirred for 24 h at room temperature followed by further heating under static conditions in

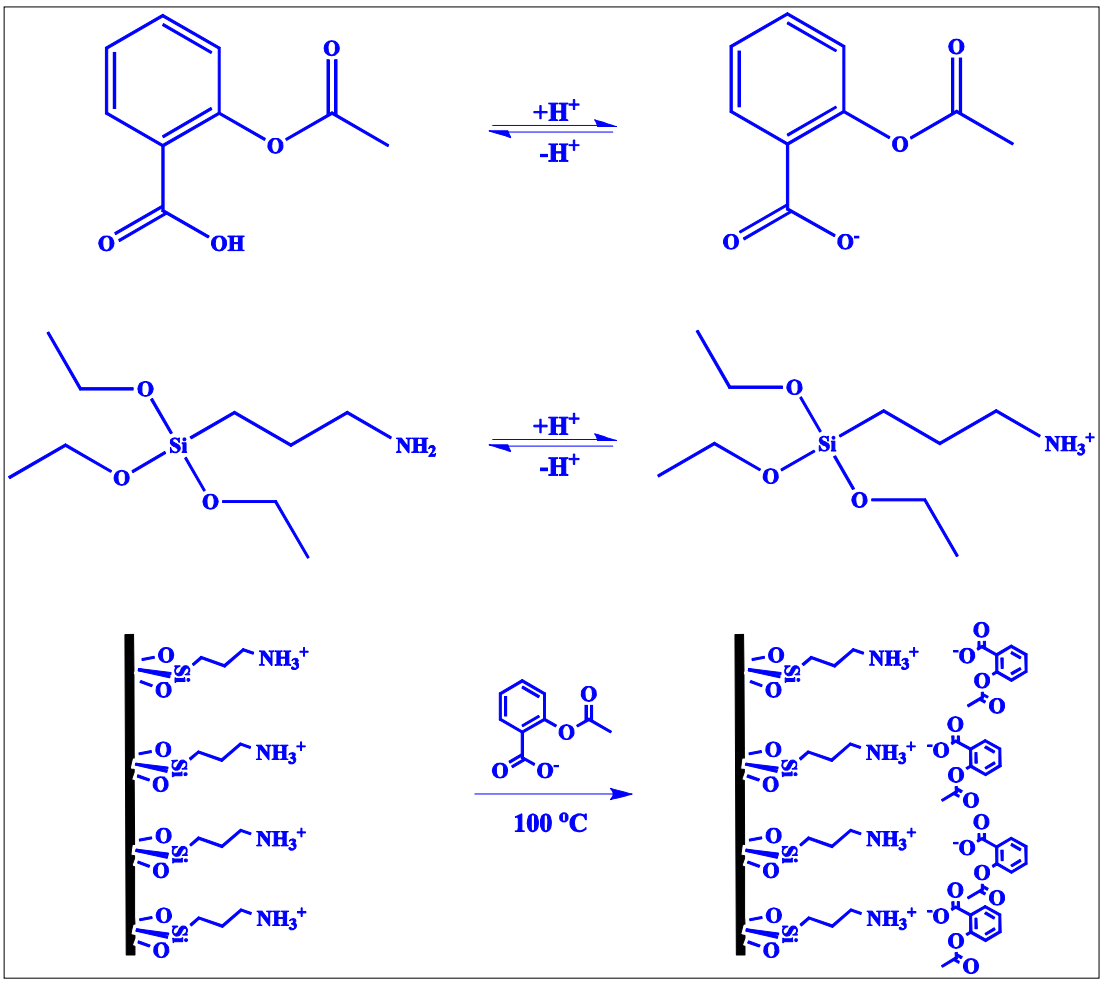


Figure 51. Schematic Representation of Aspirin templated amorphous silica

a stainless steel autoclave for 24 h. The white colored reaction mixture was filtered, washed with de-ionized water and dried in an oven kept at 100 °C for 24 h.

### 8.3.2. Characterization

The aspirin templated silica material was characterized using a variety of different techniques. The presence of diffraction peaks in the silica material was confirmed using powder X-ray diffraction (pXRD) (Siemens D5000 X-ray diffractometer with Cu Kα and a nickel filter). A broad-range pattern ($2\theta$ = 1 to 10 with a 0.02 step size, 1 s/step) was collected for the aspirin templated silica material.

Surface areas of the aspirin templated silica sample was measured using nitrogen adsorption and the BET method on a Nova 1200 Nitrogen Adsorption Instrument (Quantachrome). Typically, 100 mg of powder was dried overnight at 120 °C in vacuum. A 7-point BET isotherm was then recorded and the specific surface area was calculated for the samples ($S_{tot}$). A 50-point adsorption/desorption isotherm was measured and used for calculation of total pore volume. The total pore volume ($V_{tot}$) was calculated by measuring the amount of adsorbed nitrogen at 0.97 $P/P_o$.

Thermogravimetric analysis (TGA) was performed using the TA Q5000 TGA instrument with a heating rate of 5 °C/min under nitrogen flow. While samples were heated from room temperature to 800 °C, the weight change was recorded. The TGA data was used to calculate the cumulative content aspirin and APTES loading.

FT-IR spectra were recorded using the Nicolet FT-IR spectrometer and the sample was pressed into disk by mixing them in the ratio of 1:5 with KBr. The spectra were recorded in the range of 400-4000 $cm^{-1}$.

Nuclear magnetic resonance (NMR) experiments were conducted on a 500 MHz Bruker Avance III spectrometer with 3.2 mm zirconia rotors. $^{13}C$-$^{1}H$ cross polarization magic angle spinning (CPMAS) experiments were conducted on the aspirin and aspirin templated material. The $^{13}C$-$^{1}H$ CP-MAS experiments were conducted with the MAS spinning speed of 10 kHz with adamantane as the reference material.

Known amounts of the aspirin templated silica material was mixed (1 mg/ml) with simulated body fluid at pH 7.4 and 37 °C. The simulated body fluid was made using known amounts of sodium monobasic phosphate and sodium dibasic phosphate. The samples were stirred at ca. 100 rpm and 2 ml aliquots were removed at regular intervals. The aliquots were centrifuged in order to ensure no solid was in suspension and the supernatants were analyzed for aspirin with UV –Vis spectroscopy (Varian Cary 100 Scan) at $\lambda$ = 296 nm. The amount of released aspirin was calculated using the following equation:

$$C_{tcorr} = C_t + \frac{v}{V}\sum_0^{t-1} C_t \qquad (16)$$

where $C_{tcorr}$ is the corrected concentration at time t (corrected to account for changes in volume), $C_t$ is the apparent concentration at time t, v is the volume of the sample taken, and V is the total volume of the solution.

## 8.4 Results and Discussion

Figure 52 shows the powder X-ray diffraction patterns for the aspirin templated silica material. From the diffractogram, no observable diffraction pattern is obtained. Wang and coworkers obtained similar diffraction patterns, which are typical for materials which possess a very low degree of ordering in their structure.[217] There is a small

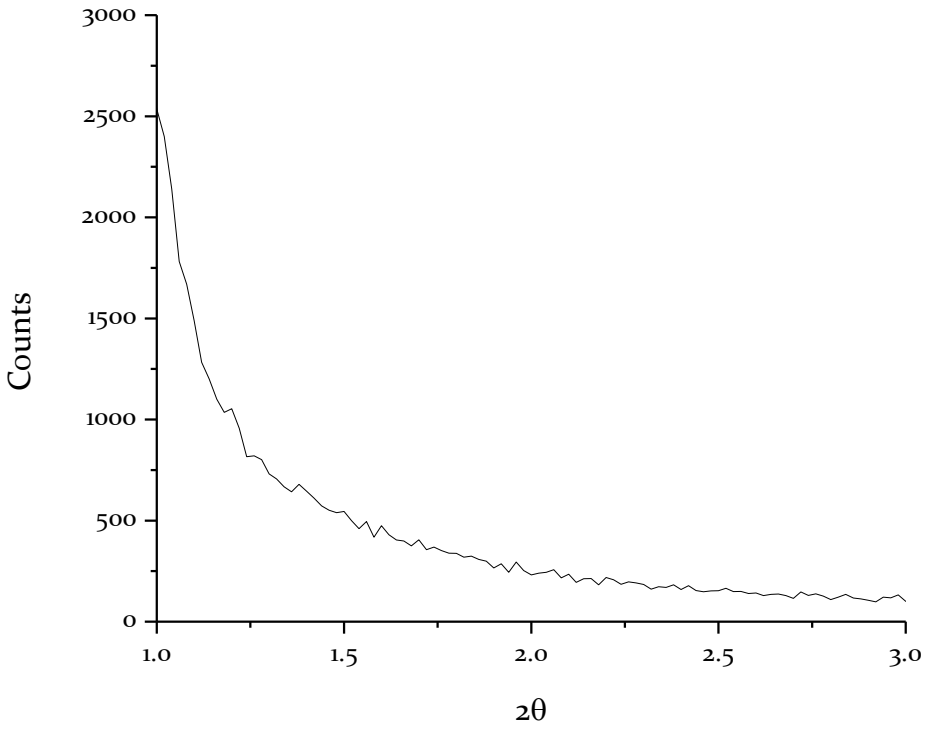


Figure 52. Powder X-ray diffraction pattern of aspirin templated silica material

.

shoulder 2θ ~ 1.2, which indicates the less ordered mesostructure, due to the presence of organic molecules in the pore structure.[224]

Nitrogen adsorption-desorption isotherm measurements were performed on the as-synthesized material (Figure 53). The material possess a type IV isotherm which is typical for porous materials having pore diameters of more than 2 nm. In case of aspirin templated material, the capillary condensation occurs from partial pressures of 0.4 to 1.0, which accounts for the presence of large pores in the material. The hysteresis loop for the nitrogen isotherm bears a close resemblance to amorphous silica materials. The surface area for the drug template material was determined to be 245 $m^2/g$ with a pore volume of 0.458 $cm^3/g$. This pore volume of the drug template material is similar to amine functionalized mesoporous silica MCM-41 loaded with aspirin.

Figure 54 shows the thermogravimetric plots of the aspirin templated material and the parent aspirin. The cumulative weight loss for the aspirin templated material was found out to be 19 wt%. This weight change consists of both the APTES moieties as well as the aspirin drug molecules present in the co-condensed system.

Solid State NMR and FTIR Spectroscopy: $^{13}$C-CP-MAS experiments were conducted on both the aspirin templated silica as well as the parent aspirin. $^{13}$C NMR spectra are shown in Figure 55. Characteristic resonances corresponding to aspirin and APTES were observed in the spectra. The peak at approximately 170 ppm was assigned to the carbonyls of the carboxylic acid and ester groups of the aspirin which are not resolved. The peaks in the region from 116 ppm – 150 ppm were assigned to the aromatic carbons of the phenyl ring in aspirin. The peak from the methyl group of aspirin was observed at approximately 19 ppm with two additional peaks coming from the propyl

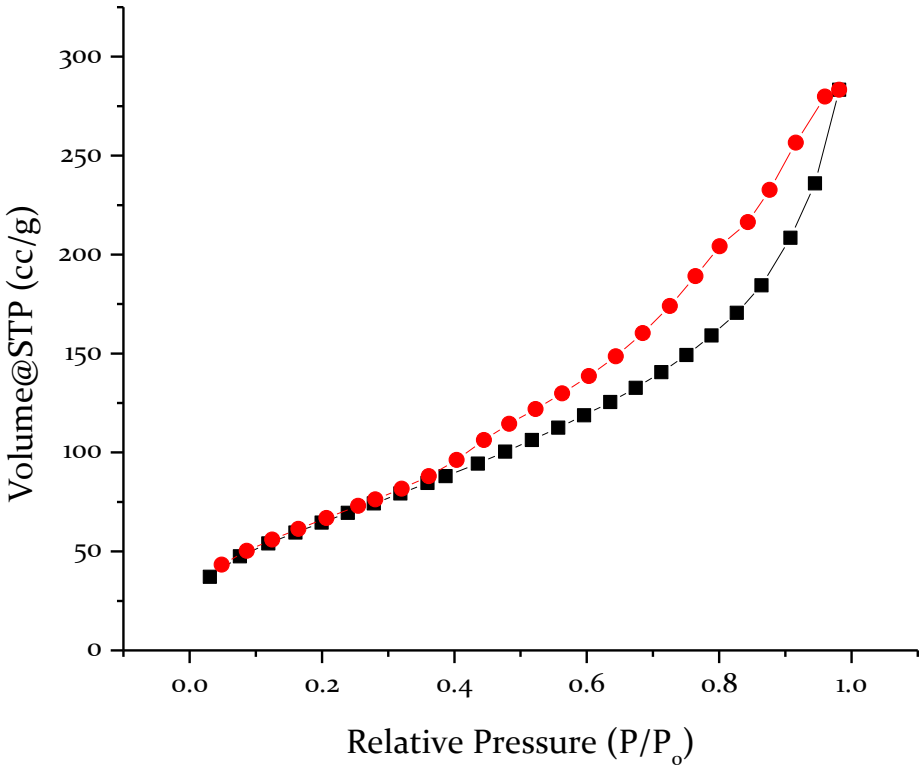


Figure 53. Nitrogen Adsorption-Desorption Isotherm for the aspirin template silica particles.

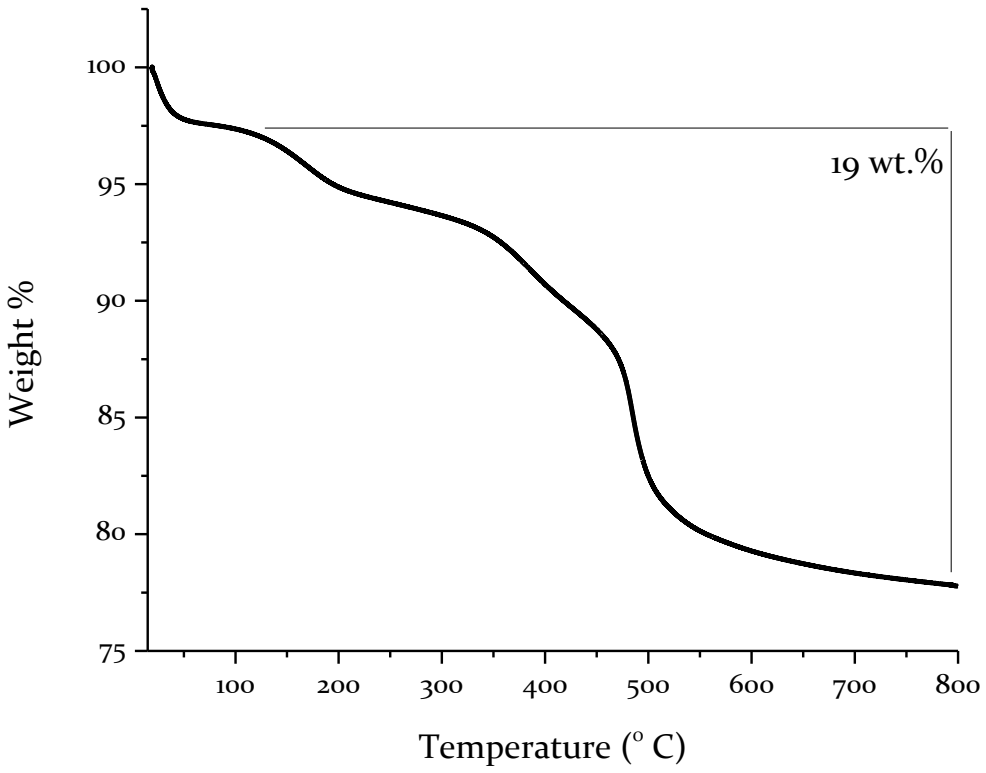


Figure 54. Thermogram of aspirin template silica particles showing the characteristic weight changes due to the aspirin molecule.

chain of the APTES moiety for the APTES present in the drug templated system. The phenyl ring carbon peaks for aspirin templated silica are shifted relative to the pure aspirin indicating that the phenyl ring interaction as one of the contributing factors for the stabilization of the drug in the co-condensed system. A similar shift has been observed for aspirin loaded in polymeric hosts, mesoporous silica and zeolites.

The FTIR spectra of aspirin template silica and aspirin are shown in Figure 56. The peaks around 1000 $cm^{-1}$ correspond to the Si-OH vibrations with a shoulder at 1200 $cm^{-1}$ accounting for the formation of the Si-O-Si framework. The peak at 1640 $cm^{-1}$ is attributed to the bending more vibrations of the water present in the co-condensed system. Relatively weaker peaks are also observed at 1486, 1460 and 1380 $cm^{-1}$ and these are attributed to aspirin phenyl group vibrations. The characteristic peak assigned to the bending mode of the amine groups is observed at ~ 1570 $cm^{-1}$, with the peak around 2800 $cm^{-1}$ attributed to the presence of C-H stretches arising from the APTES and the aspirin moieties present in the co-condensed system. The carbonyl vibration at ~1700 $cm^{-1}$ is not observed and this is attributed to the strong interaction of the carbonyl carbon of the carboxylic acid with the amine groups. This lack of a carbonyl vibration at ~1700 $cm^{-1}$ has been observed in previous studies of aspirin on various mesoporous silica functionalized materials and has been attributed to the formation of a carboxylate species. As a consequence of the absence of the carbonyl vibrations, there may exist the presence of $COO^{-}$---$NH_3^{+}$ type of bonding formation in the silica structure.

Drug Release Studies: The aspirin release profile for the aspirin templated silica system are shown in Figure 57. Drug release from porous media can follow several different models. In some cases, the release process is governed by Fick's diffusion and

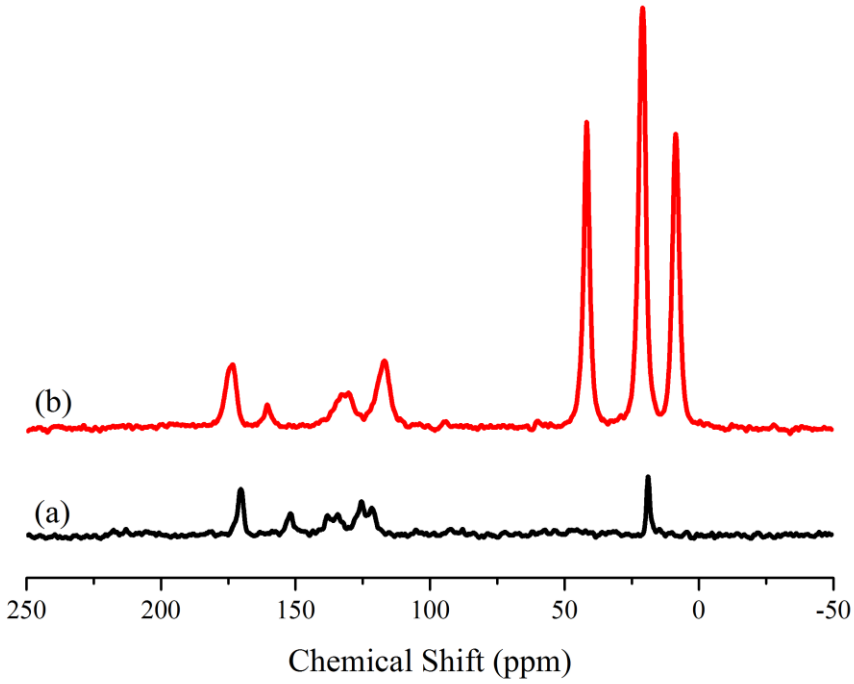


Figure 55. $^{13}C$ CP-MAS Solid State NMR for (a) aspirin (b) aspirin template mesoporous silica

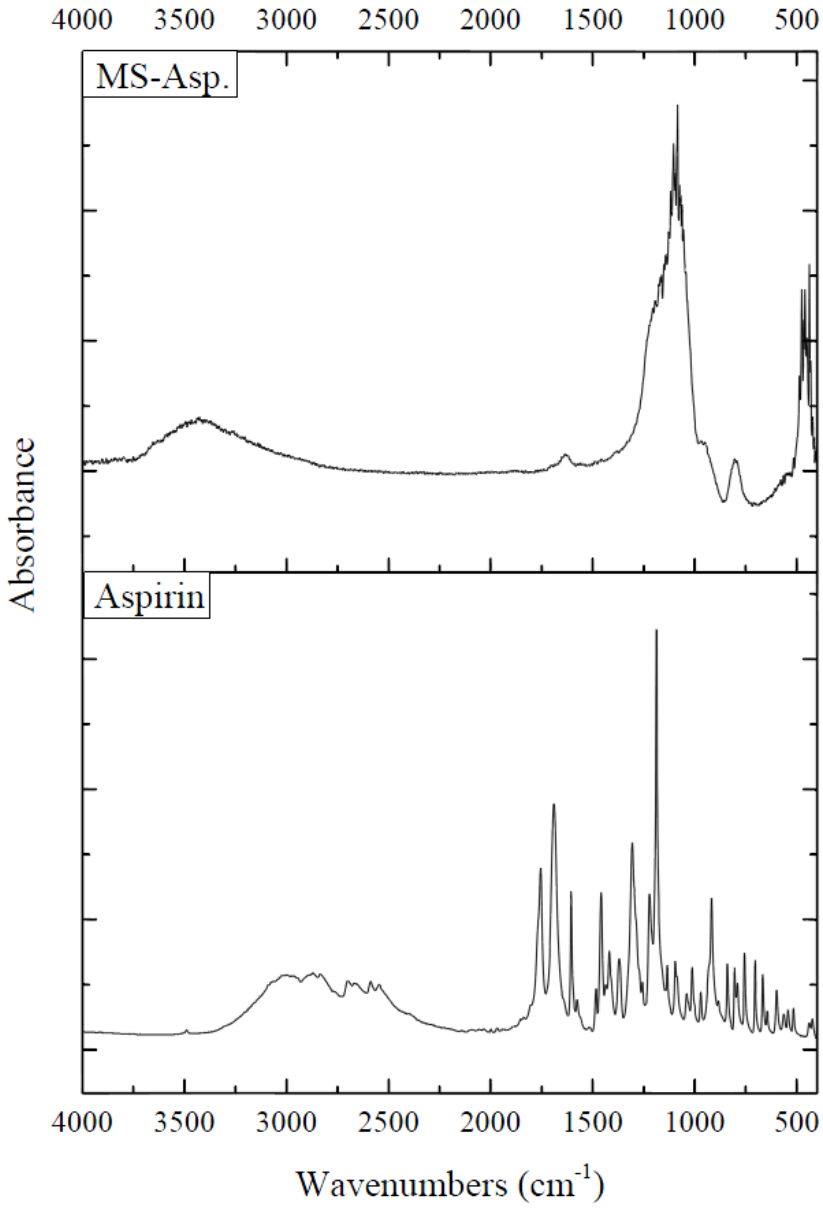


Figure 56. FT-IR spectra of the parent aspirin (bottom) and the aspirin templated silica material (top)

can be described using a simplified Higuchi model, $Q=K_H t^{0.5}$, where Q=the amount of drug release, $K_H$ is the Higuchi dissolution constant, and t is the time. The Korsmeyer-Peppas model is similar except that a release exponent, n, is introduced into the model such that $Q=at^n$, where a is a constant. The drug release follows the first-order kinetic exponential decay model, with the equation represented as:

$$Q = Q_{max}(1 - \exp(-k_1 t)) \qquad (17)$$

where Q is the amount of drug released in time t, $Q_{max}$ is the maximum amount of drug released and $k_1$ is the first order release constant. The Korsmeyer-Peppas model has been used to describe the release of aspirin from bimodal mesoporous silica materials. For amine-modified MCM-41 and SBA-15, the drug release for ibuprofen and sodium alendronate has been described using the first order kinetic model described by [3]. Preliminary investigations on the drug release profile of the aspirin templated silica system showed a release profile similar to that of mesoporous systems loaded with aspirin. The amount of aspirin released is calculated by assuming that all of the aspirin taken at the start of the reaction has been encapsulated in the silica material. The release studies were carried over a period of 24 h in order to make sure that the release of the drug from the templated system was complete. Nearly, 30% of the aspirin is released in the first 5 h, which plateaus over a period of 24 h. The parameters obtained after fitting the data to the exponential decay model shows the maximum release extent to be 33 % with the rate constant for the release as 0.004 $min^{-1}$.

## 8.5 Conclusions

Aspirin templated mesoporous silica was successfully synthesized using aspirin as the templating agent. The condensation of aspirin in the one step pathway results from the

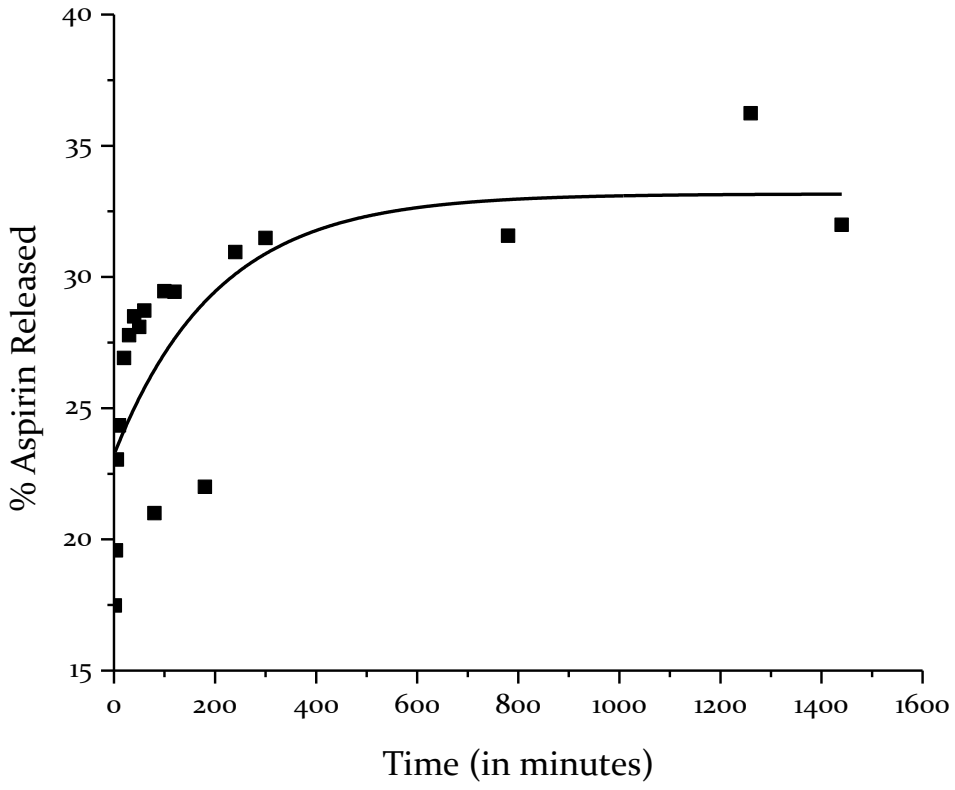


Figure 57. Drug Release profile from the aspirin template system

interaction between the negatively charged carboxylate groups of aspirin and the positively charged amine groups of the APTES moieties. Both FT-IR and $^{13}C$ CP-MAS NMR studies showed the presence of the aforementioned observation as well as the presence of aspirin intact in the drug templated silica material. The drug release profile followed the first order exponential decay mechanism of drug release. This novel drug templated silica system will enable us to design new systems with encapsulated biomolecules.

# CHAPTER 9

# CONCLUSIONS AND FUTURE WORK

## 9.1 Conclusions

This thesis investigates the interaction of small drug molecules with zeolites and mesoporous silica. The thesis can be divided into two major sections one which involves the interaction of the drug molecules with zeolites and the second with mesoporous silica materials. Zeolite HY has been extensively studied for loading and release of small drug molecules (aspirin, 5-FU) using various physical techniques. It was shown that the drug loading and release in zeolite HY is a function of the $SiO_2/Al_2O_3$ content of the zeolite. In addition, the drug loading and release also changes with the polarity of the drug. The loading of aspirin in zeolite HY was highest in lowest $SiO_2/Al_2O_3$ ratio whereas the release was fastest in that zeolite HY. The extent of release of aspirin decreased as the $SiO_2/Al_2O_3$ ratio was increased, accounting for the critical contribution of the amount of aluminum. In case of 5-FU, the trend observed was opposite to that of aspirin, the extent of release of 5-FU from the lowest $SiO_2/Al_2O_3$ ratio was the lowest. This basic difference can be explained based on the difference in the polarities of the two drug molecules. As a consequence, the nature of interaction with the release medium is different when the drug loaded zeolite materials were released in the physiological pH. The drug loaded zeolites were extensively characterized using spectroscopic techniques such as FTIR and solid state NMR, in order to obtain the molecular level insight of the drug molecules inside the micropores of the zeolite. $^{27}$Al MAS NMR measurements showed a decrease in the intensity of the octahedral peak intensity and an increase in the tetrahedral peak intensity after drug loading in the host zeolitic materials. This trend was observed in both the drug

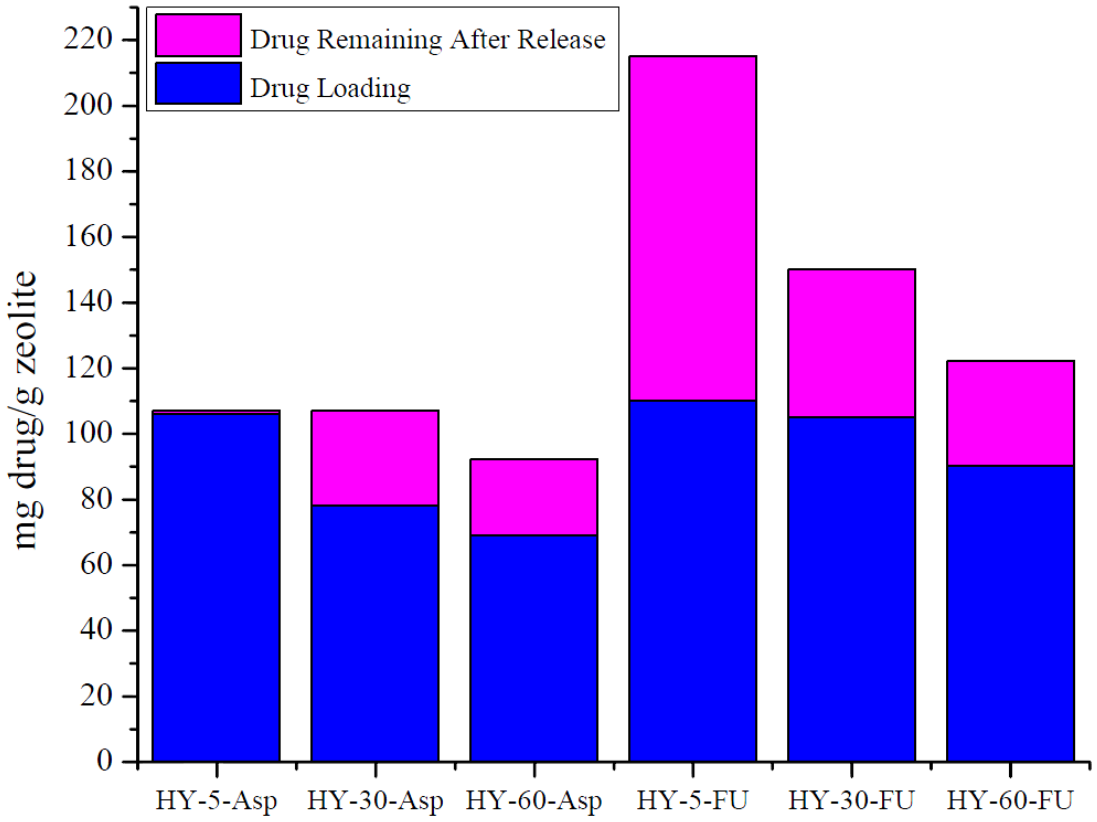


Figure 58. Comparison of loading of different drug molecules in the host zeolite HY

molecules (aspirin, 5-FU), which was attributed to the conversion of octahedral Al to the tetrahedral Al after drug loading (Figure 58). Quantum calculations supported the hypothesis of the presence of the aluminum-aspirin complex in the zeolite micropores.

Mesoporous silica was the other host material which was studied towards the loading and release of the drug, aspirin. MCM-41 and SBA-15 were the two different types of mesoporous silica which were used as the host materials. Amine functionalization was carried out on both MCM-41 and SBA-15 and the effect of amine functionalization was studied towards the loading and release of the aspirin in these mesoporous materials. In case of MCM-41, two different methods of amine functionalization were used namely co-condensation method and post synthesis method. It was found that the co-condensation method of functionalization produced highest aspirin loadings and showed the least amount of the drug released. This was attributed to the distribution of the functional groups on the interior walls of mesoporous silica. In case of postsynthesis method, the loadings did not increased significantly with an increase in the amine content and this can be explained due to pore blocking by the functional groups during this method of functionalization. In case of SBA-15 mesoporous materials, with higher amine functionalization, higher aspirin loadings were achieved and a slower release profile was observed. Both the materials were characterized using FTIR and solid state NMR. The change in the chemical shift of aromatic carbon peaks in the $^{13}C$ NMR spectra was accounted due to the orientation of the aspirin molecule parallel to the pore wall of the mesoporous silica. This explanation was complemented by the molecular dynamics simulations carried on the mesoporous silica containing aspirin molecule.

Finally, the last chapter discusses the synthesis of the mesoporous silica without the use of the sacrificial template. The synthesis was carried out in the presence of aspirin molecule acting as a template for the formation of mesoporous silica. APTES was used as the co-template which helps to make the silica framework in conjunction with the silicon source. The formation of the aspirin templated mesoporous silica was confirmed using various physical techniques. FTIR and solid state NMR showed the presence of the aspirin molecules in the system and confirmed the formation of the silica network. The drug release of the aspirin templated system showed a sustained drug release profile.

## 9.2 Future Work

Zeolites have shown their potential in the applications of drug delivery and other biomedical applications such as imaging. The use of zeolites as targeted delivery devices still remains the major focus of researchers. An improvement in the fundamental way in which the zeolites communicates with the drug/biomolecules may result in interesting systems. The coating of the drug loaded zeolites with gold nanoparticles may open the window for the photodynamic therapeutic properties in addition to the drug loading and release properties.

Mesoporous silica has been the most promising material for drug delivery/biomedical applications. Many coupled mesoporous systems such as magnetite-mesoporous silica have been synthesized and have shown potential in addressing hyphenated properties of mesoporous silica systems as drug delivery vehicles.[139] One area which still needs a focus is the hybrid mesoporous material which encapsulates quantum dots either on its surface or present in the core of mesoporous silica shell system. Drug delivery using quantum dots and mesoporous silica will open a new

window for research in a sense that this drug delivery system will not only deliver the drug cargo but will also benefit from the pharmaceutical advantages of quantum dots. In addition, novel template free methods should be developed in order to minimize the variables in the mesoporous silica synthesis. Biomolecules should be used as templates in order to synthesize mesostructures.

# REFERENCES


(1) McCusker, L. B.; Baerlocher, C. Chapter 3 Zeolite structures. In *Studies in Surface Science and Catalysis*; H. van Bekkum, E. M. F. P. A. J., Jansen, J. C., Eds.; Elsevier, 2001; Vol. Volume 137; pp 37.

(2) Maesen, T.; Marcus, B. Chapter 1 The zeolite scene—An overview. In *Studies in Surface Science and Catalysis*; H. van Bekkum, E. M. F. P. A. J., Jansen, J. C., Eds.; Elsevier, 2001; Vol. Volume 137; pp 1.

(3) Kunkeler, P. J.; Downing, R. S.; Bekkum, H. v. Chapter 21 The use of bulky molecules as probes for investigating the contributions of the external and internal pore-wall activities of zeolite catalysts. In *Studies in Surface Science and Catalysis*; H. van Bekkum, E. M. F. P. A. J., Jansen, J. C., Eds.; Elsevier, 2001; Vol. Volume 137; pp 987.

(4) Degnan Jr, T. F. *Topics in Catalysis* **2000**, *13*, 349.

(5) http://www.iza-structure.org.

(6) Ramamurthy, V. *Journal of Photochemistry and Photobiology C: Photochemistry Reviews* **2000**, *1*, 145.

(7) Song, W.; Justice, R. E.; Jones, C. A.; Grassian, V. H.; Larsen, S. C. *Langmuir* **2004**, *20*, 4696.

(8) Song, W.; Justice, R. E.; Jones, C. A.; Grassian, V. H.; Larsen, S. C. *Langmuir* **2004**, *20*, 8301.

(9) Song, W.; Li, G.; Grassian, V. H.; Larsen, S. C. *Environmental Science & Technology* **2005**, *39*, 1214.

(10) Bresinska, I.; Balkus, K. J., Jr. *The Journal of Physical Chemistry* **1994**, *98*, 12989.

(11) Li, W. S. L., Z. F.; Jing, F. Y.; Yang, X. G.; Li, X. J.; Pei, F. K.; Wang, X. X.; Lei, H. *Acta Chim. Sinica* **2007**, *65*, 2029.

(12) Platas-Iglesias, C.; Vander Elst, L.; Zhou, W.; Muller, R. N.; Geraldes, C. F. G. C.; Maschmeyer, T.; Peters, J. A. *Chemistry – A European Journal* **2002**, *8*, 5121.

(13) Young, S. W.; Qing, F.; Rubin, D.; Balkus, K. J.; Engel, J. S.; Lang, J.; Dow, W. C.; Mutch, J. D.; Miller, R. A. *Journal of Magnetic Resonance Imaging* **1995**, *5*, 499.

(14) Braschi, I.; Blasioli, S.; Gigli, L.; Gessa, C. E.; Alberti, A.; Martucci, A. *Journal of Hazardous Materials* **2010**, *178*, 218.

(15) Braschi, I.; Gatti, G.; Paul, G.; Gessa, C. E.; Cossi, M.; Marchese, L. *Langmuir* **2010**, *26*, 9524.

(16) Dyer, A.; Morgan, S.; Wells, P.; Williams, C. *Journal of Helminthology* **2000**, *74*, 137.

(17) Zhang, H.; Kim, Y.; Dutta, P. K. *Microporous and Mesoporous Materials* **2006**, *88*, 312.

(18) Horcajada, P.; Márquez-Alvarez, C.; Rámila, A.; Pérez-Pariente, J.; Vallet-Regí, M. *Solid State Sciences* **2006**, *8*, 1459.

(19) Di Renzo, F.; Testa, F.; Chen, J. D.; Cambon, H.; Galarneau, A.; Plee, D.; Fajula, F. *Microporous and Mesoporous Materials* **1999**, *28*, 437.

(20) Tanev, P. T.; Pinnavaia, T. J. *Chemistry of Materials* **1996**, *8*, 2068.

(21) Beck, J. S.; Vartuli, J. C.; Roth, W. J.; Leonowicz, M. E.; Kresge, C. T.; Schmitt, K. D.; Chu, C. T. W.; Olson, D. H.; Sheppard, E. W. *Journal of the American Chemical Society* **1992**, *114*, 10834.

(22) Huo, Q.; Margolese, D. I.; Stucky, G. D. *Chemistry of Materials* **1996**, *8*, 1147.

(23) Cai, Q.; Luo, Z.-S.; Pang, W.-Q.; Fan, Y.-W.; Chen, X.-H.; Cui, F.-Z. *Chemistry of Materials* **2001**, *13*, 258.

(24) Davidson, A. *Current Opinion in Colloid & Interface Science* **2002**, *7*, 92.

(25) Lin, H.-P.; Kao, C.-P.; Mou, C.-Y.; Liu, S.-B. *The Journal of Physical Chemistry B* **2000**, *104*, 7885.

(26) Giraldo, L. F.; López, B. L.; Pérez, L.; Urrego, S.; Sierra, L.; Mesa, M. *Macromolecular Symposia* **2007**, *258*, 129.

(27) Ramírez, A.; Lopez, B. L.; Sierra, L. *The Journal of Physical Chemistry B* **2003**, *107*, 9275.

(28) Zhao, X. S.; Lu, G. Q. *The Journal of Physical Chemistry B* **1998**, *102*, 1556.

(29) Hoffmann, F.; Cornelius, M.; Morell, J.; Fröba, M. *Angewandte Chemie International Edition* **2006**, *45*, 3216.

(30) Inagaki, S.; Guan, S.; Fukushima, Y.; Ohsuna, T.; Terasaki, O. *Journal of the American Chemical Society* **1999**, *121*, 9611.

(31) Melde, B. J.; Holland, B. T.; Blanford, C. F.; Stein, A. *Chemistry of Materials* **1999**, *11*, 3302.

(32) Asefa, T.; MacLachlan, M. J.; Coombs, N.; Ozin, G. A. *Nature* **1999**, *402*, 867.

(33) Göltner-Spickermann, C. *Current Opinion in Colloid & Interface Science* **2002**, *7*, 173.

(34) Sayari, A.; Hamoudi, S. *Chemistry of Materials* **2001**, *13*, 3151.

(35) Soler-Illia, G. J. d. A. A.; Crepaldi, E. L.; Grosso, D.; Sanchez, C. *Current Opinion in Colloid & Interface Science* **2003**, *8*, 109.

(36) Soler-Illia, G. J. d. A. A.; Sanchez, C.; Lebeau, B.; Patarin, J. *Chemical Reviews* **2002**, *102*, 4093.

(37) Zhao, X. S.; Lu, G. Q.; Millar, G. J. *Industrial & Engineering Chemistry Research* **1996**, *35*, 2075.

(38) Grün, M.; Kurganov, A. A.; Schacht, S.; Schüth, F.; Unger, K. K. *Journal of Chromatography A* **1996**, *740*, 1.

(39) Inagaki, S.; Ogata, S.; Goto, Y.; Fukushima, Y. Mesoporous materials derived from layered silicates and the adsorption properties. In *Studies in Surface Science and Catalysis*; L. Bonneviot, F. B. C. D. S. G., Kaliaguine, S., Eds.; Elsevier, 1998; Vol. Volume 117; pp 65.

(40) Cesteros, Y.; Haller, G. L. *Microporous and Mesoporous Materials* **2001**, *43*, 171.

(41) Coluccia, S.; Marchese, L.; Martra, G. *Microporous and Mesoporous Materials* **1999**, *30*, 43.

(42) Góra-Marek, K.; Datka, J. *Applied Catalysis A: General* **2006**, *302*, 104.

(43) Hattori, H. *Chemical Reviews* **1995**, *95*, 537.

(44) Hunger, M.; Schenk, U.; Breuninger, M.; Gläser, R.; Weitkamp, J. *Microporous and Mesoporous Materials* **1999**, *27*, 261.

(45) Jentys, A.; Kleestorfer, K.; Vinek, H. *Microporous and Mesoporous Materials* **1999**, *27*, 321.

(46) Ryoo, R.; Ko, C. H.; Howe, R. F. *Chemistry of Materials* **1997**, *9*, 1607.

(47) Xu, M.; Wang, W.; Seiler, M.; Buchholz, A.; Hunger, M. *The Journal of Physical Chemistry B* **2002**, *106*, 3202.

(48) Lebeau, B.; Parmentier, J.; Soulard, M.; Fowler, C.; Zana, R.; Vix-Guterl, C.; Patarin, J. *Comptes Rendus Chimie* **2005**, *8*, 597.

(49) Lee, J.; Han, S.; Hyeon, T. *Journal of Materials Chemistry* **2004**, *14*, 478.

(50) Lee, J.; Kim, J.; Hyeon, T. *Advanced Materials* **2006**, *18*, 2073.

(51) Lu, A.-H.; Schüth, F. *Comptes Rendus Chimie* **2005**, *8*, 609.

(52) Ryoo, R.; Joo, S. H.; Jun, S. *The Journal of Physical Chemistry B* **1999**, *103*, 7743.

(53) Ryoo, R.; Joo, S. H.; Kruk, M.; Jaroniec, M. *Advanced Materials* **2001**, *13*, 677.

(54) *Small* **2011**, n/a.

(55) Hakami, O.; Zhang, Y.; Banks, C. J. *Water Research* **2012**, *46*, 3913.

(56) Andersson, J.; Rosenholm, J.; Areva, S.; Lindén, M. *Chemistry of Materials* **2004**, *16*, 4160.

(57) Gao, Q.; Xu, Y.; Wu, D.; Shen, W.; Deng, F. *Langmuir* **2010**, *26*, 17133.

(58) Zhu, Y.-f.; Shi, J.-l.; Li, Y.-s.; Chen, H.-r.; Shen, W.-h.; Dong, X.-p. *Microporous and Mesoporous Materials* **2005**, *85*, 75.

(59) Trewyn, B. G.; Giri, S.; Slowing, I. I.; Lin, V. S. Y. *Chemical Communications* **2007**, 3236.

(60) Trewyn, B. G.; Slowing, I. I.; Giri, S.; Chen, H.-T.; Lin, V. S. Y. *Accounts of Chemical Research* **2007**, *40*, 846.

(61) Bae, Y. H.; Huh, K. M.; Kim, Y.; Park, K.-H. *Journal of Controlled Release* **2000**, *64*, 3.

(62) Mittal, G.; Kumar, M. N. V. R. *Journal of Pharmaceutical Sciences* **2009**, *98*, 3730.

(63) Rösler, A.; Vandermeulen, G. W. M.; Klok, H.-A. *Advanced Drug Delivery Reviews* **2001**, *53*, 95.

(64) Uhrich, K. E.; Cannizzaro, S. M.; Langer, R. S.; Shakesheff, K. M. *Chemical Reviews* **1999**, *99*, 3181.

(65) Higuchi, T. *Journal of Pharmaceutical Sciences* **1961**, *50*, 874.

(66) Higuchi, T. *Journal of Pharmaceutical Sciences* **1963**, *52*, 1145.

(67) Kortesuo, P.; Ahola, M.; Kangas, M.; Leino, T.; Laakso, S.; Vuorilehto, L.; Yli-Urpo, A.; Kiesvaara, J.; Marvola, M. *Journal of Controlled Release* **2001**, *76*, 227.

(68) Lu, J.; Liong, M.; Zink, J. I.; Tamanoi, F. *Small* **2007**, *3*, 1341.

(69) Shen, J.; He, Q.; Gao, Y.; Shi, J.; Li, Y. *Nanoscale* **2011**, *3*, 4314.

(70) Xu, W.; Gao, Q.; Xu, Y.; Wu, D.; Sun, Y.; Shen, W.; Deng, F. *Powder Technology* **2009**, *191*, 13.

(71) Charnay, C.; Bégu, S.; Tourné-Péteilh, C.; Nicole, L.; Lerner, D. A.; Devoisselle, J. M. *European Journal of Pharmaceutics and Biopharmaceutics* **2004**, *57*, 533.

(72) Pecharsky, V. K. Z., P. Y. *New York: Springer* **2005**.

(73) Patterson, A. L. *Physical Reviews* **1939**, *56*, 978.

(74) Brunauer, S. E., P. H.; Teller, E. *Journal of the American Chemical Society* **1938**, *60*, 309.

(75) Barrett, E. P. J., L. G.; Halenda, P. P. *Journal of the American Chemical Society* **1951**, *73*, 373.

(76) Brown, M. E. *Introduction to Thermal Analysis* Chapman & Hall **1988**.

(77) Haines, P. J. *Principles of Thermal Analysis* Blackie A & P **1995**.

(78) Fifield, F. W. *Principles of Analytical Chemistry* Blackwell Science Ltd **2005**.

(79) Gore, K. U.; Abraham, A.; Hegde, S. G.; Kumar, R.; Amoureux, J.-P.; Ganapathy, S. *The Journal of Physical Chemistry B* **2002**, *106*, 6115.

(80) Jiao, J.; Kanellopoulos, J.; Wang, W.; Ray, S. S.; Foerster, H.; Freude, D.; Hunger, M. *Physical Chemistry Chemical Physics* **2005**, *7*, 3221.

(81) Joseph Goldstein, D. E. N., D C. Joy, C E. Lyman, P Echlin, E LIfshin, L Sawyer, and J R. Michael. *Springer* **2003**.

(82) Atkins, P. *Physical Chemistry* Freeman, New York **1998**, *6th ed.*

(83) Levine, I. N. *Quantum Chemistry* Prentice Hall **2000**, *5th ed.*

(84) Lewars, E. *Introduction to Computational Chemistry* KLUWER ACADEMIC PUBLISHERS **2003**.

(85) Tildesley, M. P. A. a. D. J. *Oxford University Press Inc. New York, 1st edition* **1987**.

(86) Smit, D. F. a. B. *Academic Press, Inc. Orlando, FL. USA, 2nd edition* **2001**.

(87) He, Q.; Shi, J. *Journal of Materials Chemistry* **2011**, *21*, 5845.

(88) Kim, J.; Lee, J. E.; Lee, J.; Yu, J. H.; Kim, B. C.; An, K.; Hwang, Y.; Shin, C.-H.; Park, J.-G.; Kim, J.; Hyeon, T. *Journal of the American Chemical Society* **2005**, *128*, 688.

(89) Breck, D. W. *Wiley-Interscience: New York* **1974**.

(90) Denayer, J. F.; Souverijns, W.; Jacobs, P. A.; Martens, J. A.; Baron, G. V. *The Journal of Physical Chemistry B* **1998**, *102*, 4588.

(91) Velu, S.; Ma, X.; Song, C. *Industrial & Engineering Chemistry Research* **2003**, *42*, 5293.

(92) Matsui, M.; Kiyozumi, Y.; Yamamoto, T.; Mizushina, Y.; Mizukami, F.; Sakaguchi, K. *Chemistry – A European Journal* **2001**, *7*, 1555.

(93) Yasuda, H.; Yoshimura, Y. *Catalysis Letters* **1997**, *46*, 43.

(94) Petushkov, A.; Ndiege, N.; Salem, A. K.; Larsen, S. C. Chapter 7 - Toxicity of Silica Nanomaterials: Zeolites, Mesoporous Silica, and Amorphous Silica Nanoparticles. In *Advances in Molecular Toxicology*; James, C. F., Ed.; Elsevier, 2010; Vol. Volume 4; pp 223.

(95) Petushkov, A.; Intra, J.; Graham, J. B.; Larsen, S. C.; Salem, A. K. *Chemical Research in Toxicology* **2009**, *22*, 1359.

(96) Fenoglio, I.; Croce, A.; Di Renzo, F.; Tiozzo, R.; Fubini, B. *Chemical Research in Toxicology* **2000**, *13*, 489.

(97) Cheng, C.-H.; Bae, T.-H.; McCool, B. A.; Chance, R. R.; Nair, S.; Jones, C. W. *The Journal of Physical Chemistry C* **2008**, *112*, 3543.

(98) Larsen, S. C. *The Journal of Physical Chemistry C* **2007**, *111*, 18464.

(99) Balkus, K. J.; Shi, J. *The Journal of Physical Chemistry* **1996**, *100*, 16429.

(100) Csajbók, É.; Bányai, I.; Vander Elst, L.; Muller, R. N.; Zhou, W.; Peters, J. A. *Chemistry – A European Journal* **2005**, *11*, 4799.

(101) Tsotsalas, M. M.; Kopka, K.; Luppi, G.; Wagner, S.; Law, M. P.; Schäfers, M.; De Cola, L. *ACS Nano* **2009**, *4*, 342.

(102) Ndiege, N.; Raidoo, R.; Schultz, M. K.; Larsen, S. *Langmuir* **2011**, *27*, 2904.

(103) Galownia, J.; Martin, J.; Davis, M. E. *Microporous and Mesoporous Materials* **2006**, *92*, 61.

(104) Vila; a, N.; lia; Amorim, R.; Martinho, O.; Reis, R.; Baltazar, F.; tima; Fonseca, A.; nio; Neves, I. *Journal of Materials Science* **2011**, *46*, 7511.

(105) Manuel, A.; Rodrigo, F.-P.; Silvia, I.; Jordi, A.; Ibarra, M. R.; Jesús, S. *Nanotechnology* **2006**, *17*, 4057.

(106) Martucci, A.; Pasti, L.; Marchetti, N.; Cavazzini, A.; Dondi, F.; Alberti, A. *Microporous and Mesoporous Materials* **2012**, *148*, 174.

(107) Braschi, I.; Gatti, G.; Paul, G.; Gessa, C. E.; Cossi, M.; Marchese, L. *Langmuir* **2010**, *26*, 9524.

(108) Braschi, I.; Blasioli, S.; Gigli, L.; Gessa, C. E.; Alberti, A.; Martucci, A. *Journal of Hazardous Materials* **2010**, *178*, 218.

(109) Ukmar, T.; Čendak, T.; Mazaj, M.; Kaučič, V.; Mali, G. *The Journal of Physical Chemistry C* **2012**, *116*, 2662.

(110) Ridker, P. M.; Cook, N. R.; Lee, I. M.; Gordon, D.; Gaziano, J. M.; Manson, J. E.; Hennekens, C. H.; Buring, J. E. *New England Journal of Medicine* **2005**, *352*, 1293.

(111) Catella-Lawson, F.; Reilly, M. P.; Kapoor, S. C.; Cucchiara, A. J.; DeMarco, S.; Tournier, B.; Vyas, S. N.; FitzGerald, G. A. *New England Journal of Medicine* **2001**, *345*, 1809.

(112) Corma, A. *Chemical Reviews* **1995**, *95*, 559.

(113) Jones, C. A.; Stec, D.; Larsen, S. C. *Journal of Molecular Catalysis A: Chemical* **2004**, *212*, 329.

(114) M. J. Frisch, G. W. T., H. B. Schlegel, G. E. Scuseria, M. A. Robb, J. R. Cheeseman, G. Scalmani, V. Barone, B. Mennucci, G. A. Petersson, H. Nakatsuji, M. Caricato, X. Li, H. P. Hratchian, A. F. Izmaylov, J. Bloino, G. Zheng, J. L. Sonnenberg, M. Hada, M. Ehara, K. Toyota, R. Fukuda, J. Hasegawa, M. Ishida, T. Nakajima, Y. Honda, O. Kitao, H. Nakai, T. Vreven, J. A. Montgomery, Jr., J. E. Peralta, F. Ogliaro, M. Bearpark, J. J. Heyd, E. Brothers, K. N. Kudin, V. N. Staroverov, R. Kobayashi, J. Normand, K. Raghavachari, A. Rendell, J. C. Burant, S. S. Iyengar, J. Tomasi, M. Cossi, N. Rega, J. M. Millam, M. Klene, J. E.

Knox, J. B. Cross, V. Bakken, C. Adamo, J. Jaramillo, R. Gomperts, R. E. Stratmann, O. Yazyev, A. J. Austin, R. Cammi, C. Pomelli, J. W. Ochterski, R. L. Martin, K. Morokuma, V. G. Zakrzewski, G. A. Voth, P. Salvador, J. J. Dannenberg, S. Dapprich, A. D. Daniels, Ö. Farkas, J. B. Foresman, J. V. Ortiz, J. Cioslowski, and D. J. Fox. *Gaussian, Inc., Wallingford CT* **2009**.

(115) Sherwood, P.; H. de Vries, A.; J. Collins, S.; P. Greatbanks, S.; A. Burton, N.; A. Vincent, M.; H. Hillier, I. *Faraday Discussions* **1997**, *106*, 79.

(116) Papayannis, D. K.; Kosmas, A. M. *Journal of Molecular Structure: THEOCHEM* **2010**, *957*, 47.

(117) Soscún, H.; Castellano, O.; Hernandez, J.; Arrieta, F.; Bermúdez, Y.; Hinchliffe, A.; Brussin, M. R.; Sanchez, M.; Sierraalta, A.; Ruette, F. *Journal of Molecular Catalysis A: Chemical* **2007**, *278*, 165.

(118) Binev, I. G.; Stamboliyska, B. A.; Binev, Y. I. *Journal of Molecular Structure* **1996**, *378*, 189.

(119) Allara, D. L.; Nuzzo, R. G. *Langmuir* **1985**, *1*, 52.

(120) van den Brand, J.; Blajiev, O.; Beentjes, P. C. J.; Terryn, H.; de Wit, J. H. W. *Langmuir* **2004**, *20*, 6308.

(121) Alcock, N. W.; Tracy, V. M.; Waddington, T. C. *Journal of the Chemical Society, Dalton Transactions* **1976**, 2243.

(122) Jiao, J.; Altwasser, S.; Wang, W.; Weitkamp, J.; Hunger, M. *J. Phys. Chem. B* **2004**, *108*, 14305.

(123) Li, S.; Huang, S.-J.; Shen, W.; Zhang, H.; Fang, H.; Zheng, A.; Liu, S.-B.; Deng, F. *J. Phys. Chem. C* **2008**, *112*, 14486.

(124) Jiao, J.; Altwasser, S.; Wang, W.; Weitkamp, J.; Hunger, M. *The Journal of Physical Chemistry B* **2004**, *108*, 14305.

(125) Li, S.; Huang, S.-J.; Shen, W.; Zhang, H.; Fang, H.; Zheng, A.; Liu, S.-B.; Deng, F. *The Journal of Physical Chemistry C* **2008**, *112*, 14486.

(126) Jiao, J.; Altwasser, S.; Wang, W.; Weitkamp, J.; Hunger, M. *Journal of Physical Chemistry B* **2004**, *108*, 14305.

(127) Papayannis, D.; Kosmas, A. *J. Mol. Struct. (Theochem)* **2010**, *957*, 47.

(128) Henson, N. J.; Cheetham, A. K.; Gale, J. D. *Chemistry of Materials* **1994**, *6*, 1647.

(129) Davis, M. E. *Nature* **2002**, *417*, 813.

(130) Raman, N. K.; Anderson, M. T.; Brinker, C. J. *Chemistry of Materials* **1996**, *8*, 1682.

(131) Aznar, E.; Sancenón, F.; Marcos, M. D.; Martínez-Máñez, R.; Stroeve, P.; Cano, J.; Amorós, P. *Langmuir* **2011**, *28*, 2986.

(132) Du, X.; He, J. *Langmuir* **2011**, *27*, 2972.
(133) Gai, S.; Yang, P.; Li, C.; Wang, W.; Dai, Y.; Niu, N.; Lin, J. *Advanced Functional Materials* **2010**, *20*, 1166.

(134) Gao, L.; Sun, J.; Li, Y. *Journal of Solid State Chemistry* **2011**, *184*, 1909.

(135) Gao, L.; Sun, J.; Li, Y.; Zhang, L. *Journal of Nanoscience and Nanotechnology* **2011**, *11*, 6690.

(136) Gao, L.; Sun, J.; Ren, B.; Li, Y.; Zhang, H. *Materials Research Bulletin* **2011**, *46*, 1540.

(137) Gao, Q.; Xu, Y.; Wu, D.; Sun, Y.; Li, X. *The Journal of Physical Chemistry C* **2009**, *113*, 12753.

(138) Hou, Z.; Li, C.; Ma, P.; Li, G.; Cheng, Z.; Peng, C.; Yang, D.; Yang, P.; Lin, J. *Advanced Functional Materials* **2011**, *21*, 2356.

(139) Huang, S.; Fan, Y.; Cheng, Z.; Kong, D.; Yang, P.; Quan, Z.; Zhang, C.; Lin, J. *The Journal of Physical Chemistry C* **2009**, *113*, 1775.

(140) Huh, S.; Wiench, J. W.; Trewyn, B. G.; Song, S.; Pruski, M.; Lin, V. S. Y. *Chemical Communications* **2003**, 2364.

(141) Izquierdo-Barba, I.; Sousa, E.; Doadrio, J.; Doadrio, A.; Pariente, J.; Martínez, A.; Babonneau, F.; Vallet-Regí, M. *Journal of Sol-Gel Science and Technology* **2009**, *50*, 421.

(142) Kang, X.; Cheng, Z.; Li, C.; Yang, D.; Shang, M.; Ma, P. a.; Li, G.; Liu, N.; Lin, J. *The Journal of Physical Chemistry C* **2011**, *115*, 15801.

(143) Manzano, M.; Aina, V.; Areán, C. O.; Balas, F.; Cauda, V.; Colilla, M.; Delgado, M. R.; Vallet-Regí, M. *Chemical Engineering Journal* **2008**, *137*, 30.

(144) Mellaerts, R.; Jammaer, J. A. G.; Van Speybroeck, M.; Chen, H.; Humbeeck, J. V.; Augustijns, P.; Van den Mooter, G.; Martens, J. A. *Langmuir* **2008**, *24*, 8651.

(145) Pasqua, L.; Testa, F.; Aiello, R.; Cundari, S.; Nagy, J. B. *Microporous and Mesoporous Materials* **2007**, *103*, 166.

(146) Slowing, I. I.; Trewyn, B. G.; Giri, S.; Lin, V. S. Y. *Advanced Functional Materials* **2007**, *17*, 1225.

(147) Song, S. W.; Hidajat, K.; Kawi, S. *Langmuir* **2005**, *21*, 9568.

(148) Vallet-Regí, M.; Balas, F.; Arcos, D. *Angewandte Chemie International Edition* **2007**, *46*, 7548.

(149) Vathyam, R.; Wondimu, E.; Das, S.; Zhang, C.; Hayes, S.; Tao, Z.; Asefa, T. *The Journal of Physical Chemistry C* **2011**, *115*, 13135.

(150) Wang, S. *Microporous and Mesoporous Materials* **2009**, *117*, 1.

(151) Yang, P.; Gai, S.; Lin, J. *Chemical Society Reviews* **2012**, *41*, 3679.

(152) Horcajada, P.; Rámila, A.; Pérez-Pariente, J.; Vallet, R.; amp; x; M. *Microporous and Mesoporous Materials* **2004**, *68*, 105.

(153) Tao, Z. M.; Xie, Y. W.; Goodisman, J.; Asefa, T. *Langmuir* **2010**, *26*, 8914.

(154) Zheng, H. Q.; Wang, Y.; Che, S. N. *J. Phys. Chem. C* **2011**, *115*, 16803.

(155) Wang, S. *Microporous Mesoporous Mater.* **2009**, *117*, 1.

(156) Wang, S. *Microporous and Mesoporous Materials* **2009**, *117*, 1.

(157) Nieto, A.; Colilla, M.; Balas, F.; Vallet-Regí, M. a. *Langmuir* **2010**, *26*, 5038.

(158) Nieto, A.; Balas, F.; Colilla, M.; Manzano, M.; Vallet-Regí, M. *Microporous and Mesoporous Materials* **2008**, *116*, 4.

(159) Huh, S.; Chen, H.-T.; Wiench, J. W.; Pruski, M.; Lin, V. S. Y. *Angewandte Chemie International Edition* **2005**, *44*, 1826.

(160) Zeng, W.; Qian, X.-F.; Zhang, Y.-B.; Yin, J.; Zhu, Z.-K. *Materials Research Bulletin* **2005**, *40*, 766.

(161) Lee, S. H.; Rossky, P. J. *The Journal of Chemical Physics* **1994**, *100*, 3334.

(162) Hess, B.; Kutzner, C.; van der Spoel, D.; Lindahl, E. *Journal of Chemical Theory and Computation* **2008**, *4*, 435.

(163) Van Der Spoel, D.; Lindahl, E.; Hess, B.; Groenhof, G.; Mark, A. E.; Berendsen, H. J. C. *Journal of Computational Chemistry* **2005**, *26*, 1701.

(164) Parrinello, M.; Rahman, A. *Journal of Applied Physics* **1981**, *52*, 7182.

(165) Darden, T.; York, D.; Pedersen, L. *The Journal of Chemical Physics* **1993**, *98*, 10089.

(166) Essmann, U.; Perera, L.; Berkowitz, M. L.; Darden, T.; Lee, H.; Pedersen, L. G. *The Journal of Chemical Physics* **1995**, *103*, 8577.

(167) Coasne, B.; Fourkas, J. T. *The Journal of Physical Chemistry C* **2011**, *115*, 15471.

(168) Coasne, B.; Viau, L.; Vioux, A. *The Journal of Physical Chemistry Letters* **2011**, *2*, 1150.

(169) Coasne, B.; Fourkas, J. T. *J. Phys. Chem. C* **2011**, *115*, 15471.

(170) Coasne, B.; Viau, L.; Vioux, A. *J. Phys. Chem. Lett.* **2011**, *2*, 1150.

(171) Vachon, M. G.; Nairn, J. G. *European Journal of Pharmaceutics and Biopharmaceutics* **1998**, *45*, 9.

(172) Babonneau, F.; Yeung, L.; Steunou, N.; Gervais, C.; Ramila, A.; Vallet-Regi, M. *Journal of Sol-Gel Science and Technology* **2004**, *31*, 219.

(173) Azais, T.; Tourne-Peteilh, C.; Aussenac, F.; Baccile, N.; Coelho, C.; Devoisselle, J. M.; Babonneau, F. *Chem. Mat.* **2006**, *18*, 6382.

(174) Azais, T.; Hartmeyer, G.; Quignard, S.; Laurent, G.; Tourne-Peteilh, C.; Devoisselle, J. M.; Babonneau, F. *Pure and Applied Chemistry* **2009**, *81*, 1345.

(175) Izquierdo-Barba, I.; Sousa, E.; Doadrio, J. C.; Doadrio, A. L.; Pariente, J. P.; Martinez, A.; Babonneau, F.; Vallet-Regi, M. *Journal of Sol-Gel Science and Technology* **2009**, *50*, 421.

(176) Azaïs, T.; Tourné-Péteilh, C.; Aussenac, F.; Baccile, N.; Coelho, C.; Devoisselle, J.-M.; Babonneau, F. *Chemistry of Materials* **2006**, *18*, 6382.

(177) Babonneau, F.; Yeung, L.; Steunou, N.; Gervais, C.; Ramila, A.; Vallet-Regi, M. *Journal of Sol-Gel Science and Technology* **2004**, *31*, 219.

(178) Gao, L.; Sun, J. H.; Li, Y. Z. *Journal of Solid State Chemistry* **2011**, *184*, 1909.

(179) Gao, L.; Sun, J. H.; Ren, B.; Li, Y. Z.; Zhang, H. *Materials Research Bulletin* **2011**, *46*, 1540.

(180) Zhu, Y.; Shi, J.; Li, Y.; Chen, H.; Shen, W.; Dong, X. *Microporous Mesoporous Mater.* **2005**, *85*, 75.

(181) Costa, P.; Sousa Lobo, J. M. *European Journal of Pharmaceutical Sciences* **2001**, *13*, 123.

(182) Costa, P.; Lobo, J. M. S. *European Journal of Pharmaceutical Sciences* **2001**, *13*, 123.

(183) Nieto, A.; Colilla, M.; Balas, F.; Vallet-Regi, M. *Langmuir* **2010**, *26*, 5038.

(184) Langer, R.; Tirrell, D. A. *Nature* **2004**, *428*, 487.

(185) Langer, R. *Nature* **1998**, *392*, 5.

(186) Slowing, I. I.; Vivero-Escoto, J. L.; Wu, C.-W.; Lin, V. S. Y. *Advanced Drug Delivery Reviews* **2008**, *60*, 1278.

(187) Rimoli, M. G.; Rabaioli, M. R.; Melisi, D.; Curcio, A.; Mondello, S.; Mirabelli, R.; Abignente, E. *Journal of Biomedical Materials Research Part A* **2008**, *87A*, 156.

(188) Rana, V. K.; Park, S. S.; Parambadath, S.; Kim, M. J.; Kim, S.-H.; Mishra, S.; Singh, R. P.; Ha, C.-S. *MedChemComm* **2011**, *2*, 1162.

(189) Grund, S.; Doussineau, T.; Fischer, D.; Mohr, G. J. *Journal of Colloid and Interface Science* **2012**, *365*, 33.

(190) Vilaça, N.; Amorim, R.; Martinho, O.; Reis, R.; Baltazar, F.; Fonseca, A.; Neves, I. *Journal of Materials Science* **2011**, *46*, 7511.

(191) Tsotsalas, M.; Busby, M.; Gianolio, E.; Aime, S.; De Cola, L. *Chemistry of Materials* **2008**, *20*, 5888.

(192) Longley, D. B.; Harkin, D. P.; Johnston, P. G. *Nat Rev Cancer* **2003**, *3*, 330.

(193) Meyerhardt, J. A.; Mayer, R. J. *New England Journal of Medicine* **2005**, *352*, 476.

(194) Akalin, E.; Akyuz, S.; Akyuz, T. *Journal of Molecular Structure* **2007**, *834–836*, 477.

(195) Lin, F. H.; Lee, Y. H.; Jian, C. H.; Wong, J.-M.; Shieh, M.-J.; Wang, C.-Y. *Biomaterials* **2002**, *23*, 1981.

(196) Sun, C.-Y.; Qin, C.; Wang, X.-L.; Yang, G.-S.; Shao, K.-Z.; Lan, Y.-Q.; Su, Z.-M.; Huang, P.; Wang, C.-G.; Wang, E.-B. *Dalton Transactions* **2012**, *41*, 6906.

(197) Lopes, S.; Simeonova, M.; Gameiro, P.; Rangel, M.; Ivanova, G. *The Journal of Physical Chemistry B* **2011**, *116*, 667.

(198) Zhu, Y.; Shi, J.; Li, Y.; Chen, H.; Shen, W.; Dong, X. *Micropor. Mesopor. Mat.* **2005**, *85*, 75.

(199) Dobrowolski, J. C.; Rode, J. E.; Kołos, R.; Jamróz, M. H.; Bajdor, K.; Mazurek, A. P. *J. Phys. Chem. A* **2005**, *109*, 2167.

(200) Akalin, E.; Akyuz, S.; Akyuz, T. *J. Mol. Struct.* **2007**, *834*, 477.

(201) Grassi, M.; Lamberti, G.; Cascone, S.; Grassi, G. *International Journal of Pharmaceutics* **2011**, *418*, 130.

(202) Manzano, M.; Lamberti, G.; Galdi, I.; Vallet-Regí, M. *AAPS PharmSciTech* **2011**, *12*, 1193.

(203) Maria, G.; Stoica, A.-I.; Luta, I.; Stirbet, D.; Radu, G. L. *Microporous and Mesoporous Materials* **2012**, *162*, 80.

(204) Narang, K. K.; Singh, V. P.; Bhattacharya, D. *Polyhedron* **1997**, *16*, 2491.

(205) Slowing, II; Trewyn, B. G.; Giri, S.; Lin, V. S. Y. *Adv. Func. Mat.* **2007**, *17*, 1225.

(206) Slowing, II; Vivero-Escoto, J. L.; Wu, C. W.; Lin, V. S. Y. *Advanced Drug Delivery Reviews* **2008**, *60*, 1278.

(207) Trewyn, B. G.; Giri, S.; Slowing, II; Lin, V. S. Y. *Chem. Commun.* **2007**, 3236.

(208) Kralj, M. *Periodicum biologorum* **2003**, *105*, 99.

(209) Horcajada, P.; Serre, C.; Vallet-Regi, M.; Sebban, M.; Taulelle, F.; Ferey, G. *Angewandte Chemie-International Edition* **2006**, *45*, 5974.

(210) Galarneau, A.; Cambon, H.; Di Renzo, F.; Fajula, F. *Langmuir* **2001**, *17*, 8328.

(211) Wang, X.; Lin, K. S. K.; Chan, J. C. C.; Cheng, S. *The Journal of Physical Chemistry B* **2005**, *109*, 1763.

(212) Doadrio, A. L.; Sousa, E. M. B.; Doadrio, J. C.; Pérez Pariente, J.; Izquierdo-Barba, I.; Vallet-Regí, M. *Journal of Controlled Release* **2004**, *97*, 125.

(213) Katiyar, A.; Ji, L.; Smirniotis, P.; Pinto, N. G. *Journal of Chromatography A* **2005**, *1069*, 119.

(214) Katiyar, A.; Yadav, S.; Smirniotis, P. G.; Pinto, N. G. *Journal of Chromatography A* **2006**, *1122*, 13.

(215) Botella, P.; Corma, A.; Quesada, M. *Journal of Materials Chemistry* **2012**, *22*, 6394.

(216) Kim, S.-S.; Pauly, T. R.; Pinnavaia, T. J. *Chemical Communications* **2000**, 835.

(217) Wang, J.; Tsung, C.-K.; Hayward, R. C.; Wu, Y.; Stucky, G. D. *Angewandte Chemie International Edition* **2005**, *44*, 332.

(218) Yang, H.; Vovk, G.; Coombs, N.; Sokolov, I.; A. Ozin, G. *Journal of Materials Chemistry* **1998**, *8*, 743.

(219) Lind, A.; Spliethoff, B.; Lindén, M. *Chemistry of Materials* **2003**, *15*, 813.

(220) Gao, X.; Nie, S. *The Journal of Physical Chemistry B* **2003**, *107*, 11575.

(221) Yokoi, T.; Karouji, T.; Ohta, S.; Kondo, J. N.; Tatsumi, T. *Chemistry of Materials* **2010**, *22*, 3900.

(222) Lacasta, S.; Sebastián, V. c.; Casado, C.; Mayoral, A. l.; Romero, P.; Larrea, A. n.; Vispe, E.; López-Ram-de-Viu, P.; Uriel, S.; Coronas, J. n. *Chemistry of Materials* **2011**, *23*, 1280.

(223) Lavasanifar, A.; Samuel, J.; Kwon, G. S. *Advanced Drug Delivery Reviews* **2002**, *54*, 169.

(224) Kataoka, K.; Harada, A.; Nagasaki, Y. *Advanced Drug Delivery Reviews*.

(225) Alonso, M. J.; Sánchez, A. *Journal of Pharmacy and Pharmacology* **2003**, *55*, 1451.

(226) Lian, T.; Ho, R. J. Y. *Journal of Pharmaceutical Sciences* **2001**, *90*, 667.